High Harmonic Spectroscopy of Complex Molecules

by

Michael C. H. Wong

Thesis submitted to the
Faculty of Graduate and Postdoctoral Studies
in partial fulfillment of the requirements
for the Doctorate in Philosophy degree in
Physics

Department of Physics
Faculty of Science
University of Ottawa

0.1 List of publications included in this thesis

The following publications are included as chapters in this thesis.

1. J.-P. Brichta, **M. C. H. Wong**, J. B. Bertrand, H.-C. Bandulet, D. M. Rayner, and V. R. Bhardwaj
   Comparison and real-time monitoring of high-order harmonic generation in different sources
   Physical Review A **79**, 033404 (2009)

2. **M. C. H. Wong**, J.-P. Brichta, and V. R. Bhardwaj
   High-harmonic generation in H_2O
   Optics Letters **35**, 1947 (2010)

3. **M. C. H. Wong**, J.-P. Brichta, and V. R. Bhardwaj
   Signatures of symmetry and electronic structure in high-order harmonic generation in polyatomic molecules
   Physical Review A **81**, 061402(R) (2010)

4. **M. C. H. Wong**, J.-P. Brichta, M. Spanner, S. Patchkovskii, and V. R. Bhardwaj
   High-harmonic spectroscopy of molecular isomers
   Physical Review A **84**, 051403(R) (2011)
   Physical Review A **85**, 049901(E) (2012)

5. **M. C. H. Wong**, A.-T. Le, A. F. Alharbi, A. E. Boguslavskiy, R. R. Lucchese, J.-P. Brichta, C. D. Lin, and V. R. Bhardwaj
   High Harmonic Spectroscopy of the Cooper Minimum in Molecules
   Physical Review Letters **110**, 033006 (2013)

6. **M. C. H. Wong**, M. Spanner, J.-P. Brichta, S. Patchkovskii, and V. R. Bhardwaj
   High-harmonic spectroscopy of structural isomers
   In preparation (2014)

Additional publications by the author

The following publications are not directly related to work presented in this thesis.

7. R. A. Ganeev, L. B. Elouga Bom, J. Abdul-Hadi, **M. C. H. Wong**, J. P. Brichta, V. R. Bhardwaj, and T. Ozaki
   Higher-Order Harmonic Generation from Fullerene by Means of the Plasma Harmonic Method
   Physical Review Letters **102**, 013903 (2009)

8. R. A. Ganeev, L. B. Elouga Bom, **M. C. H. Wong**, J.-P. Brichta, V. R. Bhardwaj, P. V. Redkin, and T. Ozaki
   High-order harmonic generation from C_{60}*-rich plasma*
   Physical Review A **80**, 043808 (2009)

9. A. F. Alharbi, A. E. Boguslavskiy, N. Thiré, **M.C.H. Wong**, B. Schmidt, F. Légaré and V.R. Bhardwaj
   High Harmonic Generation in Cyclohexadiene
   In preparation (2014)

10. R. Cireasa, A. E. Boguslavsky, B. Pons, **M. C. H. Wong**, D. Descamps, S. Petit, H. Ruf, N. Thiré, A. Ferré, J. Suarez, J. Higuet, B. E. Schmidt, A. F. Alharbi, F. Légaré, V. Blanchet, B. Fabre, S. Patchkovskii, O. Smirnova, Y. Mairesse and V. R. Bhardwaj
    Probing molecular chirality on sub-femtosecond time-scale.
    Submitted to Nature (September, 2014)

0.2 Abstract

Advancements in spectroscopy rely on the improvement of two fundamental characteristics: spatial and temporal resolutions. High harmonic spectroscopy (HHS) is an emerging technology that promises the capability of studying the fastest processes that exist today: electronic motion with ångström spatial and attosecond temporal resolution. HHS is based on the process of high harmonic generation (HHG) which arises from the nonlinear interaction between an intense, infrared laser pulse and an atomic or molecular gaseous medium, producing coherent, attosecond-duration bursts of extreme ultraviolet (XUV) light.

In order to utilize the attosecond pulses for spectroscopic measurements, it is necessary to improve the conversion efficiency of HHG. Chapter 2 of this thesis describes the improvements we make to the HHG source in order to obtain high XUV photon flux and we report on the nonlinear ionization of atomic systems using these pulses in Chapter 6.

In Chapters 3 – 5, we describe several HHG experiments in complex, polyatomic molecules in order to promote the use of HHS as a general spectroscopic tool. Amplitude modulations in high harmonic spectra of complex molecules can be attributed to several types of interference conditions that depend on a system's molecular or electronic structure such as recombination with multiple centres or dynamical interference from multi-orbital contributions to ionization. Our results demonstrate the capability of HHS to extract useful information on molecular and electronic structure from large, polyatomic molecules directly from their high harmonic spectra. Furthermore, we use HHS to investigate the suppression of ionization in complex molecules due to quantum destructive interference during ionization as well as the distinguishability of emitted harmonic spectra from molecular isomers.

Chapter 6 explores the study of multi-electron dynamics in complex molecules using XUV multiphoton ionization of atoms and molecules as well as the ionization and fragmentation of C_{60} which has hundreds of delocalized valence electrons. This thesis also describes the author's role in the design and fabrication of a time-of-flight mass spectrometer (Section 6.1) as well as an HHG detector system (Appendix A).

0.3 Sommaire

Les progrès de la spectroscopie reposent sur l'amélioration de deux caractéristiques fondamentales: la résolution spatiale et temporelle. La spectroscopie des harmoniques élevées (SHE) est une technologie émergente qui promet une capacité d'étudier les processus le plus rapides existant aujourd'hui, notamment le mouvement électronique sur des échelles spatiales et temporelles de l'Angstrom et de l'attoseconde. La SHE est basée sur le processus de génération d'harmoniques élevées (GHE) qui résulte de l'interaction non-linéaire entre une impulsion laser infrarouge intense et un milieu atomique ou moléculaire gazeux, produisant des flash ultraviolets (XUV) d'une durée attoseconde, cohérents et d'une intensité extrême.

Afin d'utiliser les impulsions attosecondes pour des mesures spectroscopiques, il est nécessaire d'améliorer l'efficacité de conversion de la GHE. Nous présentons dans cette thèse, au chapitre 2, les améliorations apportés á la source de GHE afin d'obtenir une forte fluence de photons XUV et nous rapportons l'ionisation non linéaire des systèmes atomiques à l'aide de ces impulsions dans le chapitre 6.

Au sein des chapitres 3 – 5, nous d'écrivons plusieurs expériences de la GHE dans des molécules polyatomiques complexes afin de promouvoir l'utilisation de la SHE comme un outil spectroscopique générale. Les modulations d'amplitude dans le spectre d'harmoniques élevées des molécules complexes peuvent être attribuées à plusieurs types de conditions d'interférence qui dépendent de la structure moléculaire ou électronique d'un système tel que les recombinaisons multi-centres ou les contributions à l'ionisation par l'interférence dynamique des multi-orbitales. En outre, nous utilisons la SHE pour sonder la suppression de l'ionisation des molécules complexes en raison de l'interférence quantique destructive pendant l'ionisation ainsi que les différences spectrales des harmoniques émis depuis les isomères moléculaires.

Le chapitre 6 porte sur l'étude des dynamiques multi-électroniques dans des molécules complexes en utilisant l'ionisation multiple par XUV des atomes et des molécules ainsi que l'ionisation et la fragmentation de C_{60} comportant des centaines d'électrons de valence délocalisés. Cette thèse décrit également le rôle de l'auteur dans la conception et la fabrication d'un spectromètre de masse à temps-de-vol (section 6.1) et un système de détection de GHE (annexe A).

0.4 Acknowledgements

So many people to thank and so little space to do it. Let's get started.

First and foremost I'd like to thank my thesis supervisor, Ravi Bhardwaj, for giving me the amazing opportunity to work in such a cutting-edge field of research. Ravi, you've crafted a tremendous research program so far at the University of Ottawa and I am lucky to have been a part of your Ultrafast Photonics Group. It would be impossible to put into words all that I've learned from you about laser science, spectroscopy, and experimental techniques during my time as your student. I appreciate that you trusted me with both your extensive research dollars as well as to provide entertainment for your kids with all the DVDs I gave them!

The results of this research project could not have been possible without the aid of numerous colleagues and collaborators at the University of Ottawa, the National Research Council, and the Advanced Laser Light Source in Varennes, QC. The list of people who have made this research happen is long and convoluted but I will do my best to highlight each contribution.

I'd like to thank the cast and crew from the NRC Femto-(Atto)-second Science Group for providing my first taste of strong-field laser science. Thank you David Villeneuve and Paul Corkum for letting me into your labs as a wide-eyed undergraduate student to build vacuum chambers and power supplies. I wouldn't be where I am today if not for your guidance and inspiration to apply myself to this field. Thanks to Domagoj Pavicic and John Parsons for teaching me about vacuum technology and the design of spectrometers. I've kept your lessons in mind with every flange I've tightened and electrode I've designed. Thanks to Patrick Dooley for sharing your knowledge about laser safety. Some parts of your famous presentation still live on at University of Ottawa today! I also am grateful for technical advice from Bert Avery and David Joines who showed me that sometimes I have to get my hands dirty when working in a laser lab.

My experimental results stem from many weeks of beamtimes at the Advanced Laser Light Souces labs in Varennes, QC as well as the Ultrafast Photonics labs at the University of Ottawa. Thanks to JP Brichta for spending numerous days and nights with me

in the ALLS labs collecting data and setting up experiments. Your expertise in laser lab techniques was indispensable and your cheerful personality made those many beamtimes bearable. I'm very pleased that we got to publish so many papers together to represent the efforts we put in. Thanks also to Abdullah Alharbi for your help with several experiments. I believe your hard work and dedication will pay off with a successful scientific career. Thanks very much to Andrey Boguslavskiy for joining in on experiments and analysis. You brought a new level of proficiency and detail to our experiments and really broadened our capabilities of what we could achieve in the lab. Thank you also to Jean-Michel Guay for all your assistance in lifting heavy equipment and Farhana Baset for feeding me delicious Bengali food.

The team of researchers and technicians at ALLS also played a big part in helping this research project along. Thank you to François Légaré for your infectious enthusiasm about lasers, for your help in solving any experimental problem, and for always taking a personal interest in whatever experiment I was currently working on. Thank you to Bruno Schmidt for providing us with such a novel and elite laser source with which to conduct our experiments. Thank you to Mathieu Giguère and Philippe Lassonde for your help with the short-pulse C_{60} experiments. Thank you to François Poitras, Antoine Laramée, Lukasz Andrzejewski (I appreciate your translation help!), and Guy Lebrun for your expert technical advice and assistance. Thank you to Heidi Bandulet and Daniel Comtois for teaching me about the HHG and VMI systems during my first few visits to ALLS. And finally, thank you to Tsuneyuki Ozaki for your collaboration on the HHG in C_{60} project. I am extremely grateful to have had the chance to work in one of the world's leading laser labs.

Since we are an experimental group, our research has benefited from collaboration with some world-class experts in strong-field theory and computation. Thank you to Thomas Brabec for being our resident theoretical expert at every level of this research project. I appreciate your involvement throughout the various stages of my scientific career as professor of my quantum optics course, examiner for my comprehensive exam and doctoral thesis, and finally as chair of the department where I work. Thank you to Michael Spanner for your contribution to the isomers project and to Anh Thu Le for your contribution to the Cooper minimum project.

Finally, it is with great pleasure that I thank my family and friends for their incredible support during the course of my graduate studies. To my parents, Li Shiau and Kat Ching, my siblings, John and Janet, and all my aunts, uncles, and cousins, thank you forever for your love and support from the time I was little to becoming an official doctor and beyond. To all my friends both old and new, young and old, rich and poor, thank you kindly for all the support and kind words you've given me (GHS, uOttawa, v-ball, HMC!). And last but not least, I dedicate this work to my new family. Chieu Anh, you've been a wonderfully supportive and loving influence in my life and you've given me a reason to want to work hard to provide an incredible life for both of us as well as for Zak and Snoopy who provide us with hours upon hours of devotion and entertainment.

Contents

List of Figures

Chapter 1

Introduction

1.1 The advent of high harmonic spectroscopy

The science of spectroscopy is an age-old technique to study the properties of matter. One can arguably attribute the first discovery in spectroscopy to be when Sir Isaac Newton showed that white light could be dispersed into a spectrum using a prism in the late 1600's [1]. Since then, spectroscopy has evolved into an important scientific tool that has led to numerous achievements in modern physics, including the invention of the laser in the late 1950's [2, 3]. As pulsed lasers became more commonplace, modern laser spectroscopists began to develop a field of study capable of probing the static and dynamic nature of the smallest known particles that exist in our world: atoms, molecules, and electrons. For example, Raman spectroscopy [4] is capable of distinguishing between molecules based on their vibrational frequencies which are specific to their chemical bonds and molecular symmetry. Laser-induced fluorescence [5] can be used to study three-dimensional molecular structure and dynamics with high signal-to-noise ratio. It is even possible to analyse molecular structure regardless of its physical state (solid, gas, or liquid) using laser-induced breakdown spectroscopy [6, 7] which detects emission based on a tiny high-temperature plasma plume created by a laser source.

The wavelength and duration of the laser pulse describe the two fundamental characteristics of spectroscopy, spatial and temporal resolutions, with the latter providing the dynamics information. Improvements to spectroscopy dictate a constant need to pursue shorter and shorter laser pulse durations in order to increase the time resolution of spectroscopic techniques. The mid 1980's brought the creation of femtosecond (10^{-15} s) light pulses and introduced the field of femtochemistry in which new, unprecedented techniques proved capable of studying atoms and molecules on their own timescale and procured a Nobel Prize for A. Zewail in 1999 [8, 9] for his pioneering research. However, the femtosecond timescale is not capable of probing electron dynamics which operate on the shorter, attosecond (10^{-18} s) timescale. In order to decrease the pulse duration to the sub-femtosecond domain, it is necessary to work with frequencies in the extreme ultraviolet (XUV) spectrum as visible light is not capable of supporting attosecond pulses due to the Fourier transform limit. Additionally, attosecond light pulses require a broad bandwidth of frequencies spanning several electron volts (eV). The technique capable of producing the necessary bandwidth for attosecond laser pulses and is currently responsible for the creation of the shortest optical pulses to date ($\sim$80 as, [10]), is high harmonic generation (HHG). The novel form of laser-induced emission spectroscopy to be pursued in this thesis is known as high harmonic spectroscopy (HHS) and analyzes the emission spectrum of HHG from an atomic or molecular target. Only HHS can provide the precise time resolution needed to study electron dynamics, stemming from the sub-cycle nature of the HHG process.

HHG is the result of a nonlinear interaction between a near-infrared short pulsed laser beam which is focused on an atomic or molecular gaseous target, producing many orders of harmonics of the fundamental optical field with energies capable of reaching several hundred eV. This process was first observed in 1987 [11] where the 17^{th} harmonic of a 248 nm beam was emitted through interaction with neon gas. The HHG process is based on electron self-recollision which was first described by Corkum in 1993 [12] where an electron in a strong laser field tunnels away from its parent ion, accelerates in the continuum due to the influence of the laser-electric field, then recombines to its ground state while emitting a high energy XUV photon. The last 25 years have shown significant advancement in HHG technology and has been primarily focused on optimization of the laser source. Tabletop titanium-sapphire femtosecond lasers based on the chirped pulse amplification (CPA) process [13] are now available in numerous laser labs around the world, producing high energy 800 nm light pulses with durations on the order of 20–30 fs. Pulse compression schemes to reduce the pulse durations of these lasers to less than two optical cycles [14, 15] are in widespread use as well. Some labs employ ultra stable systems with intensities up to 10^{18} W/cm^2 with less than 1% energy fluctuations [16] as well as electric field phase stability within the pulse envelope of less than 100 as [17]. HHG has not been restricted to 800 nm as the use of longer wavelengths as driving fields for HHG has been made possible by optical parametric amplification (OPA) technology [18]. These improvements in laser technology have enabled the generation of single attosecond pulses as short as ∼80 as in duration [10] as well as high harmonic emission in the keV X-ray regime [19].

The advantage of using attosecond pulses to study fundamental electronic processes is evident when high photon energies are needed for the excitation of, for example, surface and volume plasmons in large molecules such as C_{60} [20], or the excitation of low-lying core electrons [21]. To pursue these studies, an efficient source of high harmonics are required and we devote a section (1.3) and chapter (see Chapter 2) to this topic. However, in order to examine key electronic processes such as valence electron dynamics or electron correlations in atoms and molecules, we must return to the original interaction between the laser and the nonlinear system and that is where this research project begins.

1.1.1 Goal and outline of the thesis

The research presented in this thesis is the author's contribution to the fields of HHS and attosecond science during the course of the Ph.D project. While most HHG experiments have focused on atoms (particularly noble gases) in the past, molecules are particularly interesting targets due to the complexity of their electronic structures and the role this plays on molecular and electronic dynamics. There still exists a deficiency in theoretical tools and models to fully study the various interactions during the HHG process in molecules although some significant results have already been seen [22, 23, 24]. In the meantime, experimental work is fluorishing in simple di- and triatomic molecules [25, 26, 27, 28, 29, 30, 31, 32, 33, 34]. This extension of HHG from atoms to molecules, while complicated, has a strong influence on a variety of topics in chemistry and physics and is a necessary requirement to study the fastest processes that exist.

This thesis describes several advances made in studying molecular and electronic structure in complex molecules using HHS. The second half of Chapter 1 contains important background information and theory for HHG from atoms and molecules. Our improvement to optimizing high harmonic yield, with the use of finite and semi-infinite gas cells, is described in Chapter 2. A thorough description of the laser source we used in our experiments, as well as the experimental HHG system, is provided in Publication 1 in that chapter.

The next three chapters report on the use of HHS to study various aspects of molecular properties such as signatures of symmetry in electronic structure (Chapter 3), the influence of molecular structure (Chapter 4), and isomeric effects (Chapter 5). Each publication within the chapters provides novel development in the use of HHS to decipher these properties and leads towards the goal of time-resolved molecular spectroscopy of complex molecules with attosecond (10^{-18} s) temporal and ångström (10^{-10} m) spatial resolution.

Chapter 6 explores the study of multi-electron dynamics in complex molecules using XUV multiphoton ionization of atoms and molecules as well as the ionization and fragmentation of C_{60} which has hundreds of delocalized valence electrons.

A global conclusion for the thesis is included in Chapter 7 as well as an update on current progress and future plans for additional research in this field.

1.2 Theory of high harmonic generation

The basis of HHG can be described by a semiclassical three step model [12] which both qualitatively and quantitavely describes the principle properties of emitted photons during this highly nonlinear process. The three steps (represented in Fig. 1.1) are tunnel ionization, acceleration of the electron in the laser-electric field, and finally, radiative recombination.

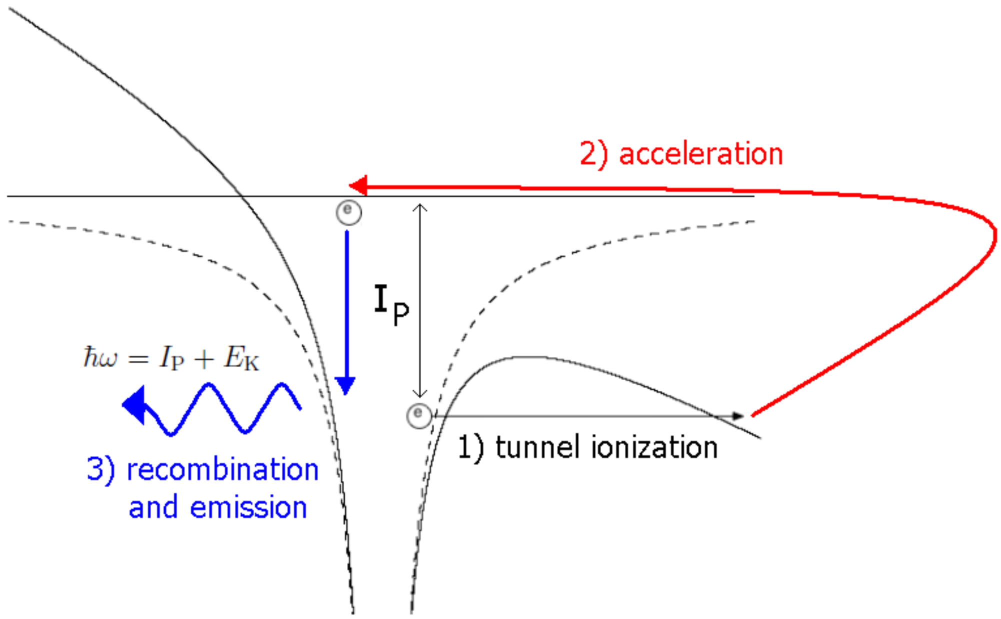

Figure 1.1: An electron sits in the Coulomb potential of the atom (dashed line). The height of the potential barrier is the ionization potential, I_P. The strong laser field distorts the potential to one side (solid line) during one half-cycle of the laser field allowing the electron to tunnel-ionize. The electron experiences acceleration due to the strong laser field then recombines back to its ground state when in the vicinity of its parent ion and emits a photon with energy, $\hbar\omega = I_p + E_k$, where E$_k$ is the kinetic energy the electron gained in the laser-electric field.

1.2.1 Tunnel ionization

First, a linearly polarized strong laser field is incident on a nonlinear system such as an atom. We consider the electron under the Coulomb potential of the nucleus with potential energy, V_0 = -1/r. The barrier height is known as the ionization potential, I_P, and is the energy that the electron requires to free itself from the nucleus. However, the laser field can act to lower the potential barrier to one side such that the electron wavepacket is permitted to tunnel to freedom (see step 1 of Fig. 1.1). This process can happen every half-laser cycle thus tunneling occurs twice per optical cycle. The tunneling probability is influenced by the height and thickness of the potential barrier and it is possible to calculate the necessary electric field strength to completely suppress the barrier such that the tunneling rate becomes 1, known as barrier suppression ionization [35]. This value corresponds to the saturation intensity, I_sat, given by

$$I_\mathrm{sat}(\mathrm{W/cm^2}) = 4 \times 10^9 I_\mathrm{P}(\mathrm{eV})^4 \tag{1.1}$$

where the units are stated in brackets. Equation 1.1 shows that it only requires intensities close to 10^{14} W/cm^2 to ionize most atoms and molecules ($I_\mathrm{P} \approx$ 8–15 eV) which is easily attainable with modern laser systems.

The distortion of the potential barrier varies with time and tunnel ionization is only possible if the barrier is lowered for sufficiently long. Keldysh introduced an adiabaticity parameter, γ, which related the tunneling time with the period, $T_0 = 2\pi/\omega_0$, of the laser electric field [36] and is given by

$$\gamma = \sqrt{\frac{I_\mathrm{P}}{2U_\mathrm{P}}} \tag{1.2}$$

where $U_\mathrm{P} = E^2 \,/\, 4\omega^2$ is the ponderomotive potential of the electron (the average kinetic energy the electron gains in an oscillating electric field).

1.2.2 Acceleration and recombination

Once the electron has left the potential of the atom and has entered the continuum, the laser-electric field is strong enough to dominate the electron's motion (see Step 2 of Fig. 1.1). The potential the electron now finds itself in is linear, with its slope determined by the instantaneous value of the laser field. Just after ionization, the electron is now accelerated away from the ion and when the laser field changes direction, the slope of the potential reverses and the electron is now driven back towards its initial position. As the electron finds itself in the vicinity of its parent ion, it can radiatively recombine (see Step 3 of Fig. 1.1) to emit a photon with energy equal to the ionization potential of the system plus the kinetic energy, E_{K}, the electron acquired during its travel:

$$\hbar\omega = I_{\mathrm{P}} + E_{\mathrm{K}}. \tag{1.3}$$

This process occurs every half cycle of the laser pulse so that we have XUV photons being emitted with period $T_0/2$. This periodicity gives rise to interference fringes in the spectral domain, producing an emission spectrum of frequencies separated by $2\omega_0$. The inversion symmetry caused by electrons tunneling towards opposite sides of the system each half cycle gives rise to a sign change in the emission and thus the emitted harmonics can only be odd multiples of the fundamental frequency.

In order to examine the recombination energy of the electron, we can map each velocity the electron acquires in the laser field to a classical trajectory. The equation of motion for the electron is

$$a(t) = -E_0 \cos(\omega_0 t). \tag{1.4}$$

To simplify the problem, we impart the following initial conditions: for an electron born at time t_{i}, we (1) ignore the distance through which the electron travels through the potential barrier so that it is born at the origin ($x(t_{\mathrm{i}}) = 0$), and (2) assume the electron loses any kinetic energy it had due to the tunneling process so that it is born with zero initial velocity ($v(t_{\mathrm{i}}) = 0$). Solving Eq. 1.4 gives us velocity and position:

$$v(t) = -E_0/\omega_0(\sin(\omega_0 t) - \sin(\omega_0 t_{\mathrm{i}})) \tag{1.5}$$

$$x(t) = E_0/\omega_0^2(\cos(\omega_0 t) - \cos(\omega_0 t_{\mathrm{i}})) + E_0/\omega_0 \sin(\omega_0 t_{\mathrm{i}})(t - t_{\mathrm{i}}). \tag{1.6}$$

At some recollision time, $t_{\mathrm{f}} > 0$, the electron returns to the ion thus we have $x(t_{\mathrm{f}}) = 0$ and we can solve Eq. 1.6 to find

$$\cos(\omega_0 t_{\mathrm{i}}) - \cos(\omega_0 t_{\mathrm{f}}) = \omega_0 \sin(\omega_0 t_{\mathrm{i}})(t_{\mathrm{f}} - t_{\mathrm{i}}). \tag{1.7}$$

The largest velocity (and thus largest kinetic energy) the electron can gain may be found by plotting these classical trajectories from Eq. 1.7 or by numerically solving the system of equations generated from Eq. 1.7 and the derivative of Eq. 1.5 set to zero. Electron trajectories are typically spoken of in terms of their phase of birth. For the sinusoidal laser pulse, each t_i is related to a specific phase, ϕ, dependent on the period of oscillation. For $\lambda = 800$ nm, the period is 2.7 fs. It was first seen in [12] that the highest electron velocity and hence, the highest photon energy, corresponds to the phase of birth of $\phi = 17°$, known as the cutoff.

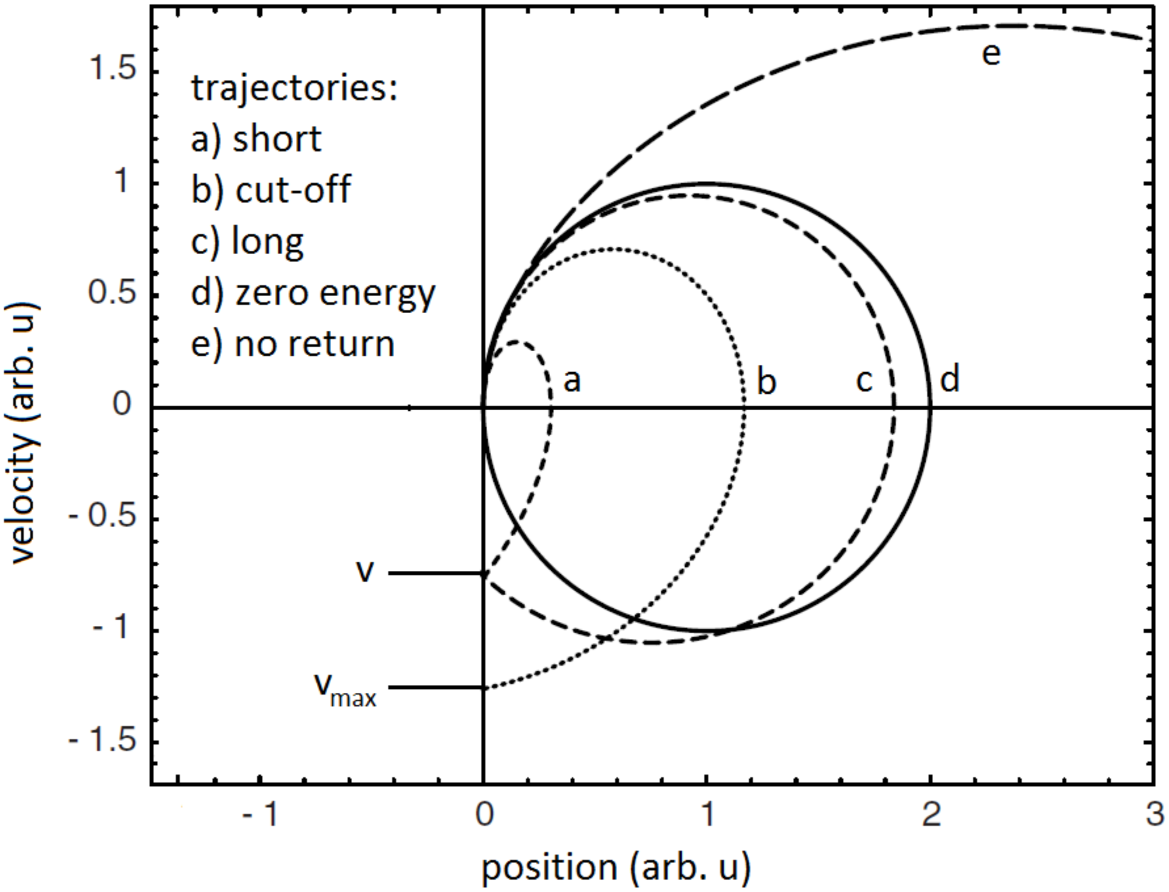

Figure 1.2: A phase plot of selected electron trajectories tunneling at different moments during a single optical cycle of the fundamental field. The traces correspond to the following electron trajectories: a) short, b) cutoff, c) long, d) zero energy, e) no return. See text for expanded description. Adapted from [37].

Several important classes of electron trajectories to note are plotted in Fig. 1.2. Each returning electron velocity, except for the cutoff, will have two corresponding trajectories, known as the short and long trajectories, and are shown in the traces (a) ($\phi = 45°$) and (c) ($\phi = 3°$) of Fig. 1.2. The cutoff trajectory is shown in trace (b) ($\phi = 17°$). The cutoff trajectory leads to what is known as the cutoff law for HHG which gives the highest photon energy:

$$E_{cutoff} = I_p + 3.17U_p. \tag{1.8}$$

The probability of tunneling is highest at the peak of the laser field and these electrons will follow trajectory (d) ($\phi = 0°$) but the electron will return to the ion with zero velocity. Finally, trajectory (e) ($\phi = -45°$) shows an electron which will never return to the parent ion.

The model developed so far in this section is a mixture of both classical and quantum mechanics. We first have a quantum representation of tunnel ionization, then the classical motion of the electron in the laser field, and finally a quantum radiative recombination. This simple semi-classical model gives an elegant analysis of HHG and relates the important elements of the process such as the harmonic cutoff as well as ionization and recombination times. However, a full quantum mechanical treatment is needed in order to decipher further quantum effects that may influence the HHG process such as quantum diffusion of wavepackets or quantum interferences. In the following subsection we present a brief summary of the quantum mechanical approach to HHG and how the three semi-classical steps are described.

1.2.3 Quantum mechanical approach to high harmonic generation

The quantum mechanical treatment of HHG is described by the Lewenstein model [38] which calculates the single atom response (SAR) during harmonic generation. The SAR is the dipole responsible for high harmonic emission for any given arbitrary pulse shape, calculated as a function of time. The electric field of the emitted high harmonics can be obtained by the second derivative of the dipole and a Fourier transform of this field will yield the generated harmonic spectrum.

The wavefunction of the electron, $\psi(t)$, in the electric field, $\mathbf{E} = \partial\mathbf{A}/\partial t$ (where $\mathbf{A}(t)$ is the vector potential), can be solved using the Schrödinger equation in the single-active electron approximation

$$i\frac{\partial\left|\psi(t)\right\rangle}{\partial t} = \left[-\nabla^2/2 + V(\mathbf{x}) - \mathbf{E}\cdot\mathbf{x}\right]\left|\psi(t)\right\rangle \tag{1.9}$$

where $V(\mathbf{x})$ is the atomic potential. This analysis now makes several assumptions and also makes use of the strong-field approximation (SFA) which is valid in the tunneling regime ($\gamma \leq 1$). The SFA assumes that once the electron is ionized to the continuum, the effect of the atomic potential, $V(\mathbf{x})$, is negligible. Furthermore, any bound state above the ground state ($\left|0\right\rangle$) can be ignored and the depletion of the ground state is neglected.

The wavefunction of the electron is now divided into two parts: one that stays in its ground state ($\left|0\right\rangle$) and a part that ionizes into the continuum:

$$\left|\psi(t)\right\rangle = e^{iI_pt}\left(a(t)\left|0\right\rangle + \int d^3\mathbf{v}\, b(\mathbf{v},t)\left|\mathbf{v}\right\rangle\right) \tag{1.10}$$

where $a(t) \cong 1$ is the ground state amplitude, $b(\mathbf{v}, t)$ are the continuum state amplitudes, and $\left|\mathbf{v}\right\rangle$ is a continuum state with momentum $\mathbf{v}$. The free oscillations of the ground state have been factored out which essentially sets the zero energy to the energy of the ground state, $\left|0\right\rangle$.

We can now calculate the time-dependent dipole moment, $\left\langle\psi(t)\right|\mathbf{x}\left|\psi(t)\right\rangle$, of the ionized electron:

$$\mathbf{x}(t) = -i\int_0^t dt_i \int d^3\mathbf{p}\cdot\mathbf{d}^*(\mathbf{p}+\mathbf{A}(t))e^{iS(\mathbf{p},t_i,t)} \times \mathbf{E}(t_i)\cdot\mathbf{d}(\mathbf{p}+\mathbf{A}(t_i)) \tag{1.11}$$

where $\mathbf{p} = \mathbf{v} + \mathbf{A}(t)$ is the canonical momentum and S is the semiclassical action which represents the phase the electron acquires, represented by

$$S(\mathbf{p}, t_i, t) = \int_{t_i}^{t} dt'' \left(\frac{(\mathbf{p} - \mathbf{A}(t''))^2}{2} + I_{\mathbf{p}}\right). \tag{1.12}$$

The dipole moment can be intuitively related to the three-step semiclassical treatment previously described as it is a product of the amplitude for each step (ionization, propagation, and recombination). To begin, the probability between a transition from ground to continuum state for the electron with momentum $\mathbf{p}$ is $\mathbf{E}(t_i)\cdot\mathbf{d}(\mathbf{p}+\mathbf{A}(t_i))$. This rate is usually calculated using a numerical approach such as the Ammosov-Delone-Krainov [39] or Yudin-Ivanov [40] method. The electron wavepacket then propagates freely under the guidance of the laser field and acquires the phase, $S(\mathbf{p}, t_i, t)$. Finally, the wavepacket radiatively recombines at time $t = t_f$ with probability $\mathbf{d}^*(\mathbf{p} + \mathbf{A}(t))$ and is typically treated as a plane wave for simplicity. The high harmonic spectra can thus be obtained by calculating the Fourier transform of the dipole moment, $\mathbf{x}(\omega_q)$.

It is important to note that this calculated dipole moment is only for the SAR while the high harmonic signal combines emission from a summation over all electron trajectories and all ionization times, t_i, which is a macroscopic sample. For high harmonic emission, the response of each atom must add coherently so that the output is a collimated beam propagating with the same k-vector as the fundamental beam. The intensity of the emitted harmonic beam is strongly dependent on the degree to which the atomic dipoles are in phase. Therefore, phase matching plays an important role in high harmonic generation. Section 1.3 will touch on several aspects of phase matching and how it affects harmonic generation efficiency.

1.2.4 Extension of HHG theory to molecular media

The extension of HHG theory from atoms to molecules is not trivial and is still a work in progress. However, we can immediately make two important modifications to the Lewenstein model. The ionization rate shall be calculated using a method appropriate for molecules such as molecular-ADK (MO-ADK) theory [41] which considers the symmetry property and the asymptotic behavior of the molecular electronic wave function, or calculations based on numerical integration of the time-dependent Schrödinger equation [42]. Also, the ground state in the recombination amplitude from the dipole moment calculation (see Eq. 1.11) can be replaced with the highest occupied molecular orbital (HOMO), obtainable using a standard quantum chemistry package such as GAMESS [43, 44].

Several other factors must be considered when dealing with molecular media in HHG. To fully understand the process, each step (ionization, propagation, and recombination) of HHG must be closely examined. For complex molecules, even the ionization step is not fully understood theoretically and the examples cited above to calculate ionization rates tend to use exploitations of the symmetry of the molecule (linear, or perhaps spherical) or single active electron approximations to simplify the problem. In terms of the electronic structure, nodes in the HOMO have been shown to suppress ionization [45] and in turn, significantly extend the HHG cutoff [46]. The fact that many molecules have closely spaced orbitals can lead to simultaneous contribution to ionization from multiple orbitals which was recently shown to be possible for HHG from aligned CO_2 molecules [31].

The propagation step may be influenced by ionization and we must consider how the outgoing electronic wavepacket can be affected. This is especially important in complex molecules that have many delocalized electrons and an ionic potential that cannot be ignored. Furthermore, one might need to not only consider the effect of the ionic potential, but also consider multiple electrons appearing in the continuum. Progress has been made in going beyond the SFA [47] for propagation calculations but working with more than two electrons is still a challenge.

The recombination step for molecules might prove to be the most complicated as one must consider the many facets of how the electronic and molecular structure can affect the incoming electron wavepacket. Do the bound electrons have influence on the returning one? Has the HOMO been distorted by the optical field enough to affect the incoming plane wave? And how will the unique molecular structure influence the recombination? The focus of molecular HHG is how to address these questions. For example, theoretical calculations have shown that laser-induced molecular vibrations in molecules can enhance or diminish HHG yield [48, 49]. Along a similar line, several studies have shown the effect of multi-centre recombination appearing as a local minimum in high harmonic spectra [50, 27].

There still does not exist a consensus regarding which effects are most important to HHG and which systems, if any, they influence. This demonstrates the importance of extending what high harmonic spectroscopists have learned about atoms and simple molecules to bigger and more complex systems in order to better understand the process as a whole. This discussion will be expanded in the following subsection.

1.2.5 Observables in high harmonic spectra

From HHG experiments, the observables we obtain are (1) the high harmonic spectrum and amplitude, and (2) the dependence of high harmonic spectra on the ellipticity of the driving laser. Typical high harmonic spectra follow a simple formula of drastic decrease for the first few harmonic orders followed by a broad plateau region then finally, a sharp cutoff. Deviations from this representation of spectra such as amplitude modulations in the plateau region or extension of the cutoff allow us to obtain useful information about the ionizing medium directly from both our observables such as signatures of molecular and electronic structure.

Cooper minimum

Modulations in high harmonic spectra can occur for a variety of reasons. Local amplitude minima, which are completely independent of the laser parameters, are directly related to the electronic structure of the atom or molecule. Since the early days of HHG, high harmonic spectra from Ar has displayed a local minimum near 48 eV [51] which more recent studies have shown to be both intensity and wavelength-independent [52, 53]. This minimum arises due to the well-known Cooper minimum (CM) in the photoionization cross-section [54]. Photoionization cross-sections for outer subshells of atoms can be calculated by integration over the bound and continuum radial wave functions for the electron, giving radial dipole matrix elements for energetic transitions between the ground and excited state. Matrix elements for the transition from the outer p-state to the continuum as a function of electron energy for Ne, Ar, and Kr are shown in Fig. 1.3 (adapted from [54]). The zero-crossing, or sign change, in the Ar and Kr curves will lead to a local minimum in the photoionization cross-sections. Since the recombination dipole matrix in HHG is, in essence, the inverse of photoionization, the CM results in an amplitude modulation of the high harmonic spectrum.

The appearance of the CM in high harmonic spectra confirms the capability of HHS to retrieve field-free electronic structure information from a target system. Some molecules have also demonstrated amplitude modulations in their partial photoionization cross-sections for lone-pair orbitals [55] since they can be associated with a particular nucleus

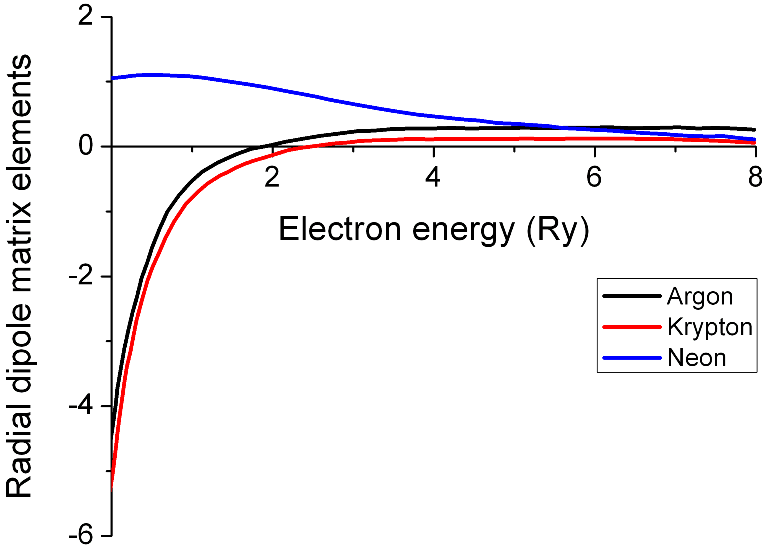

Figure 1.3: Radial dipole length matrix elements for photoionization in Ne, Ar, and Kr as a function of electron energy. Adapted from [54].

and will display atomic-like character within the linear combination of atomic orbitals description. In Chapter 3, we use HHS to investigate the Cooper minimum in molecules towards the study of electron localization in molecular orbitals.

Interference due to molecular structure

A form of amplitude modulation in high harmonic spectra that is strictly from molecules stems from interference during electron recombination with multiple centers. This type of interference is strongly dependent on the spacing of the nuclear centers as well as the de Broglie wavelength of the recolliding electron. The theoretical work of Lein *et al.* showed that processes involving electron recollision, including HHG, can demonstrate this type of interference for diatomic molecules [50]. They describe the interference minimum as a consequence of the phase of the emitted harmonic radiation and how it depends on the angle of alignment, θ, between the molecular axis and the laser polarization. For the 2D H_2^+ studied in [50], the phase of the Fourier transformed time-dependent dipole matrix (see section 1.2.3 above) is smooth with increasing θ but undergoes a sudden jump at a critical angle of 30°. Therefore, contribution to recombination at angles below the critical angle will destructively interfere with contribution from angles above it, leading to a decrease in yield for a specific harmonic which results in a local minimum in the high harmonic spectrum.

The experimental work of Kanai *et al.* confirmed this type of interference in high harmonic spectra from CO_2 [27]. They state specific interference conditions for a diatomic molecule whose HOMO has anti-bonding symmetry, such as O_2: $R \cos \theta = n\lambda$ for destructive and $R \cos \theta = (n - 1/2)\ \lambda$ for constructive interference, where λ is the de Broglie wavelength of the returning electron, θ is the angle between the molecular axis and the polarization of the laser pulse, R is the internuclear distance between the two atoms, and n is a positive integer. These conditions are reversed for molecules whose HOMOs have bonding symmetry. The CO_2 molecules can be treated like an extended diatomic with the two O atoms as nuclear centers. The HOMO of CO_2 shares the same anti-bonding symmetry as O_2. A schematic of the elongated CO_2 molecule can be seen in Fig. 1.4 (adapted from [27]). From the MO-ADK model [39], the maximum ionization rate for CO_2 occurs at the ionization angle, $\theta = 30°$, similar to O_2 and H_2. Based on

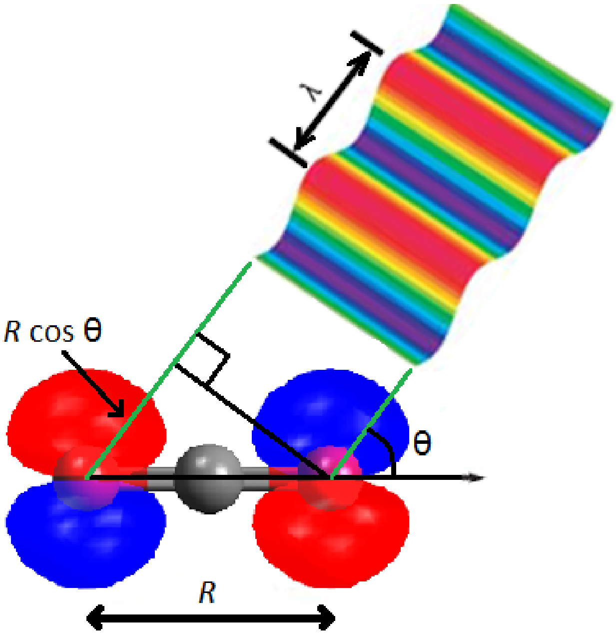

Figure 1.4: Schematic of two-center interference conditions for a diatomic molecule. λ is the de Broglie wavelength of the returning electron, θ is the angle between the molecular axis and the polarization of the laser pulse, and R is the internuclear distance. Adapted from [27].

the above equation for destructive interference, it was calculated that the recombination probability at $\theta = 30°$ for the 23^{rd} harmonic should be suppressed by several orders. The plot of the high harmonic spectra for CO_2 in [27] confirmed this suppression due to interference from multi-center recombination, represented as a local minimum. In Chapter 4, we extend the model of Kanai *et al.* to explore the interference arising from multi-center recombination for a planar polyatomic molecule with three possible centers.

Orbital interference

Another type of amplitude modulation that emerges in high harmonic spectra from molecules appears as a result of interference during ionization due to contribution of multiple molecular orbitals. In atoms, tunnel ionization is exponentially sensitive to I_P as appearance energies for higher excited states are typically many eV apart. However in molecules, higher electronic excitations can often lie within a few eV from the ground state which leads to a coherent superposition of multiple ionic states during ionization. By exploiting the symmetry of orbital structures in the HOMO, HOMO-1, and HOMO-2 of CO_2, Smirnova *et al.* showed that contributions to ionization from multiple molecular orbitals can be enhanced or suppressed depending on the angle of ionization during HHG [31]. They also revealed a local minimum in high harmonic spectra from CO_2 that was highly dependent on the laser source, stemming from interference between different ionization channels. Destructive interference occurs if the total harmonic phase difference between two ionization channels satisfies the following relation: $\Delta \mathrm{E}\ \tau^* + \phi = \mathrm{m}\pi$, where $\Delta\mathrm{E}$ is the energy difference between channels, τ^* is the return time of the electron, ϕ represents other contributions to harmonic phase, and m is an odd integer. The contributions to ϕ include the phase accumulated in the ion, the phase of the continuum electron, the phase of the recombination dipole matrix element, and phase acquired during ionization. Since the condition for destructive interference is linked to the electron return time, τ^*, the position of the minimum should therefore scale with intensity. Smirnova *et al.* concluded that in high harmonic spectra from CO_2, the intensity-dependent local minimum was a result of destructive interference between the HOMO and HOMO-2 channels. We have seen similar types of intensity dependent amplitude minima in high harmonic spectra from 1,4-cyclohexadiene and a manuscript on this topic is in preparation for publication in the near future (see Publication 9).

Additionally, interference from molecular orbitals can affect the cutoff and ellipticity dependence of high harmonic spectra. The cutoff law described above (see eqn. 1.8), states that the highest emitted photon energy during HHG is dependent on the ionization potential (I_P) and ponderomotive potential (U_P) which in turn, depends only on laser intensity and wavelength. However, evidence has shown a significant extension of HHG cutoff for molecules such as O_2 (I_P = 12.1 eV) and CO_2 (I_P = 13.8 eV) compared to their companion atoms, Xe (I_P = 12.1 eV) and Kr (I_P = 14.0 eV), respectively, at intensities greater than saturation due to suppression of ionization [46, 56]. In molecules whose HOMO exhibits nodal planes, suppression of ionization occurs due to quantum interferences when electron wave packets emitted from either side of a nodal plane destructively interfere due to their opposite phases. This suppression of ionization has also been shown in the ellipticity dependence for the double ionization signal of C_6H_6, another recollision process [45]. For atoms, the probability of recollision is maximum at linear polarization and falls off rapidly as ellipticity, ϵ, increases. This follows directly from the laws of motion governing the electron in the strong laser field. However, Bhardwaj *et al.* presented a local minimum in the double ionization signal for linear polarization with the maximum occuring at $\epsilon = 0.1$. In C_6H_6, an electron wave packet cannot be launched if the laser polarization lies in one of the two nodal planes due to destructive interference. As ellipticity increases, the destructive interference is offset by the transverse field component that compensates for initial electron momentum, forcing some of the electrons to recombine with the ionic core. Both sections of Chapter 4 present evidence of suppressed ionization obtained directly from high harmonic spectra as well as the ellipticity dependence of HHG in polyatomic molecules.

1.3 High harmonic efficiency

The low conversion efficiency from infrared light into high harmonics is presently a hindrance to the use of these light pulses in experiments and research is ongoing to improve this. Typical conversion rates are on the order of 10^{-5} to 10^{-7} [57, 58] when using 800 nm light for most HHG experiments. The efficiency of the HHG process depends on (a) a high sample density leading to coherent buildup of emitted harmonics, (b) the length of the nonlinear medium, L_{med}, (c) the absorption length of harmonics by the nonlinear medium, L_{abs}, and (d) the phase velocity matching between the fundamental and the high harmonic beams. In addition to medium dispersion, the presence of free electrons can lead to a phase velocity mismatch which limits coherent buildup to short interaction lengths. HHG efficiency is optimized by a delicate balance of these competing processes. The following subsections examine a few of these factors.

1.3.1 Phase matching

To achieve considerable HHG output, the radiation emitted in the forward direction by each atom must be in phase with the radiation emitted by each neighboring atom. This occurs when the phase velocity of the fundamental driving laser and the generated radiation is equal. In a dispersive medium, the driving laser will slip π radians out of phase with the generated radiation after a characteristic propagation distance known as the coherence length, $L_{coh} = \pi/\Delta k$, and subsequently there will be destructive interference. Δk is known as the phase mismatch and is given by

$$\Delta k_q = qk_d - k_q \tag{1.13}$$

where q is the harmonic order, k_q is the wavevector of the q^{th} harmonic, and k_d is the wavevector of the fundamental beam. The wavevector of the fundamental beam in the nonlinear medium is given by

$$k_d = k_0 \left(1 + N_a n(\lambda_0) - \frac{N_e r_e \lambda_0^2}{2\pi}\right) \tag{1.14}$$

where k_0 is the wavevector of the fundamental beam in vacuum, N_a is the density of neutrals in the sample, N_e is the density of free electrons, $n(\lambda_0)$ is the index of refraction at wavelength λ_0, and r_e is the classical electron radius [59]. The second and third terms in Eq. 1.14 correspond to medium and plasma dispersion, respectively. Similarly, the wavevector of the q^{th} harmonic beam is given by

$$k_q = qk_0 \left(1 + N_a n(\lambda_q) - \frac{N_e r_e \lambda_0^2}{2\pi q^2}\right). \tag{1.15}$$

We insert Eqs. 1.14 and 1.15 into Eq. 1.13 and assuming $(1 - 1/q^2) \approx 1$, we obtain

$$\begin{aligned} \Delta k_q &= q k_0 \left(N_a \Delta n_q - \frac{N_e r_e \lambda_0^2}{2\pi} \right) \\ &= q k_0 \left(P(1-\eta)\Delta n_q - P N_0 \eta \frac{r_e \lambda_0^2}{2\pi} \right) \end{aligned} \tag{1.16}$$

where P is the pressure in bar, η is the ionization fraction of the gas, N_0 is the particle density at $P = 1$ bar, and Δn_q is the difference in refractive index of the gas for each wavelength.

Proper phase matching is obtained by minimizing Δk_q. If HHG is produced in a waveguide, there exists a third dispersion term which affects phase mismatch and is dependent on the size of the capillary being used [60]. This dispersive term is negative and is capable of compensating for the medium and plasma dispersion terms in Eq. 1.16 by tuning the pressure in the waveguide. However, the dispersion due to plasma defocusing (second term in Eq. 1.16) is determined by the plasma density which is a function of the ionization. There thus exists a critical ionization degree above which phase matching is impossible simply by adjusting the pressure. Therefore, while an increase in intensity can be useful to generate a higher cutoff (which is a function of the quiver energy, U_p), it also serves to increase phase mismatch due to the increase in ionization. Additionally, extraneous ionization can also lead to a strong reduction of medium density which lowers the nonlinear response.

A final term which can cause phase mismatch in the HHG process is the Gouy phase shift when a Gaussian laser beam is focused [61, 62]. This geometric mismatch is a function of the distance from the focus and the laser's Rayleigh range. Thus, the contribution from the Gouy phase can be controlled by placing the focus at a different position with respect to the highest gas densities [63]. When the focus is at the centre of the nonlinear medium, the harmonic intensity is low due to poor phase matching. By focusing the fundamental beam before the nonlinear medium, phase matching on the optical axis is efficient which leads to a high regularity of the harmonics in both the spatial and spectral domains. On the other hand, focusing the fundamental beam after the medium achieves efficient phase matching off the optical oxis which can distort the spatial and temporal profiles of the harmonics.

1.3.2 Quasi phase matching

Quasi phase matching (QPM) is a technique used to supplement traditional phase matching to increase HHG efficiency and is a well-known concept in nonlinear optics [64]. QPM is typically used when pressure tuning is not possible such as the case where ionization is too high. The goal is to generate only radiation that constructively interferes with previously generated radiation while eliminating harmonic emission from regions having destructive phase. For a nonlinear medium that is isometric, which is the case for most HHG experiments, the proper approach is to create a periodic modulation of the HHG amplitude.

Several approaches have already been tested to implement QPM into HHG experiments. Some examples include using a modulated hollow-core fibre to periodically vary the intensity of the fundamental laser driving the HHG conversion [65, 66] by creating regions of alternating bore diameter. In another case, the coupling excitation of multiple modes into a waveguide can result in the rapid periodic variation of the axial intensity [67]. Periodically varying the pressure of the nonlinear medium is another QPM scheme where alternating regions of high and low pressure allow the use of an unmodulated fundamental beam [68]. Finally, all-optical methods of QPM are also possible by using counter propagating pulses to effectively disrupt harmonic emission in a periodic fashion along the optical axis [69, 70].

1.3.3 Reabsorption of harmonic radiation

The reabsorption of harmonic radiation is an important issue when trying to optimize efficiency. For phase-matched harmonics, the coherent signal grows with the increase of the interaction length as well as gas pressure. However, attenuation of the signal occurs due to interaction of harmonic photons with neutral media. Thus, there exists an optimal interaction length and pressure for maximum harmonic conversion efficiency. The number of photons emitted per unit time and area, N_{out}, is related to these factors by:

$$N_{out} \propto \rho^2 A_q^2 \frac{4L_{abs}^2}{1+4\pi^2(L_{abs}^2/L_{coh}^2)} \left[1+\exp\left(-\frac{L_{med}}{L_{abs}}\right) - 2\cos\left(\frac{\pi L_{med}}{L_{coh}}\right)\exp\left(-\frac{L_{med}}{2L_{abs}}\right)\right] \tag{1.17}$$

where A_q is the amplitude of the atomic response at the harmonic frequency ω_q, L_{coh} is the previously defined coherence length, L_{med} is the medium or interaction length, and $L_{abs} = 1/\sigma\rho$ is the absorption length with σ being the ionization cross section and ρ being the gas density (from[71]).

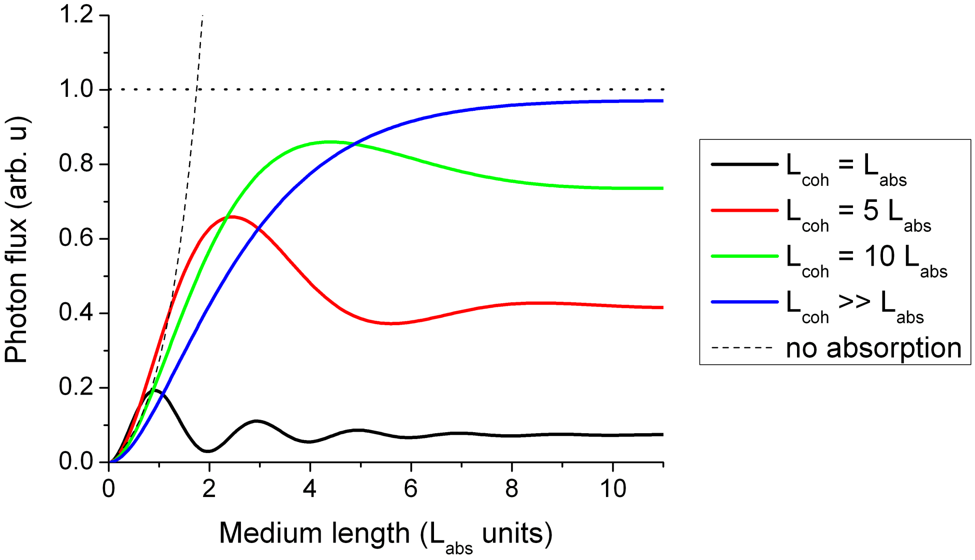

Figure 1.5: Number of on-axis emitted photons (arb. u) as a function of the medium length (in units of absorption length). The dashed line corresponds to a zero absorption case.

Figure 1.5 shows the variation of N_{out} for several different coherence lengths. It is evident that even at very high coherence length, the harmonic emission will saturate once the interaction length is longer than a few absorption lengths. This study showed that the optimizing conditions found were $L_{med} > 3L_{abs}$ and $L_{coh} > 5L_{abs}$. The study also found that the saturation point in Figure 1.5 is independent of density and increases as $|A_q/\sigma|^2$. Therefore the optimization of the HHG efficiency requires all three of the previous conditions. The use of a gas cell for HHG, along with a loose focusing geometry, is an effective method to increase L_{med} compared to a traditional pulsed valve [71]. Improving phase matching between the fundamental and harmonic fields would yield greater values of L_{coh} and as noted above, significant research is being conducted on this topic. We discuss many factors of high harmonic reabsorption in Chapter 2.

1.3.4 Wavelength scaling of HHG

Traditionally, HHG experiments are conducted using 800 nm light from a Ti:Saph laser system, a tabletop laser source available in numerous labs around the world. New developments for the Ti:Saph laser system are constantly in progress with recent advances including pulse durations near the single oscillation limit [14, 15], intensities up to 10^{18} W/cm^2 with less than 1% energy fluctuations [16], and electric field phase stability within the pulse envelope of less than 100 as [17].

However, 800 nm light is not suitable for studying HHG from complex molecules as most have their I_{P} in the range of 8–10 eV and saturation intensities around 0.2–0.4 $\times 10^{14}$ W/cm^2. We recall the cutoff law from 1.2.2 that showed the maximum photon energy attainable scales as $\hbar\omega = I_p + 3.17U_p$, where $U_p \propto I\lambda^2$. Such low values of ionization would be inadequate to obtain a broad enough range of HHG frequencies necessary to study how molecular or electronic dynamics can affect the HHG process. Research has shown the requirement for emitted harmonic spectra to exceed $\sim$50 eV in order to see signatures of these effects [72].

Instead, the use of longer infrared wavelength light (λ = 1 - 2 μm) has become crucial for HHG in molecules. The energy of the recolliding electron scales as λ^2 so the harmonic cutoff can be extended to much greater photon energies compared to 800 nm light while the laser intensity is kept below the saturation intensity of the molecule. Additionally, the spacing of harmonics in the emitted spectrum decreases significantly as the wavelength is increased since the fundamental photon energy is inversely proportional to wavelength. This leads to a higher spatial resolution for HHS. A picture of high harmonic spectra from Xe are shown in Figure 1.6 using λ = 800, 1300, and 1800 nm light, showing the significant extension of the harmonic cutoff (higher photon energies) as well as the decrease in harmonic spacing when using similar laser intensities ($I \sim 10^{14}$ W/cm^2) and multi-cycle pulses. We recall that phase mismatch was heavily dependent on plasma dispersion. The use of lower laser intensities helps to offset these detrimental effects from the ionized medium [73, 74], thus enabling the use of higher gas pressures to increase harmonic flux.

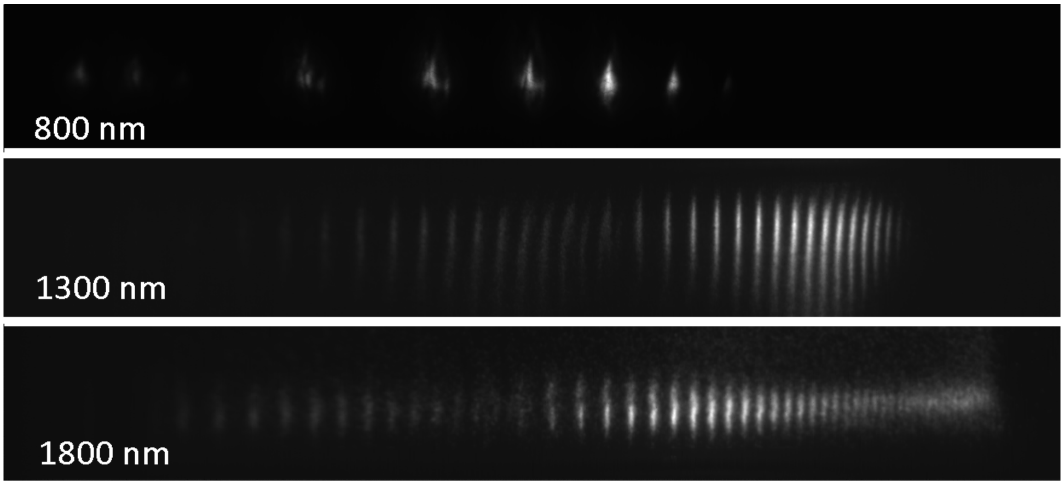

Figure 1.6: High harmonic spectra from Xe using λ = 800, 1300, and 1800 nm light.

The consequence of using longer wavelengths for HHG is that the electron wavepacket will spend more time in the continuum resulting in a large transverse spreading and thus, reducing the probability of recollision. A formulation to calculate the recombination probability comes from the saddle point analysis from [38] with solutions given by Yakovlev *et. al.* [75] where the amplitude, a_{pr}, for an electron born at time t_i returning to its parent ion at time t, has the form

$$a_{pr}(t) \propto \left(\frac{2\pi}{t - t_i}\right)^{3/2}. \tag{1.18}$$

The probability for recombination, $|a_{pr}(t)|^2$, is thus

$$|a_{pr}(t)|^2 \propto \left(\frac{2\pi}{t - t_i}\right)^{3} \tag{1.19}$$

where the time the electron spends in the continuum, $t - t_i$, is directly proportional to λ. From this transverse spreading of the electron wavepacket, we see already a decrease of the HHG yield by λ^3. Additionally, the increase in spectral bandwidth by a factor of λ^2 should cause an equal decrease in HHG yield by the same factor if the XUV beam is spread across the entire bandwidth and remains constant. Therefore the yield should fall at minimum as λ^{-5}. In accordance, several theoretical [76, 77] and experimental [78] studies have shown the yield to decrease on the order of $\lambda^{-(5-7)}$. It is necessary to find a balance between using a long wavelength to extend the cutoff while increasing gas density and utilizing improved phase matching to balance the lower yields. For our studies, we found that wavelengths in the range of $\lambda = 1300 - 1800$ nm were a good compromise between a significant increase in cutoff and adequate HHG yield. We are able to partially offset the wavelength scaling effects by using higher pressures in our experiments.

Chapter 2

The comparison of high harmonic sources

2.1 Comparison and real-time monitoring of high-order harmonic generation in different sources (Publication 1)

J.-P. Brichta, **M. C. H. Wong**, J. B. Bertrand, H.-C. Bandulet, D. M. Rayner, and V. R. Bhardwaj
Comparison and real-time monitoring of high-order harmonic generation in different sources
Physical Review A **79**, 033404 (2009)

2.1.1 Author contribution

The published results come from experiments performed by M. C. H. Wong, J.-P. Brichta, H.-C. Bandulet and V. R. Bhardwaj at ALLS in Varennes, QC. M. C. H. Wong designed both the semi-infinite and finite gas cells used in the experiment. M. C. H. Wong, J.-B. Bertrand, D. M. Rayner, and V. R. Bhardwaj performed preliminary experiments (unpublished data) at NRC in Ottawa, ON. J.-P Brichta and M. C. H. Wong conducted the analysis of the results and created the figures. J.-P. Brichta wrote the first draft of the manuscript. All authors contributed to the final manuscript.

PHYSICAL REVIEW A **79**, 033404 (2009)

Comparison and real-time monitoring of high-order harmonic generation in different sources

J.-P. Brichta,[1] M. C. H. Wong,[1] J. B. Bertrand,[1,2] H.-C. Bandulet,[3] D. M. Rayner,[2] and V. R. Bhardwaj[1,*]
[1]*Department of Physics, University of Ottawa, 150 Louis-Pasteur, Ottawa, Ontario, Canada K1N 6N5*
[2]*National Research Council of Canada, 100 Sussex Drive, Ottawa, Ontario, Canada K1A 0R6*
[3]*Institut National de la Recherche Scientifique–Centre Énergie, Matériaux et Télécommunications, 1650 boulevard Lionel-Boulet, Varennes, Québec, Canada J3X 1S2*

(Received 8 October 2008; published 11 March 2009)

We compare the generation of coherent extreme ultraviolet (xuv) photons in argon from three different high-order harmonic sources: a semi-infinite gas cell, a finite gas cell, and a pulsed valve. We demonstrate photoionization of the background gas by the coherent xuv photons as an alternative to xuv spectroscopy for real-time and in-line monitoring of the high-order harmonics. Using this technique for measuring photocurrent, we show that the gas cells produce 50–100-fold brighter harmonics than the pulsed valve, with an estimated conversion efficiency of 10^{-4}. The spectral distribution of the harmonics produced in the gas cells peaks at the 27th harmonic compared to the 19th harmonic in the pulsed valve. We attribute this difference to the interplay between phase matching and absorption.

DOI: 10.1103/PhysRevA.79.033404 PACS number(s): 32.80.Rm, 42.65.Ky

I. INTRODUCTION

Advances in ultrafast laser technology have enabled the development of table top sources of xuv and soft x-ray light through the process of high harmonic generation (HHG) [1,2]. High energy photons are produced in a nonlinear medium when an electron, removed from an atom or a molecule by the laser field, is driven back to the ion and undergoes recombination [3,4]. HHG opens new frontiers in science by extending nonlinear optics into the xuv region [5] and pushing ultrafast science to the attosecond domain [6], thus enabling: xuv spectroscopy, imaging of molecular orbitals [7], and electron motion. However, progress in attosecond science is presently hindered by the lack of high brightness harmonic sources. Research has been ongoing to improve HHG efficiency.

The efficiency of the HHG process depends on: (a) a high density of atoms leading to coherent buildup of light as it propagates through the nonlinear medium, (b) the length of the nonlinear medium, (c) absorption of harmonics by the nonlinear medium, and (d) phase velocity matching between the fundamental and the harmonic fields. In addition to medium dispersion, the presence of free electrons can lead to a phase velocity mismatch, which limits coherent buildup to short interaction lengths. The HHG efficiency is optimized by a delicate balance of these competing processes.

HHG from noble atoms in gas phase is the most widely used technique. However, laser ablation of solids provides an alternative, especially at lower harmonics [8]. Gas jets produced by a pulsed valve (PV) are a common source of high harmonics with typical medium lengths of 1–2 mm and a maximum on-axis pressure of 10 Torr. Conversion efficiencies of about 10^{-5} in the 30 nm [9] and 10^{-7} in the 13 nm [10,11] region were obtained using high-power IR laser pulses and a loose focusing geometry. The efficiency of HHG in gas jets is determined solely by phase matching and is dominated by Gouy phase shift and medium dispersion. It is optimized by controlling the relative positions of the laser focus and the gas jet to balance both the Gouy phase shift and dipole phase shift [12]. A technical limitation of such a source is the repetition rate of the pulsed valve, which is typically much less than that of the laser.

In contrast, static gas cells permit the use of higher atomic densities and longer medium lengths, leading to higher conversion efficiencies due to their quadratic dependence. In addition to phase matching, absorption of harmonics by the medium starts to play an important role as the medium length gets longer [13]. For interaction lengths on the order of the confocal parameter of the laser, as in the case of finite gas cells (FGC), conversion efficiencies of 10^{-6} have been reported [14]. In semi-infinite gas cells (SIGC) [15], where the interaction length is several times the confocal parameter, pressures in excess of 100 Torr were used for efficient generation of high harmonics.

High-order harmonics can be generated in hollow capillary tubes [16] with conversion efficiencies of greater that 10^{-6}, producing more that 0.2 nJ per harmonic order from a modest 150 μJ laser pulse. The efficiency of high harmonics generated in the above sources can be further enhanced by employing techniques such as adaptive pulse shaping, both in the frequency [17] and spatial domains [18], and by utilizing orthogonally polarized two-color (fundamental and frequency-doubled) driving lasers [19]. Despite the numerous studies on HHG efficiency in different types of sources, there is a lack of direct comparison between them.

In this paper, we use argon as the medium to compare HHG in a gas jet, a finite gas cell, and a semi-infinite gas cell. We show that the gas cells produce 50–100 times more intense harmonics relative to the gas jet. This direct relative comparison among the different sources was made possible by introducing an alternate technique of monitoring the harmonics by measuring the photocurrent produced ionization of the background gas by the high energy photons. The standard technique involves using an x-ray spectrometer. While the spectrometer provides spectral information, the efficiency of the microchannel plate detector varies with wavelength

---

[*] ravi.bhardwaj@uottawa.ca

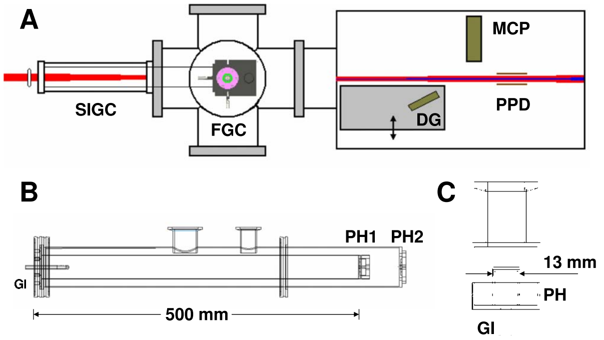

FIG. 1. (Color online) (a) Experimental setup for generation of xuv photons. SIGC, semi-infinite gas cell; FGC, finite gas cell; DG, dispersive grating. The grating sits on a motorized stage and must be removed from the beam to measure photocurrent with the parallel plate detector; MCP, microchannel plates with phosphor screen; PPD, parallel-plate detector. (b) Semi-infinite gas cell. GI, gas input; PH1, pinhole (100–250 μm); PH2, 1 cm pinhole. (c) Finite gas cell. GI, gas input; PH, 4×600 μm pinholes.

and absolute calibration is difficult. Often used in conjunction with a spectrometer, an x-ray photodiode measures short wavelength photons but must be calibrated with known sources such as a synchrotron. Unlike the standard methods, our technique can monitor high harmonics in real time and in-line, without intervention in or depletion of the x-ray beam. This is important for many studies in the attosecond domain.

II. EXPERIMENT

The schematic of the experimental setup for HHG is shown in Fig. 1. Linearly polarized laser pulses from a Ti:sapphire regenerative amplifier (0.8 mJ, 35 fs, 800 nm, 100 Hz) are focused through a 1 mm thick fused silica window onto the gas target with an achromatic lens of focal length 75 cm. The target is either a gas jet produced by a pulsed valve or two different types of gas cells. In all cases, the harmonics are produced at the same location in the source chamber. The source and detector chambers are differentially pumped through a 3 mm diameter tube that is 5 cm in length. The different harmonic orders are detected using a grazing-incidence concave grating (1200 lines mm^{-1}) which disperses and focuses them onto a microchannel plate (15 mm $\times$ 75 mm) coupled to a phosphor screen. The screen is imaged with a charge coupled device (CCD) camera. In the typical operating configuration, harmonic orders 11–49 are detected. The harmonics are optimized by slightly moving the laser focus with respect to the target and by adjusting the laser chirp.

When the grating, positioned on a translation stage, is removed from the laser path, the harmonic beam passes through a copper parallel plate detector. The parallel plate detector and microchannel plates are equidistant from the location of high-order harmonic generation. The active area of the detector plates is approximately 10 mm $\times$ 75 mm with an 8 mm separation. Ions of the background gas in the detection chamber ($P \sim 5 \times 10^{-7}$ Torr) created between the parallel plates by the high harmonic beam are detected by applying a bias of +100 V on one of the plates and measuring the photocurrent on the other plate with a picoammeter. A larger bias voltage does not improve the signal collection efficiency. Since a major constituent of the background gas is nitrogen, which has an ionization potential of 15.58 eV, harmonics of the 11th order or higher are required for single photon ionization. As a result, the photocurrent scales linearly with photon flux. Since harmonics lower than the 11th order are also produced, our photocurrent measurement underestimates the total high harmonic flux. A small amount of argon is also present in the background.

Both of our gas cells employ a differential pumping geometry to reduce the rate of gas flow into the source and detection chambers. The SIGC consists of a cylindrical inner tube (500 mm long, ϕ 36 mm) surrounded by a cylindrical outer tube (575 mm long, ϕ 60 mm). Up to 200 Torr of gas pressure is delivered into the inner tube by a ϕ 6 mm stainless steel tube. The gas pressure is monitored by a Baratron gauge. The inner and outer tubes are separated by a 150 μm diamond pinhole (Fort Wayne Wire Die, Inc.). The outer tube has a 1 mm pinhole and is pumped by a roughing pump (500 L min^{-1}). The laser is focused to a spot directly before the diamond pinhole, about 50 mm from the center of the source chamber.

The FGC consists of a small cylindrical inner cell (16 mm tall, ϕ 11 mm) and larger cylindrical outer cell (28 mm tall, ϕ 30 mm). Gas is delivered to the inner cell through a 6 mm Teflon tube and pressure is monitored with a Baratron gauge. The inner cell has two inline pinholes (ϕ 600 μm) that lead to the outer cell. The outer cell also has two inline pinholes (ϕ 600 μm) which lead to the source chamber. The outer cell is pumped by a roughing pump (500 L min^{-1}) similar to the SIGC. The FGC has an effective interaction length of $\sim$15 mm and is mounted on an *XYZ* manipulator to permit precision alignment with respect to the laser axis.

The PV has a 500 μm aperture with a 200 μs opening time and operates at 10 Hz to avoid overpressuring the source chamber. The pulsed valve is mounted on an *XYZ* manipulator and is positioned so that the interaction length is $\sim$1 mm. Stagnation pressures of up to 5 atm were used. We estimated the on-axis pressure in the gas jet based on dynamical arguments [20]. Specifically, for a stagnation pressure of P_0, the pressure in the gas jet, P, is given by

$$\frac{P_0}{P} = \left(1 + \frac{\gamma - 1}{2} M^2\right)^{\gamma/(\gamma-1)}, \tag{1}$$

where $\gamma = 5/3$ for a monatomic gas, $M = A(x/D)^{\gamma-1}$ is the Mach number, A is a constant that depends on γ and is 3.26 for a monatomic gas [21], x is the distance from the nozzle, and D is the nozzle diameter. With the laser positioned at a typical downstream distance of $\sim$1 mm, a stagnation pressure of 2300 Torr produces an on-axis pressure of 7 Torr. The atomic density in a gas jet follows a Lorentzian distribution, and over the length of the laser-jet interaction region the pressure should be at least half of the on-axis pressure [22] or approximately 3.5 Torr. A fast ionization gauge from Beam-Dynamics, located below the pulsed valve, is used to

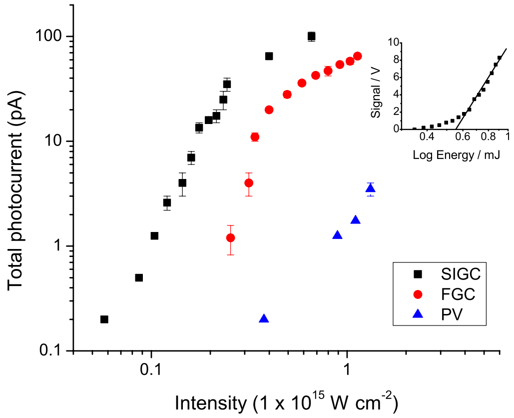

FIG. 2. (Color online) Total photocurrent as a function of laser intensity for different gas cell geometries. The photocurrent was recorded under optimum pressure conditions which were 43 Torr for the semi-infinite gas cell (black squares), 7 Torr for the finite gas cell (red circles), and 3.5 Torr for the pulsed valve (blue triangles). The inset graph shows the intensity calibration performed with the pulsed valve and a fast ionization gauge (see text). It indicates a saturation energy of 560 μJ, which for argon corresponds to the saturation intensity of 2.37×10^{14} W cm^{-2}.

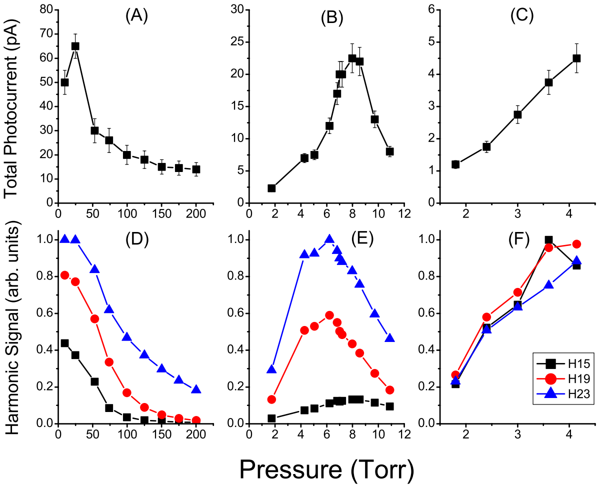

FIG. 3. (Color online) Pressure dependence of total photocurrent (top panel) and individual harmonics (bottom panel) measured using the x-ray spectrometer for [(a) and (d)] the semi-infinite gas cell, [(b) and (e)] the finite gas cell, and [(c) and (f)] the pulsed valve. The laser intensity was 3×10^{14} W cm^{-2} for the gas cells and 6×10^{14} W cm^{-2} for the pulsed valve. Error bars are a result of shot-to-shot variation in the recorded photocurrent. In the bottom panel, the harmonics shown are the 15th (black squares), 19th (red circles), and 23rd (blue triangles).

monitor the gas density and the position of the laser focus with respect to the gas jet by measuring the relative ion signal produced by the laser.

III. RESULTS AND DISCUSSION

For the three HHG sources that were investigated, the total photocurrent measured by the parallel plate detector as a function of the laser intensity is shown in Fig. 2. For each source an experimentally determined optimum gas pressure, P, was used. The photocurrent, *vis-à-vis* the harmonic signal from the SIGC (P=25 Torr), grows by nearly 3 orders of magnitude over an intensity range of 5×10^{13} W cm^{-2}–2×10^{14} W cm^{-2}, beyond which the signal starts to saturate. A similar trend is observed for the FGC photocurrent (P=7.0 Torr) in the intensity range of 2×10^{14} W cm^{-2}–4×10^{14} W cm^{-2}. However, the harmonic signal is lower by a factor of 2–20 compared to the SIGC. In contrast, a relatively large intensity of $\sim 3 \times 10^{14}$ W cm^{-2} is required to record any photocurrent when using the PV (stagnation pressure of 2 atm) and the photocurrent is at least 2 orders of magnitude smaller than the SIGC. Unlike in the gas cells, no saturation of the harmonic signal is observed until the maximum intensity is reached. In all sources, the lowest measurable photocurrent is 0.2 pA, which is limited by our ability to distinguish the signal from the background current of <0.05 pA. The error bars on the vertical axis represent fluctuations in the harmonic signal due to shot-to-shot variations in pulse energy.

The observed saturation of the photocurrent (harmonic signal) in the gas cells is the result of a combination of neutral atom depletion and the free-electron contribution to phase mismatch. The laser intensity is accurately determined by measuring the saturation intensity of argon atoms as shown in the inset of Fig. 2. We used the fast ionization gauge below the pulsed valve to record the ions produced by the laser as a function of pulse energy. When plotted in a semi-log plot the intercept on the energy axis gives the saturation intensity [23]. The saturation intensity of argon is 2.4×10^{14} W cm^{-2}.

Optimum gas pressures used in Fig. 2 are obtained by studying the pressure dependence of the total photocurrent (top panel in Fig. 3) and the intensity of individual harmonics with the xuv spectrometer (bottom panel in Fig. 3). For the latter, the signal strengths for H13–H23 were measured by integrating across the MCP image in those regions where the harmonics appeared. All three HHG sources have very different pressure dependencies.

In the SIGC, the harmonic signal reaches a maximum near 25 Torr and rapidly decreases due to stronger absorption of the harmonics at higher pressures. At 25 Torr, the typical absorption length is about 0.5 mm for the 15th and 19th harmonics whereas it is twice as long for the 23rd harmonic, leading to a stronger signal. On the other hand, the signal strength from the FGC rises at first due to increasing number density, maximizes at a pressure of 7 Torr, and then decreases as the absorption dominates over the 15 mm effective interaction length. Finally, the PV never reaches a critical point at which the harmonic signal is limited by absorption. At a pressure of 3.5 Torr, the absorption length would be approximately 4 mm, which is much longer than the interaction length. As a result, the signal strength rises linearly with stagnation pressure. With their larger number densities, gas cells are essential for efficient harmonic generation.

We now show that the photocurrent measured by the parallel plate detector is due to photoionization of the back-

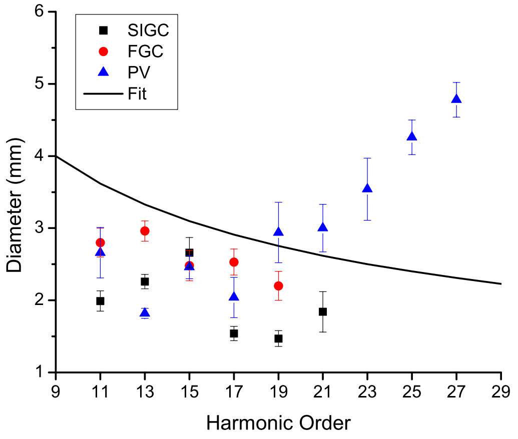

FIG. 4. (Color online) Diameter of harmonic beam at parallel plate detector measured for the semi-infinite gas cell (black squares), finite gas cell (red circles), and pulsed valve (blue triangles). The fit line plots the relationship $D_0/\sqrt{q}$, where D_0 is 12 mm in this case.

ground gas by the high order harmonics. First, by removing argon from the gas cells and turning off the gas jet, the measured photocurrent dropped to the background value. Second, by increasing the background gas density in the detection chamber, the photocurrent signal increased proportionately, as expected in single photon ionization. Third, by measuring the diameter of the harmonic beam at the detector, we ensured that the observed signal was due to ions produced and not due to the photoelectric effect. Since copper has a work function of 4.7 eV, harmonics higher than the third order could produce photoelectrons if they are incident on the detector. To measure the diameter of the harmonic beam we used the spectral images obtained by the xuv spectrometer. Since the harmonics are focused by the grating along one axis, their spatial extent along the other axis provides beam divergence.

The diameter of the harmonic beam for different orders at the parallel plate detector is shown for all three sources in Fig. 4. The recorded beam diameter is substantially less than the 8 mm separation between the parallel plates, which confirms that the photoelectric effect does not contribute to the measured photocurrent. For both gas cells, the beam diameter tends to decrease with increasing harmonic order. This is expected from the simple expression of the dipole moment at the qth harmonic frequency, which according to lowest order perturbation theory, varies as the qth power of the incident field. The solid line in Fig. 4 is the fit to $D_0/\sqrt{q}$, where D_0 is the diameter of the fundamental, measured to be 12 mm. However, for the PV, the beam diameter increases slightly with the harmonic order, as observed in previous experiments [24]. The spatial characteristics of the harmonics depend on (a) the position of the laser focus with respect to the gas jet, and (b) on the spatial profile of the driving field. Divergence of harmonics was found to change by varying the aperture size near the input window. Unlike the earlier experiments with semi-infinite gas cells [15], we did not observe any aperture effect on the beam divergence or HHG intensity.

From the total photocurrent measured by the parallel plate detector we can estimate the HHG conversion efficiency. This estimate will be greatly influenced by any errors in our assumptions of the number of ions, the molecular density, the size of the harmonic beam, the interaction volume, and the ionization cross sections. Assuming the background molecules in the detection chamber are mostly nitrogen and that each molecule is singly ionized by the high harmonic beam, 100 pA of measured photocurrent corresponds to 6.24×10^8 ions s^{-1}. Harmonics lower than the 11th order cannot contribute to the photocurrent signal, assuming the probability for multiphoton ionization to be low. The number of ions $s^{-1}\,cm^{-3}$, r_i, produced by the harmonic beam can be expressed as $r_i=\rho\sigma J_{\mathrm{HHG}}$, where ρ is the molecular density (molecules cm^{-3}) in the interaction region, σ is the photoionization cross section measured in cm^2, and J_{HHG} is the harmonic photon flux measured in photons $s^{-1}\,cm^{-2}$. Assuming that only ions produced in the detector volume will contribute to the measured signal, $r_i=N_i/V=1.04\times10^8$ ions $s^{-1}\,cm^{-3}$, where $N_i=6.24\times10^8$ ions s^{-1} (as above) and $V=6$ cm^3. With a constant pressure of 1×10^{-6} Torr, $\rho\sim2.45\times10^{10}$ cm^{-3}.

The photoionization cross section of N_2 for each harmonic energy is taken from [25] and ranges from $\sigma\simeq8-25\times10^{-18}$ cm^2 over the spectral range involving 11–49 harmonics. J_{HHG} is then calculated as a function of harmonic order and has a typical value of $\sim3\times10^{14}$ photons $s^{-1}\,cm^{-2}$. The power out is then determined by $P_{\mathrm{out}}=J_{\mathrm{HHG}}AE$, where A is the area of the qth harmonic at the detector, approximated by $A=\pi(1.2/2\sqrt{q})^2$, and E is the single-photon energy of the qth harmonic multiplied by the relative abundance of that harmonic, as determined by the spectral image obtained with the spectrometer. Given an input power of 80 mW, we estimate single order conversion efficiencies as high as 10^{-4} for the 27th harmonic produced in a semi-infinite gas cell.

The three sources used in the experiment produced different harmonic spectra as shown in Fig. 5. The SIGC spectrum shows a relatively narrow distribution, with more than half of the signal coming from the 23rd to 31st harmonic orders. The most intense harmonic is the 27th. The FGC spectrum is broader and peaks at the 25th harmonic. In both gas cells, the harmonic intensity drops rapidly by 2 orders of magnitude between the 29th and 39th harmonics. In contrast, the spectrum of the PV peaks at the 19th harmonic, but has a broad plateau, with similar intensities in the range of the 15th–23rd harmonics. A rapid cutoff is observed past the 23rd harmonic. For all three sources, the harmonic spectrum exhibits a local minimum at the 37th harmonic which can be attributed to the Cooper minimum (~50 eV) in argon [26,27]. This trend was observed to be independent of laser intensity.

We show that the differences in the harmonic spectra of the gas cells and the gas jet are a result of interplay between phase matching conditions and absorption of the harmonics. Efficient generation of high harmonics depends on three length parameters [13]; medium length L_{med}, absorption length $L_{\mathrm{abs}}=1/\rho\sigma$, and coherence length $L_{\mathrm{coh}}=\pi/\Delta k$. The phase mismatch between the qth harmonic and the fundamental fields is given by $\Delta k=k_q-qk_0$, where k_q and k_0 are harmonic and fundamental wave vectors, respectively. In

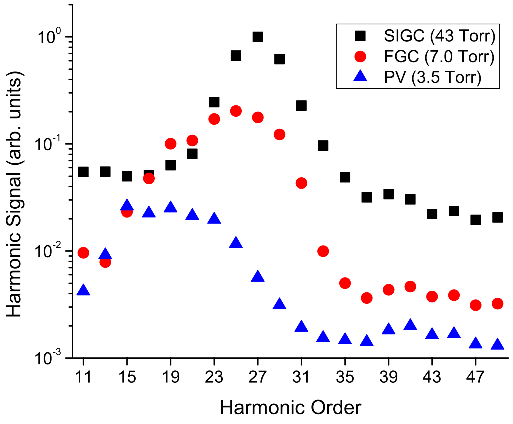

FIG. 5. (Color online) Observed high harmonic spectrum for different gas sources. The laser intensity is 3×10^{14} W cm^{-2} for the semi-infinite gas cell (black squares) and the finite gas cell (red circles). The pulsed valve data (blue triangles) were recorded with a laser intensity of 6×10^{14} W cm^{-2}.

free space, the propagation constant of light with vacuum wavelength λ in a neutral gas medium is given by

$$k=\frac{2\pi n_g(\lambda)}{\lambda}, \tag{2}$$

where the index of refraction is $n_g=1+P\delta(\lambda)$, with the pressure, P, in atmospheres and the gas dispersion function, $\delta(\lambda)$, is given by a suitable empirical relationship [28]. In general, empirical relationships are difficult to deduce beyond the UV, and we use calculated data [29] for wavelengths shorter than 140 nm. For sufficiently large laser intensities partial ionization of the medium occurs and the index of refraction is modified as

$$n_g=1+(1-\eta)P\delta(\lambda)+(1-\eta)n_2I-\eta PN_{\text{atm}}r_e\lambda^2/2\pi, \tag{3}$$

where N_{atm} is the number density at atmospheric pressure, η is the ionization fraction, and r_e is the classical electron radius. The nonlinear index of refraction, $n_2\sim9.9\times10^{-18}$ cm^2 W^{-1} atm^{-1} [30], has negligible effect at our intensities. The phase mismatch then becomes

$$\Delta k=\eta PN_{\text{atm}}r_e(q\lambda_0-\lambda_q)-\frac{2\pi(1-\eta)P}{\lambda_q}[\delta(\lambda_0)-\delta(\lambda_q)]. \tag{4}$$

The ionization fraction, η, was calculated using the ADK theory of tunnel ionization [31] at similar intensities to those used in the experiment. For an argon atom and a pulse duration of 35 fs, η is $\sim$0.08 at 4×10^{14} W cm^{-2} and $\sim$0.42 at 7×10^{14} W cm^{-2}. These values were used in calculating Δk. We then calculated the number of qth harmonic photons per unit time and area emitted on-axis, which is proportional to

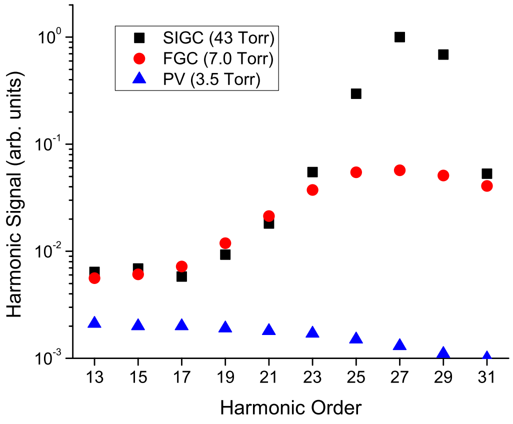

FIG. 6. (Color online) Theoretical harmonic signal for the SIGC (black squares), FGC (red circles), and PV (blue triangles) calculated using Eq. (5). The ionization fraction is η=0.08 for the SIGC and FGC, and η=0.42 for the PV, corresponding to laser intensities of $I=4\times10^{14}$ W cm^{-2} and $I=7\times10^{14}$ W cm^{-2}, respectively.

$$N_{\text{out}}\propto\rho^2A_q^2\frac{4\rho^2L_{\text{abs}}^2}{1+4\pi^2(L_{\text{abs}}^2/L_{\text{coh}}^2)}\left[1+\exp\left(-\frac{L_{\text{med}}}{L_{\text{abs}}}\right)-2\cos\left(\frac{\pi L_{\text{med}}}{L_{\text{coh}}}\right)\exp\left(-\frac{L_{\text{med}}}{2L_{\text{abs}}}\right)\right], \tag{5}$$

where A_q is the amplitude of the atomic response approximated to be $(1-\eta)I^3$, where I is the laser intensity.

The theoretical spectra for the gas cells and the gas jet are calculated with Eqs. (4) and (5) and plotted in Fig. 6, using similar intensities as in the experiment. We see a qualitative agreement between our experimental results and the theoretical calculation. Note that harmonics higher than the 31st are not included in the theoretical spectra due to the lack of dispersion data. In the case of the PV, the HHG efficiency is low due to lower number densities. The number density can be increased to some extent by increasing the gas load, but there are strict physical limitations on how much gas pressure the PV can accommodate. Since the medium length of $\sim$1 mm is much shorter than the typical absorption length, even in the strongly absorbing region near H15 ($\sim$3 mm at 3.5 Torr), absorption of the generated harmonics by the medium is negligible. As the ionization fraction increases with intensity, phase matching for higher harmonics cannot be achieved, resulting in the observed decrease in HHG efficiency.

The harmonic distribution for the two gas cells can be explained in terms of absorption and phase matching. The higher gas densities in the cells lead to lower absorption lengths, especially around the 15th harmonic. As a result, lower order harmonics are absorbed by the medium in which they are produced. Higher order harmonics have lower efficiency due to phase matching problems caused by ionization. As the ionization fraction increases, the peak in the spectral distribution shifts toward lower harmonics. The interplay between phase matching and absorption gives rise to the observed distribution with a peak around the 27th harmonic.

IV. CONCLUSION

By monitoring the photoionization of a background gas by the xuv photons produced via HHG, we have made a direct comparison of high harmonic generation in an argon-filled pulsed valve, a 11 mm finite gas cell, and a semi-infinite gas cell. Under optimal pressure conditions, we have shown that the harmonic efficiency in finite and semi-infinite gas cells is, respectively, 50 and 100 times that which is produced in pulsed valve. The strongest harmonic emission was obtained with the semi-infinite gas cell, which had an estimated conversion efficiency of $\sim 10^{-4}$. We show that the spectral distributions in both the gas jet and the cells are different due to the role of phase matching and absorption. Our results reaffirm that large conversion efficiencies cannot be achieved by simply using higher atomic densities and longer medium lengths, because, while the efficiency depends quadratically on these two parameters, it also depends on the negative exponential of their product. As a result, absorption of harmonics starts to play a critical role along with phase matching. Further enhancements in HHG efficiency depend on absorption management. By far the most promising technique to efficiently produce high harmonics employs successive sources to modulate the atomic number densities along the interaction length in order to achieve quasiphase matching while simultaneously minimizing absorption [32]. This and similar density modulation techniques might enable one to increase the harmonic flux and thereby realize experiments in xuv spectroscopy and attosecond domains.

ACKNOWLEDGMENTS

Funding for the present work was provided by the Natural Science and Engineering Research Council. The authors thank Daniel Comtois of l'Institut National de la Recherche Scientifique (INRS) for assistance during experiments conducted at Advanced Laser Light Source. The authors would also like to thank David Villeneuve and Paul Corkum at the National Research Council Canada for fruitful discussions and for allowing us to conduct preliminary experiments at their facility. J.-P.B. would like to thank Jessica Brichta and Renée Gibbins for assistance in the preparation of this paper.

---

[1] A. McPherson, G. Gibson, H. Jara, U. Johann, T. S. Luk, I. McIntyre, K. Boyer, and C. K. Rhodes, J. Opt. Soc. Am. B **4**, 595 (1987).

[2] J. J. Macklin, J. D. Kmetec, and C. L. Gordon III, Phys. Rev. Lett. **70**, 766 (1993).

[3] P. B. Corkum, Phys. Rev. Lett. **71**, 1994 (1993).

[4] M. Lewenstein, Ph. Balcou, M. Y. Ivanov, A. L'Huillier, and P. B. Corkum, Phys. Rev. A **49**, 2117 (1994).

[5] N. A. Papadogiannis, L. A. A. Nikolopoulos, D. Charalambidis, G. D. Tsakiris, P. Tzallas, and K. Witte, Phys. Rev. Lett. **90**, 133902 (2003).

[6] M. Hentschel, R. Keinberger, Ch. Spielmann, G. A. Reider, N. Milosevic, T. Brabec, P. B. Corkum, U. Heinzmann, M. Drescher, and F. Krausz, Nature (London) **414**, 509 (2001).

[7] J. Itatani, J. Levesque, D. Zeidler, H. Niikura, H. Pepin, J. C. Kieffer, P. B. Corkum, and D. M. Villeneuve, Nature (London) **432**, 867 (2004).

[8] R. Ganeev, M. Suzuki, M. Baba, H. Kuroka, and T. Ozaki, Opt. Lett. **30**, 768 (2005).

[9] E. Takahashi, Y. Nabekawa, T. Otsuka, M. Obara, and K. Midorikawa, Phys. Rev. A **66**, 021802(R) (2002).

[10] J.-F. Hergott, M. Kovačev, H. Merdji, C. Hubert, Y. Mairesse, E. Jean, P. Breger, P. Agostini, B. Carré, and P. Salières, Phys. Rev. A **66**, 021801(R) (2002).

[11] E. Takahashi, Y. Nabekawa, and K. Midorikawa, Appl. Phys. Lett. **84**, 4 (2004).

[12] P. Salières, A. L'Huillier, and M. Lewenstein, Phys. Rev. Lett. **74**, 3776 (1995).

[13] E. Constant, D. Garzella, P. Breger, E. Mével, Ch. Dorrer, C. LeBlanc, F. Salin, and P. Agostini, Phys. Rev. Lett. **82**, 1668 (1999).

[14] Y. Tamaki, J. Itatani, Y. Nagata, M. Obara, and K. Midorikawa, Phys. Rev. Lett. **82**, 1422 (1999).

[15] J. R. Sutherland, E. L. Christensen, N. D. Powers, S. E. Rhynard, J. C. Painter, and J. Peatross, Opt. Express **12**, 4430 (2004).

[16] E. A. Gibson *et al.*, Science **302**, 95 (2003).

[17] R. Bartels, S. Backus, E. Zeek, L. Misoguti, G. Vdovin, I. P. Christov, M. M. Murnane, and H. C. Kapteyn, Nature (London) **406**, 164 (2000).

[18] T. Pfeifer, R. Kemmer, R. Spitzenpfeil, D. Walter, C. Winterfeldt, G. Gerber, and Ch. Spielmann, Opt. Lett. **30**, 1497 (2005).

[19] I. J. Kim, C. M. Kim, H. T. Kim, G. H. Lee, Y. S. Lee, J. Y. Park, D. J. Cho, and C. H. Nam, Phys. Rev. Lett. **94**, 243901 (2005).

[20] H. W. Liepmann and A. Roshko, *Elements of Gasdynamics* (Wiley, New York, 1957).

[21] D. H. Levy, Annu. Rev. Phys. Chem. **31**, 197 (1980).

[22] L. A. Lompré, M. Ferray, A. L'Huillier, X. F. Li, and G. Mainfray, J. Appl. Phys. **63**, 1791 (1988).

[23] S. M. Hankin, D. M. Villeneuve, P. B. Corkum, and D. M. Rayner, Phys. Rev. Lett. **84**, 5082 (2000).

[24] M. Nisoli, G. Sansone, S. Stagira, C. Vozzi, S. De Silvestri, and O. Svelto, Appl. Phys. B: Lasers Opt. **75**, 601 (2002).

[25] J. W. Gallagher, C. E. Brion, J. A. R. Samson, and P. W. Langhoff, J. Phys. Chem. Ref. Data **17**, 9 (1988).

[26] J. W. Cooper, Phys. Rev. **128**, 681 (1962).

[27] B. K. McFarland, J. P. Farrell, M. Guhr, and P. H. Bucksbaum, Lasers and Electro-Optics, 2008 and 2008 Conference on Quantum Electronics and Laser Science (CLEO/QELS 2008), 2008 (unpublished), pp. 1–2.

[28] M. J. Weber, *Handbook of Optical Materials* (CRC, Cleveland, 2002).

[29] G. Liggett and J. S. Levinger, J. Opt. Soc. Am. **58**, 109 (1968).

[30] H. J. Lehmeier, W. Leupacher, and A. Penzkofer, Opt. Commun. **56**, 67 (1985).

[31] M. V. Ammosov, N. B. Delone, and V. P. Krainov, Sov. Phys. JETP **64**, 1191 (1986).

[32] J. Seres, V. S. Yakovlev, E. Seres, Ch. Streli, P. Wobrauschek, Ch. Spielmann, and F. Krausz, Nat. Phys. **3**, 878 (2007).

Chapter 3

Investigating signatures of electronic structure

3.1 High Harmonic Spectroscopy of the Cooper Minimum in Molecules (Publication 5)

M. C. H. Wong, A.-T. Le, A. F. Alharbi, A. E. Boguslavskiy, R. R. Lucchese, J.-P. Brichta, C. D. Lin, and V. R. Bhardwaj
High Harmonic Spectroscopy of the Cooper Minimum in Molecules
Physical Review Letters **110**, 033006 (2013)

3.1.1 Author contribution

M. C. H. Wong and J.-P. Brichta performed the experiments at ALLS in Varennes, QC. A.-T. Le performed the photoionization cross-section computer simulations. A. F. Alharbi generated the Mulliken atomic populations for the molecules studied. M. C. H. Wong conducted the analysis of the experimental results and wrote the first draft of the manuscript. All authors contributed to the final manuscript.

High Harmonic Spectroscopy of the Cooper Minimum in Molecules

M. C. H. Wong,[1] A.-T. Le,[2] A. F. Alharbi,[1] A. E. Boguslavskiy,[1] R. R. Lucchese,[3] J.-P. Brichta,[1]
C. D. Lin,[2] and V. R. Bhardwaj[1,*]

[1]*Department of Physics, University of Ottawa, 150 Louis-Pasteur, Ottawa, Ontario K1N 6N5, Canada*
[2]*J. R. Macdonald Laboratory, Kansas State University, Manhattan, Kansas 66506-2604, USA*
[3]*Department of Chemistry, Texas A&M University, College Station, Texas 77843-3255, USA*

(Received 8 June 2012; published 18 January 2013)

The Cooper minimum (CM) has been studied using high harmonic generation solely in atoms. Here, we present detailed experimental and theoretical studies on the CM in molecules probed by high harmonic generation using a range of near-infrared light pulses from $\lambda = 1.3$ to 1.8 μm. We demonstrate the CM to occur in CS_2 and CCl_4 at ~42 and ~40 eV, respectively, by comparing the high harmonic spectra with the known partial photoionization cross sections of different molecular orbitals, confirmed by theoretical calculations of harmonic spectra. We use CM to probe electron localization in Cl-containing molecules (CCl_4, CH_2Cl_2, and *trans*-$C_2H_2Cl_2$) and show that the position of the minimum is influenced by the molecular environment.

DOI: 10.1103/PhysRevLett.110.033006 PACS numbers: 33.20.Lg, 42.65.Ky

The electronic structure of atoms and molecules is mainly studied using photoelectron spectroscopy. Photoionization cross sections (PICS) and angular distribution parameters, determined as a function of photon energy, enable us to probe the nature of atomic and molecular orbitals. In atoms, if an orbital has a radial node, the dipole matrix element describing the transition from initial ground state to final continuum state can change sign as a function of photon energy. The PICS undergoes a Cooper minimum (CM) at the photon energy coinciding with the sign change [1]. An analogous effect was also observed in the photoionization of molecules containing atoms that are known to exhibit a CM [2].

High harmonic generation (HHG), in which an electron removed by the incident laser field gains energy from the field and recombines with the parent ion emitting high-energy photons [3], can also be used to probe the structure and dynamics of the recombining system that is encoded in the emitted harmonic spectrum. HHG is a new spectroscopic probe with the potential for angstrom spatial and attosecond temporal resolution, set by the shortest de Broglie wavelength of the recolliding electron and by the subcycle recollision dynamics, respectively. It has been used to image molecular orbitals [4], electronic wave packets [5], and nuclear dynamics [6] in simple aligned molecules as well as to probe collective multielectron dynamics [7] in atoms.

The recombination matrix element in the HHG process is, in essence, the inverse of photoionization, and the CM results in an amplitude modulation of the harmonic spectrum that is independent of both laser wavelength and intensity. To date, high harmonic spectroscopy has only been used to study CMs associated with the electronic structure of noble gases such as Ar [8,9] and Kr [7]. Several recent experimental and numerical studies [10–12] have focused on the origin of a shift in the position of the CM between photoionization and HHG emission. Whereas high harmonic spectroscopy has been successful in probing atomic and some simple molecular systems, extending this tool to polyatomic molecules has been difficult due to the complex nature of molecular orbitals and multielectron dynamics, thus restricting its viability as a general spectroscopic tool. Since multicenter [13] and multiorbital interferences [14] can also modulate the harmonic spectrum along with the CM, disentangling these effects is challenging in molecules.

In this Letter, we show that HHG in randomly oriented molecules containing S and Cl atoms exhibits a CM. We present the first observation of a CM in the harmonic spectrum of CS_2 and show that it agrees very well with experimental PICS. Theoretical calculations of PICS and harmonic spectra in CS_2 confirm our results. To understand how the atomic nature of a particular molecular orbital influences the photoionization dynamics, we generated high harmonics in CCl_4, CH_2Cl_2, and *trans*-$C_2H_2Cl_2$. In these molecules, the CM was monitored over a range of wavelengths and intensities that allowed its identification.

High harmonics were produced in a finite gas cell of length 10 mm with 0.6 mm apertures. A 30 cm achromatic lens was used to focus 1.3–1.8 μm near-infrared (NIR) light pulses into the gas cell through a 2 mm thick calcium fluoride window. An optical parametric amplifier pumped by a Ti:sapphire regenerative amplifier (3.5 mJ, 40 fs, 100 Hz, 0.8 μm) produced 80 fs NIR pulses whose energies varied from 0.9 mJ at 1.8 μm to 1.3 mJ at 1.3 μm. The harmonics were dispersed by a flat-field concave grating at grazing incidence onto a microchannel plate detector coupled to a phosphor screen and then imaged by a charge-coupled device camera. The spectrometer was calibrated by measuring the transmitted spectrum after an aluminum filter. Intensity calibration of the laser beam was achieved by monitoring the cutoff harmonics from HHG in Ar and validated by measuring its saturation intensity using a fast ionization gauge. The position of the laser focus in the gas cell was adjusted such that the highest yield of cutoff harmonics was produced, thereby favoring short trajectories. The vapor pressures of all liquids at room temperature were high enough for them to be introduced into the gas cell without need for a carrier gas. Each liquid underwent a freeze and thaw cycle to minimize contamination in the gas cell.

Since most molecules have ionization potentials (IP) in the range of 9–11 eV, longer wavelengths ($\lambda = 1.3$–$1.8\ \mu$m) (a) ensure adiabatic ionization, (b) extend the cutoff harmonics to beyond 50 eV which is needed to capture signatures of molecular and multielectron dynamics [15], and (c) favor phase matching at higher gas pressures, thereby partially offsetting the wavelength scaling of high harmonic signal [16].

Though CM is an atomic phenomenon, it persists in molecules containing atoms whose orbitals exhibit a radial node. We present experimental and theoretical studies on the CM in CS_2 (IP = 10.07 eV) and CCl_4 (IP = 11.47 eV) using high harmonic spectroscopy and extend it to other Cl-containing complex molecules. The top panels of Fig. 1 show experimental high harmonic spectra of CS_2 [Fig. 1(a)] and CCl_4 [Fig. 1(b)] obtained with 1.8 μm light at an intensity of $\sim 9 \times 10^{13}\ \mathrm{W/cm^2}$. For comparison, we also show the published PICS for lone-pair orbitals of CS_2 ($2\pi_g$) [17] and CCl_4 ($2t_1$) [2] obtained by angle-resolved photoelectron spectroscopy. Since lone-pair orbitals can be associated with a particular nucleus or atom, the observed minimum in the experimental PICS of these orbitals is analogous to photoionization of the $3p$ orbital of S and Cl atoms, which are known to exhibit CM at ~42 [18] and ~43.5 eV [19], respectively.

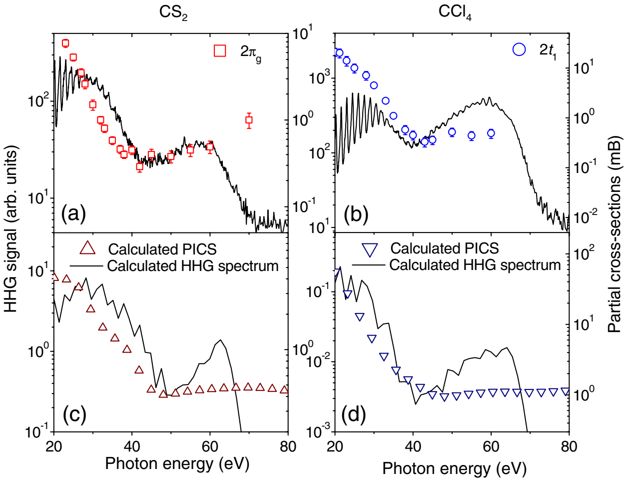

FIG. 1 (color online). Top (bottom) panels are experimental (theoretical) HHG spectra using $\lambda = 1.8\ \mu$m wavelength light with intensity $\sim 9 \times 10^{13}\ \mathrm{W/cm^2}$ ($\sim 6 \times 10^{13}\ \mathrm{W/cm^2}$) along with experimental and theoretical (open symbols) partial PICS for (a) CS_2 and (b) CCl_4. Only the envelopes are shown in theoretical HHG spectra.

The observed local minimum in the harmonic spectrum of CS_2 at ~42 eV [Fig. 1(a)] coincides well with the minimum in the PICS. The relative harmonic amplitudes are in good agreement with the known PICS in the energy range of ~30–60 eV. They differ at high energies due to a sudden drop in the harmonic signal in the cutoff region and at low energies due to poor phase matching as well as reabsorption of generated harmonics, which is typical for a gas cell. Similarly, the $2t_1$ orbital of CCl_4 also displays a minimum near ~43 eV [2], which is in fairly good agreement with the harmonic spectrum where the minimum is at ~40 eV [Fig. 1(b)].

The bottom panels of Fig. 1 show theoretical PICS as well as calculated high harmonic spectra for both CS_2 [Fig. 1(c)] and CCl_4 [Fig. 1(d)] obtained using 1.8 μm light at an intensity of $\sim 6 \times 10^{13}\ \mathrm{W/cm^2}$. Calculations for cross sections were obtained using EPOLYSCAT [20,21]. Theoretical high harmonic spectra for these molecules were obtained within a single-molecule response approximation using the quantitative rescattering (QRS) theory [22] with the transition dipole calculated from EPOLYSCAT and the ionization rate calculated within the strong-field approximation.

Local minima appear in both calculated PICS and high harmonic spectra for both molecules. In CS_2, this minimum appears at ~49 eV, which is 7 eV higher than the observed position of the minimum from experiment. The discrepancy in the position of the minimum in the high harmonic spectra can be attributed to the differences between the theoretical and experimental PICS. To avoid confusion, we note that these PICS are averaged over the isotropic molecular distribution, whereas according to the QRS, the complex valued transition dipole for a fixed-in-space molecule is used for HHG simulation. The angular averaging is carried out coherently after the induced dipole is obtained. Therefore, the position of the CM in angular-averaged PICS and that of the corresponding high harmonic spectrum could be somewhat different. In this respect, it should be of great interest to measure the CM position in HHG spectra with aligned molecules. In CCl_4, the minimum in both experimental and calculated harmonic spectra appears at ~40 eV. However, the minimum in theoretical PICS is shifted to higher photon energy (~ 48 eV) compared to that of experiments. Despite these differences, the calculations confirm the existence of a CM in molecules and fairly reproduce the relative shape of the harmonic spectra. We expect that macroscopic propagation and ground state depletion reduce the theoretical harmonic yield near the cutoff, thus bringing it to a better agreement with experiment.

The degree of atomic character in molecular orbitals influences the position of the CM, which can vary for either (a) different orbitals of a given molecule or (b) different molecular environments. Thus, the CM can be used to probe the atomic nature of molecular orbitals. To enable this, it is imperative to clearly identify the position of the CM in high harmonic spectra. However, recent studies have shown that even in simple systems such as in Ar discrepancies in the position of CM exist between different measurements and between theory and experiment.

HHG experiments carried out at 0.8, 1.2, and 2 μm have determined the CM in Ar to lie between 50 and 54 eV [8,11,12] whereas single photon measurements [23] and theoretical calculations [24] of PICS indicate the CM to occur at ~48 eV. According to the QRS theory, the CM in HHG is directly related to the CM in the differential PICS, which is slightly shifted with respect to the CM at 48 eV in the total (integrated) PICS. Moreover, the position of the CM in the HHG spectrum is influenced by the shape of the returning electron wave packet, which depends on the laser parameters and phase matching conditions. Indeed, the CM was shown to critically depend on phase matching conditions [10,12]. To understand this better, we extend the study of the CM in Ar by using a range of NIR driving wavelengths and intensities to generate high harmonics.

Figure 2 shows the measured position of the minimum in Ar using $\lambda = 1.3$–1.8 μm light as a function of intensity. The position of the minimum was extracted from each harmonic spectrum after smoothing. The use of long wavelengths reduces measurement uncertainty in determining the position of amplitude modulations since the harmonic comb spacing reduces with increasing wavelength. The error bar associated with each data point is equivalent to the energy of one harmonic order on either side of the minimum. Since phase matching was shown to be critical [10], we studied the position of the minimum for each wavelength at different pressures in the gas cell.

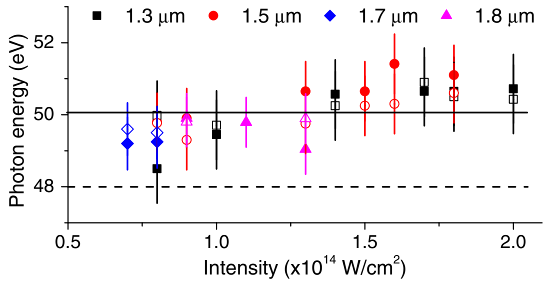

FIG. 2 (color online). Position of the Cooper minimum in HHG spectra for Ar as a function of intensity for different wavelengths $\lambda = 1.3$–1.8 μm. At each wavelength, we show the position for two different pressures (closed shapes, 45 Torr; open shapes, 25 Torr) in the finite gas cell. The dotted line at 48 eV corresponds to the position of the minimum in the experimental and theoretical PICS [23,24].

Our measurements show the position of the CM to be 50.1 ± 0.7 eV, independent of intensity, wavelength, and pressure in the gas cell (see Fig. 2). We observe a slight downshift of the minimum (49.4 eV) at lower intensities. This could be because at low intensities, the cutoff moves closer to the CM, thus influencing its position. This value for the position of the CM is in good agreement with theoretical simulations based on the QRS theory at the single-atom level [22] and with the inclusion of macroscopic propagation [11], where a single active-electron model potential suggested by Muller [25] was used. Calculation of the recombination transition dipole using field-free continuum wave functions within the same model potential approach also predicts the CM to occur near 51 eV [8,12,22].

We now return to the discussion on CM in molecules. The position of the CM might differ for different orbitals of a given molecule. In fact, calculations of PICS for the 2π and 5σ bands in HCl [26] indicate a variation of the CM position by a few eV. However, this would be difficult to study using high harmonic spectroscopy due to the lack of selectivity of a specific orbital. Here, we study the case where the CM can be affected by the molecular environment and therefore can vary for different molecules even when their molecular orbitals originate from the same atomic subshell (for example, the 3π orbital of Cl).

Figure 3(a) shows the harmonic spectra of three Cl-containing molecules using $\lambda = 1.8$ μm light with intensity $\sim 9 \times 10^{13}$ W/cm^2. Each harmonic spectrum exhibits a deep local minimum at 40.4 ± 0.5 eV (CCl_4, IP = 11.47 eV), 42.1 ± 0.4 eV (CH_2Cl_2, IP = 11.32 eV), and 43.2 ± 0.4 eV (*trans*-$C_2H_2Cl_2$, IP = 9.64 eV). The dashed line indicates the noted shift of the minimum between different molecules. We performed a systematic study to accurately determine the position of the minimum and whether it is influenced by the experimental conditions. Figures 3(b)–3(d) show the intensity dependence of the minimum in all molecules for different wavelengths whereas Fig. 3(e) shows the pressure dependence using $\lambda = 1.8$ μm light for CCl_4 and CH_2Cl_2. The dotted lines indicate the average value of the position of the minimum for each molecule. The positions of the minima and the error bars were derived in the same fashion as that for Fig. 2.

The positions of the amplitude minima in the harmonic spectra for all three molecules are independent of laser intensity and gas pressure, which suggests that they arise due to CM. This interpretation is also confirmed from the theoretical calculations. Minima arising through dynamical interference from multiorbital contributions to ionization [14] depend strongly on the laser parameters (intensity and wavelength) and can therefore be excluded. In addition, any minima arising from structural interference due to multicenter recombination [13,27,28] in unaligned molecules are expected to be very weak. A local minimum is

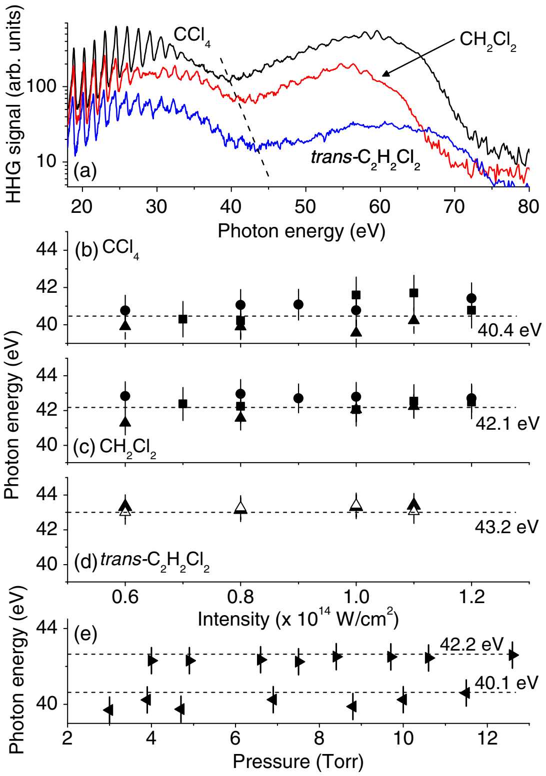

FIG. 3 (color online). (a) Harmonic spectra generated in CCl_4, CH_2Cl_2, and *trans*-$C_2H_2Cl_2$ using $\lambda = 1.8\ \mu m$ and intensity $\sim 9 \times 10^{13}\ W/cm^2$. The dashed line emphasizes the shift of the minimum between different molecules. [(b)–(d)] Position of minimum in harmonic spectra as a function of intensity for (b) CCl_4 and (c) CH_2Cl_2 with $P = 10$ Torr and $\lambda = 1.3\ \mu m$ (filled squares), $1.5\ \mu m$ (filled circles), $1.8\ \mu m$ (filled triangles) as well as (d) *trans*-$C_2H_2Cl_2$ where $\lambda = 1.8\ \mu m$ and $P = 10$ Torr (filled triangles), 3 Torr (hollow triangles). (e) Position of minimum as a function of pressure for CCl_4 (left hand side filled triangles) and CH_2Cl_2 (right hand side filled triangles) using $\lambda = 1.8\ \mu m$ light with intensity $\sim 9 \times 10^{13}\ W/cm^2$.

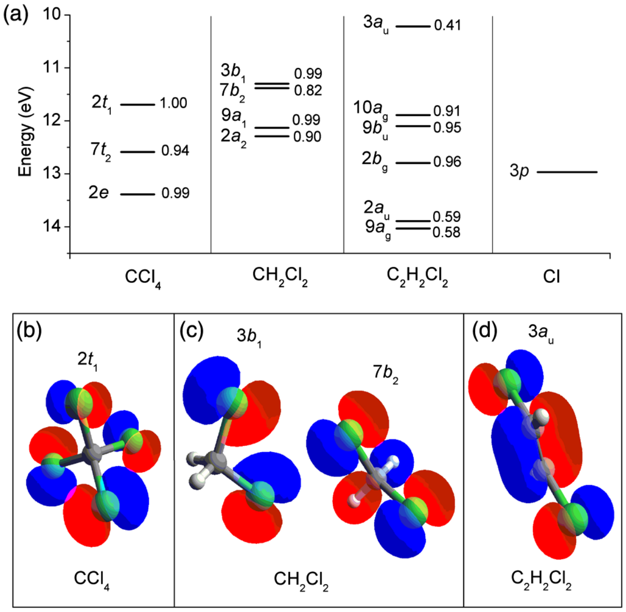

FIG. 4 (color online). (a) Binding energies and corresponding Mulliken atomic populations on Cl for molecular orbitals of CCl_4, CH_2Cl_2, and *trans*-$C_2H_2Cl_2$ as well as atomic Cl [2,33,34]. [(b)–(d)] Highest occupied molecular orbitals of (b) CCl_4, (c) CH_2Cl_2, and (d) *trans*-$C_2H_2Cl_2$.

reported to be present in PICS measurements for at least one orbital in CH_2Cl_2, but the position has not been published [29]. To our knowledge, PICS for *trans*-$C_2H_2Cl_2$ are not available for a direct comparison of the position of the CM, but the intensity-independent minimum in the harmonic spectrum is strong evidence that a CM must be present in the PICS.

The variation of CM in the three molecules is then a measure of the extent to which molecular orbitals retain part of their atomic character. To quantify the degree to which the $3p$ subshell of Cl exerts its influence on the molecular orbitals, we compare Mulliken atomic populations on Cl for each molecule. We performed *ab initio* calculations of the molecular orbitals at Hartree-Fock level using GAMESS [30]. In Fig. 4(a), we show the binding energies as well as the Mulliken atomic populations on Cl for all low-lying molecular orbitals of the three molecules in addition to the $3p$ subshell of Cl. All molecular orbitals within the 11–14 eV range have lone-pair character and, consequently, have high Mulliken atomic populations on Cl. However, the highest occupied molecular orbital (HOMO) of *trans*-$C_2H_2Cl_2$ has bonding character from the C-Cl bond with some contribution from the $3p$ orbital of Cl [31]. Such bonding orbitals are also known to exhibit a minimum in their PICS known as a partial CM (for example, the $6a_1$ band in CCl_4 [2]).

The Mulliken atomic populations on Cl are 1.0, 0.9 [32], and 0.4 for the HOMOs of CCl_4, CH_2Cl_2, and *trans*-$C_2H_2Cl_2$, respectively. Thus, the influence of the $3p$ subshell of Cl is more significant in CCl_4 and less so in *trans*-$C_2H_2Cl_2$. This is apparent from the molecular orbitals shown in Fig. 4(b) and consistent with results from photoelectron spectroscopy where the visibility of the CM, represented by the depth in the angular distribution parameter, decreased as Cl atoms were replaced by H atoms in CCl_4 [29].

In conclusion, we demonstrate for the first time evidence of a CM in high harmonic spectra of unaligned polyatomic molecules. Experimentally, we show that CM can be a sensitive probe of the atomic nature of the molecular orbital since it is independent of laser parameters. From a theoretical point of view, CM can be used to test the validity of new tools that are being developed so that they can be extended to even complex molecules. The agreement between the experimental and theoretical HHG spectra suggests that in aligned molecules it is possible to extract shapes of PICS for the HOMOs of molecules over a ~30–60 eV range using high harmonic spectroscopy, similar to the atomic case [7,9]. However, phase matching and dynamical interference from multi-orbital contributions to HHG would restrict extraction of cross sections over a large photon energy spectrum.

The authors gratefully acknowledge financial support from the Natural Science and Engineering Research Council of Canada, expert technical assistance from Bruno Schmidt and Antoine Laramée, and fruitful discussions with François Légaré and Thomas Brabec. A.-T. L., R. R. L., and C. D. L. are supported by the Chemical Sciences, Geosciences and Biosciences Division, Office of Basic Energy Sciences, Office of Science, U.S. Department of Energy.

---

*ravi.bhardwaj@uottawa.ca

[1] J. W. Cooper, Phys. Rev. **128**, 681 (1962).
[2] T. A. Carlson, M. O. Krause, F. A. Grimm, P. Keller, and J. W. Taylor, J. Chem. Phys. **77**, 5340 (1982).
[3] P. B. Corkum, Phys. Rev. Lett. **71**, 1994 (1993).
[4] J. Itatani, J. Levesque, D. Zeidler, H. Niikura, H. Pépin, J. C. Kieffer, P. B. Corkum, and D. M. Villeneuve, Nature (London) **432**, 867 (2004).
[5] S. Haessler *et al.*, Nat. Phys. **6**, 200 (2010).
[6] S. Baker, J. S. Robinson, C. A. Haworth, H. Teng, R. A. Smith, C. C. Chirilă, M. Lein, J. W. G. Tisch, and J. P. Marangos, Science **312**, 424 (2006).
[7] A. D. Shiner, B. E. Schmidt, C. Trallero-Herrero, H. J. Wörner, S. Patchkovskii, P. B. Corkum, J.-C. Kieffer, F. Légaré, and D. M. Villeneuve, Nat. Phys. **7**, 464 (2011).
[8] H. J. Wörner, H. Niikura, J. B. Bertrand, P. B. Corkum, and D. M. Villeneuve, Phys. Rev. Lett. **102**, 103901 (2009).
[9] S. Minemoto, T. Umegaki, Y. Oguchi, T. Morishita, A.-T. Le, S. Watanabe, and H. Sakai, Phys. Rev. A **78**, 061402 (R) (2008).
[10] J. P. Farrell, L. S. Spector, B. K. McFarland, P. H. Bucksbaum, M. Gühr, M. B. Gaarde, and K. J. Schafer, Phys. Rev. A **83**, 023420 (2011).
[11] C. Jin, H. J. Wörner, V. Tosa, A.-T. Le, J. B. Bertrand, R. R. Lucchese, P. B. Corkum, D. M. Villeneuve, and C. D. Lin, J. Phys. B **44**, 095601 (2011).
[12] J. Higuet *et al.*, Phys. Rev. A **83**, 053401 (2011).
[13] M. Lein, N. Hay, R. Velotta, J. P. Marangos, and P. L. Knight, Phys. Rev. A **66**, 023805 (2002).
[14] O. Smirnova, Y. Mairesse, S. Patchkovskii, N. Dudovich, D. Villeneuve, P. Corkum, and M. Y. Ivanov, Nature (London) **460**, 972 (2009).
[15] R. Torres *et al.*, Opt. Express **18**, 3174 (2010).
[16] A. D. Shiner, C. Trallero-Herrero, N. Kajumba, H.-C. Bandulet, D. Comtois, F. Légaré, M. Giguère, J.-C. Kieffer, P. B. Corkum, and D. M. Villeneuve, Phys. Rev. Lett. **103**, 073902 (2009).
[17] T. A. Carlson, M. O. Krause, and F. A. Grimm, J. Chem. Phys. **77**, 1701 (1982).
[18] S. T. Manson, A. Msezane, A. F. Starace, and S. Shahabi, Phys. Rev. A **20**, 1005 (1979).
[19] J. A. R. Samson, Y. Shefer, and G. C. Angel, Phys. Rev. Lett. **56**, 2020 (1986).
[20] F. A. Gianturco, R. R. Lucchese, and N. Sanna, J. Chem. Phys. **100**, 6464 (1994).
[21] A. P. P. Natalense and R. R. Lucchese, J. Chem. Phys. **111**, 5344 (1999).
[22] A.-T. Le, R. R. Lucchese, S. Tonzani, T. Morishita, and C. D. Lin, Phys. Rev. A **80**, 013401 (2009).
[23] J. A. R. Samson and W. C. Stolte, J. Electron Spectrosc. Relat. Phenom. **123**, 265 (2002).
[24] W. Ong and S. T. Manson, Phys. Rev. A **21**, 842 (1980).
[25] H. G. Muller, Phys. Rev. A **60**, 1341 (1999).
[26] T. A. Carlson, M. O. Krause, A. Fahlman, P. R. Keller, J. W. Taylor, T. Whitley, and F. A. Grimm, J. Chem. Phys. **79**, 2157 (1983).
[27] T. Kanai, S. Minemoto, and H. Sakai, Nature (London) **435**, 470 (2005).
[28] M. C. H. Wong, J.-P. Brichta, and V. R. Bhardwaj, Phys. Rev. A **81**, 061402(R) (2010).
[29] T. A. Carlson, M. O. Krause, W. A. Svensson, P. Gerard, F. A. Grimm, T. A. Whitley, and B. P. Pullen, Z. Phys. D **2**, 309 (1986).
[30] M. W. Schmidt *et al.*, J. Comput. Chem. **14**, 1347 (1993).
[31] L. Mei, M. Chuaqui, C. P. Mathers, J. F. Ying, and K. T. Leung, Chem. Phys. **188**, 347 (1994).
[32] Average over close-lying HOMO ($3b_1$) and HOMO-1 ($7b_2$).
[33] T. Pradeep and D. A. Shirley, J. Electron Spectrosc. Relat. Phenom. **66**, 125 (1993).
[34] M. A. Parkes, S. Ali, C. R. Howle, R. P. Tuckett, and A. E. R. Malins, Mol. Phys. **105**, 907 (2007).

Chapter 4

The influence of molecular structure

4.1 Signatures of symmetry and electronic structure in high-order harmonic generation in polyatomic molecules (Publication 3)

M. C. H. Wong, J. -P. Brichta, and V. R. Bhardwaj
Signatures of symmetry and electronic structure in high-order harmonic generation in polyatomic molecules
Physical Review A **81**, 061402(R) (2010)

4.1.1 Author contribution

M. C. H. Wong and J.-P. Brichta performed the experiments at ALLS in Varennes, QC. J.-P. Brichta performed the three-center interference calculation. M. C. H. Wong conducted the analysis of the experimental results and wrote the first draft of the manuscript. All authors contributed to the final manuscript.

PHYSICAL REVIEW A **81**, 061402(R) (2010)

Signatures of symmetry and electronic structure in high-order harmonic generation in polyatomic molecules

M. C. H. Wong, J.-P. Brichta, and V. R. Bhardwaj[*]
Department of Physics, University of Ottawa, 150 Louis Pasteur, Ottawa, Ontario, K1N 6N5 Canada

(Received 8 March 2010; published 10 June 2010)

We report detailed measurements of high-order harmonic generation in chloromethane molecules (CCl_4, $CHCl_3$, and CH_2Cl_2) to show that fingerprints of symmetry and electronic structure can be decoded from high-order harmonic generation even in complex randomly oriented molecules. In our measurements, orbital symmetries of these molecules are manifested as both extended harmonic cutoffs and a local minimum in the ellipticity dependence of the cut-off harmonics, suggesting the occurrence of quantum interferences during ionization. The harmonic spectra exhibit distinct interference minima at ~42 and ~60 eV. We attribute the former to the Cooper minimum in the photoionization cross section and the latter to intramolecular interference during the recombination process.

DOI: 10.1103/PhysRevA.81.061402 PACS number(s): 33.20.Xx, 42.65.Ky, 33.20.Lg

High-order harmonic generation (HHG) is a key process in attosecond science. Originally, the focus has been on HHG in atoms as it allows production of attosecond light pulses [1]. However, HHG in molecules is fast becoming a topic of interest in strong-field physics. The amplitude and phase of the high-order harmonics generated in a molecule can be used as a sensitive tool to probe electronic structure [2] and nuclear dynamics [3] with Ångström spatial and attosecond temporal precision.

Three distinct steps are involved in the HHG process [4], each of which imprints their signatures on the harmonic spectrum. In the first step, an electron wave packet is launched from the highest occupied molecular orbital (HOMO) into the continuum by tunneling, thereby transferring orbital information. In the second step, the electron wave packet propagates in the continuum and returns to the molecular ion, accumulating a quantum mechanical phase proportional to the excursion time. If the electron wave packet originates from multiple orbitals, the phase difference between multiple quantum paths leads to interferences that modulate the harmonic spectrum and phase [5,6]. In the third step, the electron wave packet recombines with the parent ion, emitting a high-energy photon. The recombination process, described by the dipole matrix element between the continuum state of the returning electron and the bound state of the recombined electron, can lead to modulation of amplitude and phase due to interference between the dipole amplitudes from the multiatomic centers in the molecule when they are separated by half a de Broglie wavelength [7].

To date, deciphering electronic and molecular structure information from HHG, both experimentally and theoretically, has been possible only in simple molecules like O_2, N_2, and CO_2 that are aligned in the laser field [8,9]. Very little is known about polyatomic molecules in which the orbital symmetries can be complex with multiple nodal planes, and multielectron dynamics can become significant with several orbitals close to the HOMO. The latter was found to play a major role, even in a relatively simple molecule like CO_2 [9].

In this Rapid Communication, we show that signatures of orbital symmetry and electronic structure can still be observed in the high-order harmonic spectra of randomly oriented polyatomic molecules. We demonstrate extended high-order harmonic generation in chloromethane molecules (CH_2Cl_2, $CHCl_3$, and CCl_4) and a local minimum in the ellipticity dependence of cut-off harmonics in CCl_4. We attribute this to quantum interference effects during the ionization process. We retrieve information on electronic structure from modulations in the harmonic spectra and demonstrate signatures of three-center interference during the recombination process.

Since strong field effects are greatly influenced by the ionization potential (IP), we choose CH_2Cl_2, $CHCl_3$, and CCl_4 because they have similar IPs but increasingly complex HOMO symmetries. In addition, they are highly polarizable molecules ($\alpha = {\sim}7\text{–}10$ Å^3), so multi-electron dynamics can become significant. The harmonic spectra are measured at 1300 and 1500 nm. At longer wavelengths, (a) ionization of polyatomic molecules is adiabatic [10], (b) higher-order harmonics can be easily produced as the ponderomotive energy of the electron scales as wavelength squared, (c) ellipticity dependence is stronger [11], and (d) the electron wave packet can be more accurately represented by a plane wave.

High-order harmonics are produced either in a 50-cm-long semi-infinite gas cell (SIGC) with a 150-μm pinhole or a 10-mm-long finite gas cell (FGC) with 600-μm apertures. A 75-cm (30-cm) achromatic lens is used to focus 1300-nm and 1500-nm light into the SIGC (FGC) through a 2-mm-thick calcium fluoride window. An optical parametric amplifier pumped by a Ti:sapphire regenerative amplifier (~3.5 mJ, 40 fs, 100 Hz, 800 nm) produced (1.2 mJ, 80 fs) 1300-nm and 1500-nm light. The intensity of the laser beam is altered by a combination of a half-wave plate and a thin-film polarizer. A quarter-wave plate is used to change the polarization of the driving pulse from linear to elliptical. The harmonics are dispersed by a flat field concave grating at grazing incidence onto a microchannel plate detector coupled to a phosphor screen and imaged by a CCD camera. The harmonic spectra are obtained under optimal phase-matching conditions by adjusting both the laser focus with respect to the pinhole and the pressure in the gas cell. Vapor pressure of chloromethanes at room temperature is used to introduce them into the gas

---

[*] ravi.bhardwaj@uottawa.ca

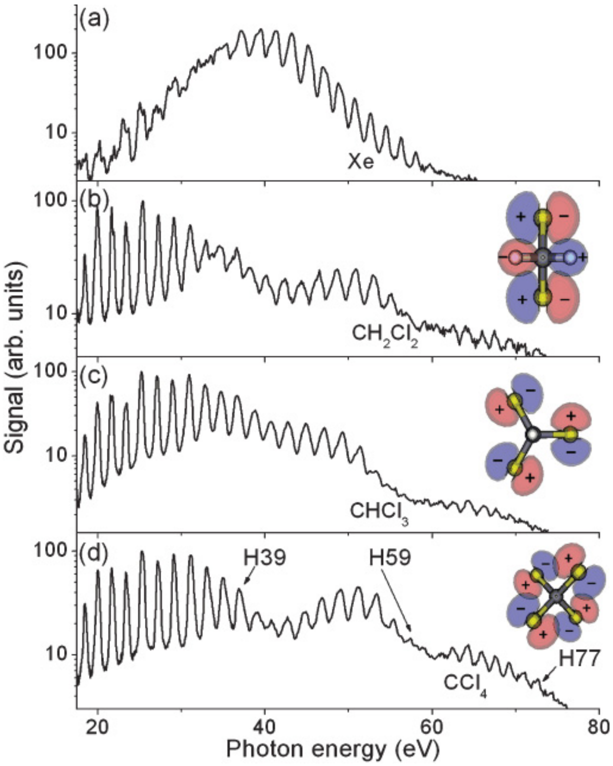

FIG. 1. (Color online) High-order harmonic spectra of (a) Xe, (b) CH_2Cl_2, (c) $CHCl_3$, and (d) CCl_4 produced by 1300-nm light at intensity of $\sim 1.5 \times 10^{14}$ W cm^{-2} in the finite gas cell. Also shown are the HOMOs for each molecule.

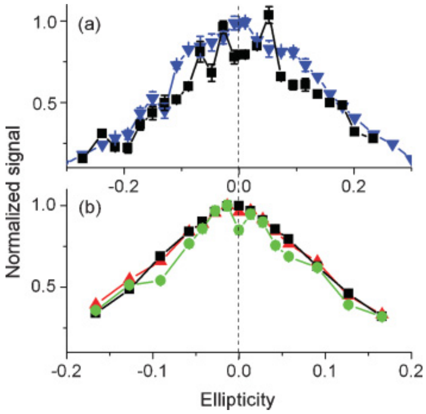

FIG. 2. (Color online) Ellipticity dependence of (a) the 21st harmonic in CCl_4 (squares) and CH_2Cl_2 (down triangles) at an intensity of $\sim 3 \times 10^{13}$ W cm^{-2}, and (b) the 29th (circles) and 39th (up triangles) harmonic in CCl_4 and the 29th in Xe (squares) at an intensity of $\sim 5 \times 10^{13}$ W cm^{-2}. Harmonics are produced in the semi-infinite gas cell using 1300-nm light.

cell without any carrier gas. A fast ionization gauge is used to calibrate the incident intensity; the methodology is described elsewhere [12].

Figure 1 compares the harmonic spectra of CH_2Cl_2 (IP 11.33 eV), $CHCl_3$ (11.37 eV), and CCl_4 (11.47 eV) with Xe (12.13 eV) at a laser intensity of $\sim 1.5 \times 10^{14}$ W cm^{-2} (1300 nm), close to the saturation intensity for both the molecules and the atom. First, the HHG cutoff in all three chloromethane molecules is extended well beyond that of Xe despite their lower IPs. Second, the harmonic cutoff in CCl_4 is extended by about 3 eV in comparison to the other molecules. Also the efficiency of cut-off harmonics increases from CH_2Cl_2 to CCl_4. Third, the harmonic amplitudes exhibit modulations. In the absence of any interference effects, as is the case with atoms, the shape of the harmonic spectra is primarily determined by both the phase-matching conditions and absorption in the gas cell. The observed modulations are independent of laser intensity.

Extension of cut-off harmonics in molecules, compared to an atom of similar IP, is a manifestation of suppressed ionization [13]. In molecules whose HOMO exhibits nodal planes, suppression of ionization occurs due to quantum interferences when electron wave packets emitted from either side of a nodal plane destructively interfere due to their opposite phases. The HOMOs, calculated using GAMESS [14,15], of all three molecules are shown as insets in Figs. 1(b)–1(d). In CH_2Cl_2, the σ plane containing Cl-C-Cl is a nodal plane. In $CHCl_3$, the three σ planes containing Cl-C-H are also nodal planes. In CCl_4, a p-type orbital is located on each chlorine atom. Of the six σ planes containing Cl-C-Cl, two of them form perfect nodal planes.

Another manifestation of suppressed ionization due to quantum interferences is the ellipticity dependence of the HHG process. Fingerprints of molecular orbitals are preserved during the propagation of the electron wave packet in the laser field and should therefore be reflected in the HHG process. Figure 2(a) shows the ellipticity variation of the laser polarization for the 21st harmonic in CCl_4 and CH_2Cl_2 at an intensity of $\sim 3 \times 10^{13}$ W cm^{-2}, below the saturation intensity. We observe a local minimum for linear polarization in CCl_4 but not in the other two chloromethanes. The local minimum is a consequence of quantum interference during ionization. In CCl_4, an electron wave packet cannot be launched if the laser polarization lies in the two nodal planes. Also, there exist certain directions in the four non-nodal σ planes where ionization is minimal. The high-order symmetry of the molecular orbital, though randomly oriented, leads to low ionization probability for linear polarization. As the ellipticity increases, the destructive interference is offset by the transverse field component that compensates for initial electron momentum, forcing some of the electrons to recombine with the ionic core. However, at larger ellipticities, the recombination probability decreases, drastically reducing the HHG signal. In contrast, CH_2Cl_2 has only one nodal plane. So in an ensemble of randomly oriented molecules, the interference effect is diminished.

In Fig. 2(b), the ellipticity dependence of the 29th and 39th harmonics of CCl_4 is compared with the 29th harmonic of Xe at an intensity of $\sim 5 \times 10^{13}$ W cm^{-2}. The dip in harmonic signal at linear polarization is more prominent only for cut-off harmonics and decreases progressively for plateau harmonics. This is the first observation of a local minimum in the ellipticity dependence of high-order harmonics in complex molecules and is similar to that observed in the recollision signal of C_6H_6 [10].

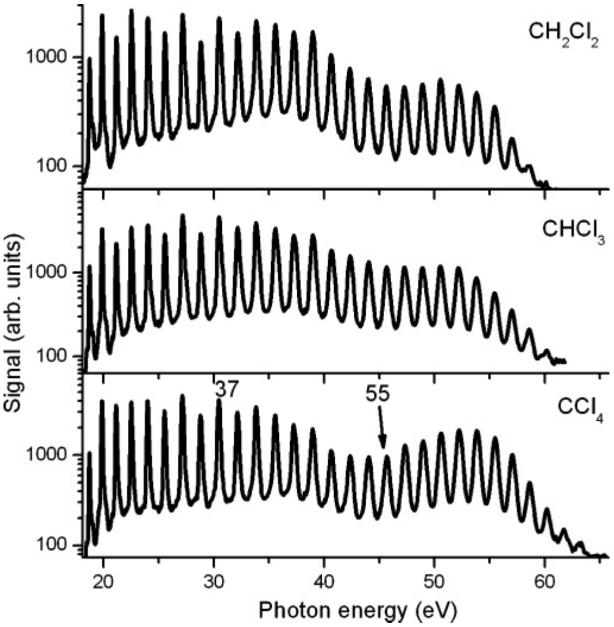

FIG. 3. High-order harmonic spectra of chloromethane molecules produced by 1500-nm light at an intensity of 8×10^{13} W cm^{-2} in the finite gas cell.

We now return to the amplitude modulations in the harmonic spectra in Fig. 1. There are amplitude minima at ~42 and ~60 eV in all three molecules. Their location is independent of laser intensity. The minimum at ~42 eV is also independent of laser wavelength, as shown in Fig. 3. The origin of the amplitude modulation in the harmonic spectra can be due to (a) the electronic structure of the molecule (its contribution is independent of the laser source), (b) intramolecular interference during recombination (depends only on the molecular structure and varies with orientation angle between the incident field and the molecular axis), and (c) interference arising from multiorbital contribution to the electron dynamics in the continuum (dependent on the laser source and the molecular species).

The amplitude minima cannot be associated with multiorbital interferences as their positions are the same for all molecules. The relative phase acquired by the electron wave packet originating from multiple orbitals depends on the product of electron excursion time (which varies with laser intensity and wavelength) and the energy difference between the orbitals (varies with molecules). For instance, in CCl_4 the first four nondegenerate molecular orbitals below the HOMO have energy differences of 0.884, 1.50, 4.95, and 8.53 eV with respect to the HOMO. In $CHCl_3$, the energy levels are more closely spaced than in CCl_4; the first four nondegenerate molecular orbitals have energy differences of 0.41, 0.48, 1.18, and 4.50 eV. The energy levels of CH_2Cl_2 are roughly similar to $CHCl_3$. The phase calculations, similar to those carried out for He and Ne [5], indicate that the first three orbitals in CH_2Cl_2 and $CHCl_3$ do not give rise to destructive interference below 80 eV. Contribution from the HOMO-4 gives rise to destructive interference within the energy range of interest but occurs at different energies in the HHG spectra in both molecules and is distinctly different from the HOMO-3 contribution from CCl_4. We could not study the wavelength dependence of the minima at ~60 eV, as the intensity was not sufficient to produce high-energy harmonics at 1500 nm.

The intensity and wavelength independence of the harmonic amplitude minimum at ~42 eV is close to the Cooper minimum in the photoionization cross sections of the chloromethane molecules [16,17]. Since the recombination process is the inverse of photoionization, we identify the amplitude minimum with electronic structure of the molecule. Similar observations have recently been made in Ar [18]. All lone pair orbitals of chloromethane molecules (first three orbitals of CCl_4 and $CHCl_3$, two orbitals of CH_2Cl_2) exhibit a minimum at ~43 eV and can be approximately visualized as arising from ionization of the constituent Cl atom. In the atomic case, a change in sign in the dipole amplitude matrix elements between the initial $3p$ orbital of Cl and the d continuum channel produces a minimum in the cross section. Therefore, to some extent, the minimum is the same for all three molecules. Beyond 43 eV, the photoionization cross section initially increases and then decreases monotonically with no further minimum [19]. Therefore, the second minimum at ~60 eV cannot be associated with the Cooper minimum.

The fixed position of the second minimum at 60 eV suggests the role of molecular structure. In simple aligned molecules, molecular structure has been shown to cause interferences in the HHG spectra during the recombination process [7]. This occurs for a specific orientation angle. We propose a similar model to describe the second amplitude minimum, which suggests that the combination of the symmetry of the molecular system and the asymmetry in the angle-dependent ionization process preferentially selects a specific orientation even in randomly oriented molecules.

We use $CHCl_3$ to model the three-center interference. We ignore the H and C atoms, since most of the electron density distribution is centered on the Cl atoms. The three Cl atoms are assumed to form a triangle, as shown in Fig. 4(a), with each p-type orbital of Cl having a nodal plane along the imaginary C-Cl bond. The Cl-Cl bond length used is 2.92 Å. We define the orientation angle, θ, to be between the electron k vector

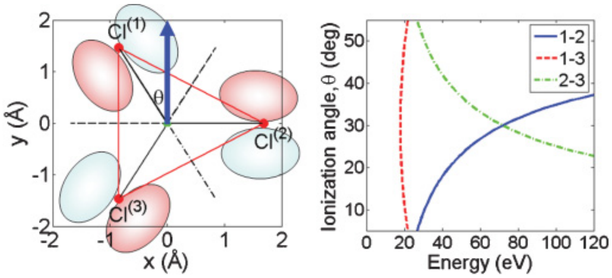

FIG. 4. (Color online) (a) Schematic of three-center interference in a hypothetical Cl_3 molecule. The three chlorine atoms are labeled. The orbital on each atom is shown with the arrow indicating ionization direction (see text for details). (b) Interference condition as a function of ionization angle. The three possible channels are labeled according to the participating pair of atoms: channel 1-2 is shown with a blue, solid line; channel 1-3 is shown with a red, dashed line; and channel 2-3 is shown with a green, dash-dotted line.

and the center of the triangle. Due to the symmetry of the system (the point groups of CH_2Cl_2, $CHCl_3$, and CCl_4 are C_{2v}, C_{3v}, and T_D respectively), we restrict the orientation angles so that $0^\circ < \theta < 60^\circ$ degrees, rationalized by the fact that an electron wave packet cannot be launched along 0° or 60° due to suppression of ionization.

The three possible two-center interferences are labeled by the participating atoms. Similar to previous studies, destructive interference between two atomic centers involving anti-symmetric orbitals is considered for which the path length is an integral multiple of the electron's de Broglie wavelength. The IP of the molecule is ignored in the de Broglie wavelength calculation. Figure 4(b) shows the photon energies at which destructive interference would occur for the three channels as a function of the ionization angle. The two channels intersect at an ionization angle of 30°. Based on the electron density distributions, this angle would also approximately correspond to maximum ionization probability which has been observed in other molecules [20].

The photon energy where the two interference channels overlap is ~70 eV. The 10-eV difference between this simplistic model prediction and the experiment could be due to molecular vibrations. High-energy photons are produced at the peak of the laser pulse, so for the 70-fs-long pulse used in the experiment, it is possible for the atoms to move. A 10-eV shift in the interference minimum corresponds to only a 10% increase in the bond lengths. Similar arguments can be made for the 60-eV interference minimum in CCl_4. However, in CH_2Cl_2, the symmetry is broken, shifting the intersection of the two channels to higher energies (~100 eV). However, faster motion of H atoms would downshift the intersection point. Quantum mechanical calculations that include the appropriate orbitals should shed more light on such interferences.

This is an experimental observation of three-center interference in HHG in a randomly oriented molecule; such interference was demonstrated theoretically in an aligned linear H_3^+ molecule [21]. Multislit interferences were also shown to occur in a spherically symmetric C_{60} molecule [22]. The possibility of extracting electronic and molecular structure information from HHG in complex molecules would widen the prospects of using HHG as a sensitive tool to probe electron dynamics in larger molecules with high spatial and temporal precision.

ACKNOWLEDGMENTS

We gratefully acknowledge discussions with Paul Corkum, Thomas Brabec, and Andreas Becker. This research is supported by the Natural Science and Engineering Research Council of Canada.

---

[1] M. Hentschel *et al.*, Nature **414**, 509 (2001).
[2] J. Itatani *et al.*, Nature **432**, 867 (2004).
[3] S. Baker *et al.*, Science **312**, 424 (2006).
[4] P. B. Corkum, Phys. Rev. Lett. **71**, 1994 (1993).
[5] T. Kanai, E. J. Takahashi, Y. Nabekawa, and K. Midorikawa, Phys. Rev. Lett. **98**, 153904 (2007).
[6] W. Li *et al.*, Science **322**, 1207 (2008).
[7] M. Lein, N. Hay, R. Velotta, J. P. Marangos, and P. L. Knight, Phys. Rev. Lett. **88**, 183903 (2002).
[8] S. M. T. Kanai and H. Sakai, Nature **435**, 470 (2005).
[9] O. Smirnova *et al.*, Nature **460**, 972 (2009).
[10] V. R. Bhardwaj, D. M. Rayner, D. M. Villeneuve, and P. B. Corkum, Phys. Rev. Lett. **87**, 253003 (2001).
[11] H. Xu *et al.*, Opt. Lett. **35**, 472 (2010).
[12] J.-P. Brichta *et al.*, Phys. Rev. A **79**, 033404 (2009).
[13] B. Shan, X. M. Tong, Z. Zhao, Z. Chang, and C. D. Lin, Phys. Rev. A **66**, 061401 (2002).
[14] M. W. Schmidt *et al.*, J. Comput. Chem. **14**, 1347 (1993).
[15] M. S. Gordon and M. W. Schmidt, in *Theory and Applications of Computational Chemistry: The First Forty Years*, edited by C. E. Dykstra, G. Frenking, K. S. Lim, and G. E. Scusaria (Elsevier Science, Amsterdam, 2005), pp. 1167–1189.
[16] T. A. Carlson *et al.*, J. Chem. Phys. **77**, 5340 (1982).
[17] T. A. Carlson *et al.*, Z. Phys. D **2**, 309 (1986).
[18] H. J. Wörner, H. Niikura, J. B. Bertrand, P. B. Corkum, and D. M. Villeneuve, Phys. Rev. Lett. **102**, 103901 (2009).
[19] G. R. Burton *et al.*, Chem. Phys. **181**, 147 (1994).
[20] D. Pavičić, K. F. Lee, D. M. Rayner, P. B. Corkum, and D. M. Villeneuve, Phys. Rev. Lett. **98**, 243001 (2007).
[21] M. Lein, P. P. Corso, J. P. Marangos, and P. L. Knight, Phys. Rev. A **67**, 023819 (2003).
[22] M. F. Ciappina, A. Becker, and A. Jaroń-Becker, Phys. Rev. A **78**, 063405 (2008).

4.2 High-harmonic generation in H_2O (Publication 2)

M. C. H. Wong, J. -P. Brichta, and V. R. Bhardwaj
High-harmonic generation in H_2O
Optics Letters **35** 1947–1949 (2010)

4.2.1 Author contribution

M. C. H. Wong and J.-P. Brichta performed the experiments at ALLS in Varennes, QC. J.-P. Brichta performed the divergence calculation. M. C. H. Wong conducted the analysis of the experimental results and wrote the first draft of the manuscript. All authors contributed to the final manuscript.

High-harmonic generation in H_2O

M. C. H. Wong, J. -P. Brichta, and V. R. Bhardwaj*

Department of Physics, University of Ottawa, 150 Louis Pasteur, Ottawa, Ontario, Canada
**Corresponding author: ravi.bhardwaj@uottawa.ca*

Received January 15, 2010; revised April 29, 2010; accepted April 30, 2010;
posted May 19, 2010 (Doc. ID 122740); published June 3, 2010

We demonstrate high-harmonic generation in H_2O using 800 and 1300 nm laser pulses up to a maximum intensity of 5×10^{14} W/cm^2. Under optimal phase-matching conditions, photon energies up to ~60 and ~87 eV are produced by using 800 and 1300 nm light, respectively. The harmonic spectra in H_2O, when compared with Xe with a similar ionization potential, exhibit significant extension of the cutoff region, indicating suppression of ionization arising from molecular orbital symmetry. © 2010 Optical Society of America

OCIS codes: 020.2649, 190.4160, 320.7110.

High-harmonic generation (HHG) is a key process in attosecond science. It permits generation of attosecond light pulses [1] and tomographic imaging of molecular orbitals and dynamics [2]. In atoms, the HHG process is well understood using a three-step model [3], where strong field ionization launches an electron wave packet into the continuum, which then propagates in the laser field and returns to the ionic core to undergo recombination and emit high-energy photons. The ionization step of the HHG process is often described by single-active-electron models that assume predominant contribution from only the highest occupied orbital [4]. However, in molecules, the symmetry of the highest occupied molecular orbital (HOMO) from which an electron is pushed into the continuum influences ionization and hence the HHG process. Moreover, the multielectron dynamics from multiple orbitals can play a dominant role in the HHG process [5,6]. While this feature allows a new way to selectively probe individual orbitals, it also introduces complexity in extracting orbital information in tomographic imaging.

Within this context, the study of HHG in H_2O molecules presented in this Letter will lay the foundation for future work that helps to understand the relative roles of different orbitals. We choose to study HHG in H_2O because of (1) its simple orbital symmetries. The HOMO and the next two underlying orbitals (HOMO-1 and HOMO-2) all have identical p-type orbitals with a single nodal plane. In contrast, even in a simple diatomic molecule like O_2, symmetries of different orbitals are dissimilar. (2) The HOMO, HOMO-1, and HOMO-2 are all well separated (>2 eV) [6], whereas in CO_2, for example, HOMO-1 and HOMO-2 differ in energies by only 0.5 eV. (3) The ionization potential of H_2O (12.6 eV) is comparable with that of Xe (12.13 eV), which permits better understanding of the HHG process. (4) It is a simple bent molecule that can be easily aligned by using the latest techniques to study the selective role of individual orbitals.

To date, HHG in H_2O has been observed only with 800 nm light from microdroplets [7] and with 3.6 μm light from liquid [8]. Both experiments sought to enhance the efficiency of the HHG process by exploiting the collective processes arising from high densities. In this Letter we present results on HHG experiments in gas-phase H_2O molecules by using 800 and 1300 nm light at intensities near and above saturation. We produce harmonics as high as the 39th at 800 nm and the 91st at 1300 nm. To the best of our knowledge, these are the highest photon energies observed in H_2O. We show extension of the HHG cutoff in H_2O well beyond that of Xe for both driving wavelengths, indicating suppression of ionization due to quantum interferences.

HHG with 800 nm (or 1300 nm) light was produced in a 50-cm-long semi-infinite gas cell (SIGC) having a 150 μm pinhole [or in a 10-mm-long finite gas cell (FGC) with 600 μm apertures]. 800 nm light pulses from a Ti:sapphire regenerative amplifier (~3.5 mJ, 40 fs, 100 Hz) were focused by using a $f = 75$ cm achromatic lens through a 2-mm-thick uncoated fused silica window. 1300 nm light pulses, produced by an optical parametric amplifier (1.2 mJ, 80 fs), were focused with a $f = 30$ cm lens through a 2-mm-thick calcium fluoride window. Efficiency of harmonic generation in the FGC is ~2 times lower than in the SIGC [9], but it allowed us to work at higher intensities with the longer-wavelength light using a shorter focal length lens. The intensity of the laser beam was altered by a combination of a half-wave plate and a thin-film polarizer. The harmonics were dispersed by a flat-field concave grating at grazing incidence onto a microchannel plate detector coupled to a phosphor screen and then imaged by a CCD camera. The harmonic spectra were obtained under optimal phase-matching conditions by adjusting the laser focus with respect to the pinhole, the pressure in the gas cell, and the laser chirp. H_2O was introduced into the gas cell without a carrier gas by heating a glass ampule with distilled water up to 50°C. This increased the partial vapor pressure of H_2O from 17.5 Torr at room temperature to 92.5 Torr. The optimum gas input pressure for which we saw the largest cutoff in both the molecule and the atom was 120 mTorr for Xe and 300 mTorr for H_2O. A fast ionization gauge was used to calibrate the incident intensity for both wavelengths of light by using the previously employed methodology [9].

Figure 1 shows the harmonic spectra of H_2O at different intensities and of Xe at an intensity of 1.5×10^{14} W/cm^2 obtained by using 800 nm laser pulses. The intensities used are near and above the saturation intensity of H_2O. We observe extension of the H_2O cutoff beyond that of Xe at all intensities by several harmonic orders. The block arrows in the H_2O spectra indicate the observed cutoff harmonics in Xe at those intensities. The three-step HHG model [3] predicts the cutoff photon energy to be $I_p + 3.17U_p$, where I_p is the ionization potential and U_p is the quiver energy. Accordingly, the

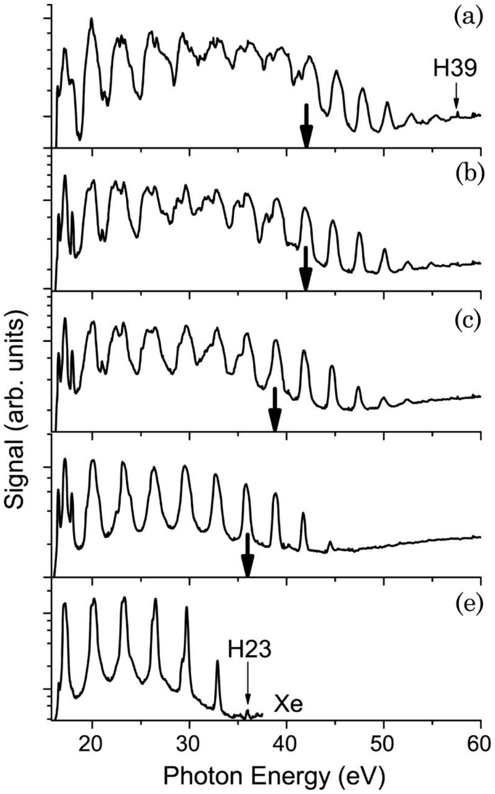

Fig. 1. Harmonic spectra for (a)–(d) H_2O and (e) Xe using 800 nm light in a semi-infinite gas cell at intensities (a) 5.0×10^{14} W/cm^2, (b) 3.5×10^{14} W/cm^2, (c) 2.5×10^{14} W/cm^2, (d) and (e) 1.5×10^{14} W/cm^2. Bold arrows in (a)–(d) indicate observed cutoffs in Xe at corresponding intensities.

cutoff photon energies for Xe ($I_p = 12.13$ eV) and H_2O ($I_p = 12.6$ eV) should be identical at the same intensity. We determine the experimental cutoff to be the highest visible harmonic above the noise level. For Xe it is the 23rd harmonic (three-step model predicts the 25th) at an intensity of 1.5×10^{14} W/cm^2, close to the saturation intensity. At higher intensities beyond saturation, the position of cutoff harmonics in Xe does not scale with intensity and remains approximately the same because the valence electron is completely ionized. Previous studies on HHG in H_2O used dense nonlinear media such as microdroplets (800 nm) [7] and liquid (3.6 μm) [8]. In spite of the important role played by collective processes in enhancing the harmonic efficiency, the highest photon energy observed was ~42 eV. In contrast, we observed photon energies as high as ~60 eV. The efficiency of the HHG in H_2O using the SIGC is estimated to be $\sim 10^{-5}$, similar to that of Ar [9].

The extension of the HHG cutoff in H_2O is due to suppressed ionization in molecules whose orbital symmetry has a nodal plane. The HOMO and the next two underlying orbitals of H_2O all have p-orbital-like character with a single nodal plane. Electron wave packets originating from either side of the nodal plane with opposite phases undergo destructive interference while tunneling. The signature of this quantum interference can be observed as higher saturation intensities [10,11] and an extension of the cutoff harmonics [12]. To ensure that the extension of the cutoff is due to suppression of ionization and not to some physical mechanism during the subsequent steps of the HHG process, we measured the saturation intensities of Xe and H_2O. The measured saturation intensities are $\sim 10^{14}$ W/cm^2 for Xe, in agreement with the model based on ADK (Ammosov–Delone–Krainov) ionization rates [13], and $\sim 1.4 \times 10^{14}$ W/cm^2 for H_2O. In our experiments, no effort has been made to align the molecules or to selectively interact with a specific orbital.

Figure 2 shows the divergence of the harmonics produced by 800 nm light, under optimal phase-matching conditions, for both H_2O and Xe, as measured on the microchannel plates. The divergence is very low and decreases with increasing harmonic order, following an empirical relation between the diameter of the qth harmonic and the fundamental, D, given by $D/(q)^{1/2}$ (solid curve in the figure). The spatial profiles of the harmonics are smooth and nearly Gaussian in shape, as shown in the inset. However, beyond the saturation intensity, broadening and distortion of the spatial profile of the harmonics is observed, which could be due to plasma formation. A good spatial mode is crucial to extract the harmonic phase and amplitude from interferometric measurements. This information is important to understand the contribution of multiple orbitals to the HHG signal [5,6].

Harmonic generation in molecules is best investigated at longer wavelengths, since the ionization process is adiabatic and the quiver energy of the recolliding electron is high, leading to higher photon energies. At long wavelengths, a given harmonic can be generated at much lower intensity, thus reducing the ionization of the nonlinear medium. This increases the photon energy range over which good phase matching can be achieved [14]. Higher photon energies and better phase matching magnify the effect of suppressed ionization and leads to a significant extension of the cutoff harmonics. However, there is a trade-off in harmonic efficiency that scales approximately with laser wavelength as $\lambda^{-5.5}$ [15]. Figure 3 shows the comparison of the harmonic spectra for H_2O and Xe at an intensity of $\sim 1.5 \times 10^{14}$ W/cm^2 using 1300 nm driving pulses. At this wavelength, the extension of the cutoff region in H_2O is much more dramatic. The cutoff energies are ~87 eV for H_2O and ~60 eV for Xe. Extended

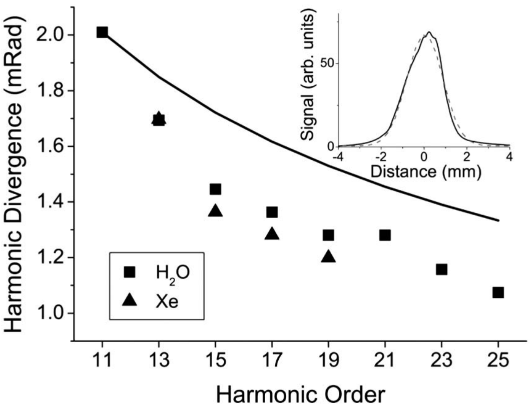

Fig. 2. Divergence of harmonic orders obtined by using 800 nm light at an intensity of 3.5×10^{14} W/cm^2. Solid curve, calculated divergence based on input beam parameters. Inset, spatial profile of the 11th harmonic (solid curve) for H_2O with a Gaussian fit (dashed curve).

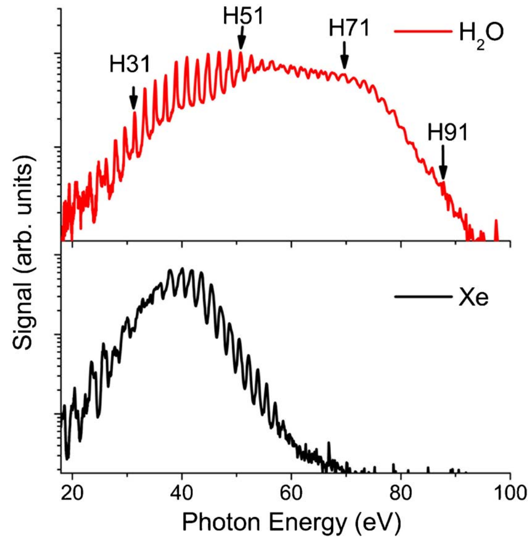

Fig. 3. (Color online) Comparison of harmonic spectra for H_2O (upper panel) and Xe (lower panel) using 1300 nm light at an intensity of $\sim 1.5 \times 10^{14}$ W/cm^2.

harmonic generation will allow the study of electronic and geometric structure of the molecule, as multiorbital and multicenter interferences appear at higher photon energies.

In conclusion, we have efficiently generated high harmonics in H_2O with photon energies up to ~60 and ~87 eV by using 800 and 1300 nm light. We observed signatures of suppressed ionization due to orbital symmetry by comparing cutoff harmonics in H_2O with Xe. Since H_2O molecules can be easily aligned, one should be able to selectively study the contribution of different orbitals to ionization and hence harmonic generation. In H_2O, the HOMO and HOMO-1 are separated in energy by 2.2 eV, whereas HOMO-1 and HOMO-2 differ by 3.7 eV, making H_2O an ideal candidate for such studies.

The authors gratefully acknowledge support from the Natural Science and Engineering Research Council of Canada and technical assistance from François Poitras and Antoine Laramée at Advanced Laser Light Source.

References

1. M. Hentschel, R. Kienberger, Ch. Spielmann, G. A. Reider, N. Milosevic, T. Brabec, P. Corkum, U. Heinzmann, M. Drescher, and F. Krausz, Nature **414**, 509 (2001).
2. J. Itatani, J. Levesque, D. Zeidler, H. Niikura, H. Pépin, J. C. Kieffer, P. B. Corkum, and D. M. Villeneuve, Nature **432**, 867 (2004).
3. P. B. Corkum, Phys. Rev. Lett. **71**, 1994 (1993).
4. X. M. Tong, Z. X. Zhao, and C. D. Lin, Phys. Rev. A **66**, 033402 (2002).
5. O. Smirnova, Y. Mairesse, S. Patchkovskii, N. Dudovich, D. M. Villeneuve, P. B. Corkum, and M. Y. Ivanov, Nature **460**, 972 (2009).
6. S.-K Son and S.-I. Chu, Chem. Phys. **366**, 91 (2009).
7. A. Flettner, T. Pfeifer, D. Walter, C. Winterfeldt, C. Spielmann, and G. Gerber, Appl. Phys. B **77**, 747 (2003).
8. A. D. DiChiara, E. Sistrunk, T. A. Miller, P. Agostini, and L. F. DiMauro, Opt. Express **17**, 20959 (2009).
9. J. -P Brichta, M. C. H. Wong, J. B. Bertrand, H. -C. Bandulet, D. M. Rayner, and V. R. Bhardwaj, Phys. Rev. A **79**, 033404 (2009).
10. A. Talebpour, C. -Y. Chien, and S. L. Chin, J. Phys. B **29**, L677 (1996).
11. V. R. Bhardwaj, P. B. Corkum, and D. M. Rayner, Phys. Rev. Lett. **91**, 203004 (2003).
12. B. Shan, X. M. Tong, Z. X. Zhao, Z. Cheng, and C. D. Lin, Phys. Rev. A **66**, 061401(R) (2002).
13. M. V. Ammosov, N. B. Delone, and V. P. Krainov, Sov. Phys. JETP **64**, 1191 (1986).
14. T. Popmintchev, M. -C. Chen, O. Cohen, M. E. Grisham, J. J. Rocca, M. M. Murname, and H. C. Kapteyn, Opt. Lett. **33**, 2128–2130 (2008).
15. A. D. Shiner, C. Trallero-Herrero, N. Kajumba, H. -C. Bandulet, D. Comtois, F. Légaré, M. Giguère, J. -C. Kieffer, P. B. Corkum, and D. M. Villeneuve, Phys. Rev. Lett. **103**, 073902 (2009).

Chapter 5

Isomeric effects in high harmonic generation

5.1 High-harmonic spectroscopy of molecular stereoisomers (Publication 4)

M. C. H. Wong, J.-P. Brichta, M. Spanner, S. Patchkovskii, and V. R. Bhardwaj
High-harmonic spectroscopy of molecular isomers
Physical Review A **84**, 051403(R) (2011)
Physical Review A **85**, 049901(E) (2012)

5.1.1 Author contribution

M. C. H. Wong and J.-P. Brichta performed the experiments at ALLS in Varennes, QC. M. Spanner performed the angle-dependent ionization calculations. M. C. H. Wong conducted the analysis of the experimental results and wrote the first draft of the manuscript. All authors contributed to the final manuscript.

A small erratum was issued in 2012 which corrected the half-cycle ionization yields for *cis*-$C_2H_2Cl_2$.

RAPID COMMUNICATIONS

PHYSICAL REVIEW A **84**, 051403(R) (2011)

High-harmonic spectroscopy of molecular isomers

M. C. H. Wong,[1] J.-P. Brichta,[1] M. Spanner,[2] S. Patchkovskii,[2] and V. R. Bhardwaj[1,*]
[1]*Department of Physics, University of Ottawa, 150 Louis-Pasteur, Ottawa, Ontario, Canada K1N 6N5*
[2]*National Research Council of Canada, 100 Sussex Drive, Ottawa, Ontario, Canada K1A 0R6*

(Received 24 August 2011; published 22 November 2011)

We demonstrate that high-order-harmonic generation (HHG) spectroscopy can be used to probe stereoisomers of randomly oriented 1,2-dichloroethylene ($C_2H_2Cl_2$) and 2-butene (C_4H_8). The high-harmonic spectra of these isomers are distinguishable over a range of laser intensities and wavelengths. Time-dependent numerical calculations of angle-dependent ionization yields for 1,2-dichloroethylene suggest that the harmonic spectra of molecular isomers reflect differences in their strong-field ionization. The subcycle ionization yields for the *cis* isomer are an order of magnitude higher than those for the *trans* isomer. The sensitivity in discrimination of the harmonic spectra of *cis*- and *trans*- isomers is greater than 8 and 5 for 1,2-dichloroethylene and 2-butene, respectively. We show that HHG spectroscopy cannot differentiate the harmonic spectra of the two enantiomers of the chiral molecule propylene oxide (C_3H_6O).

DOI: 10.1103/PhysRevA.84.051403 PACS number(s): 33.80.Rv, 42.65.Ky, 33.20.Lg

The arrangement of atoms in a molecule can influence ion energetics, reaction rates, chemical reactions, and light-matter interactions. Molecular isomers are often identified by their rovibrational absorption fingerprint using infrared, Raman, and microwave spectroscopic techniques [1]. Electronic absorption has also been exploited using wavelength-selective ultraviolet multiphoton ionization [2]. However, collisional techniques based on electron and ion impact had varying degrees of success in linking changes in molecular geometry to dynamical processes. In most cases, the isomers produced similar mass spectra [3–6]. Electron scattering from isomers has only recently demonstrated convincing differences in the absolute total cross sections in the low-energy region [7].

High-harmonic generation (HHG) spectroscopy of simple molecular systems has recently evolved as a new tool to probe electron density in the neutral [8,9] and hole dynamics [10] of an ion via harmonic amplitude, phase, and frequency measurements with angstrom spatial [11] and attosecond temporal resolution. In HHG spectroscopy, strong-field ionization launches an electron wave packet adiabatically into the continuum by tunneling. The wave packet is subsequently driven by the oscillating electric field and recombines with the parent ion, thus emitting high-energy radiation [12]. The ionization step transfers the orbital information onto the harmonic spectra and by treating the recolliding electron as a plane wave, the molecular orbital can be reconstructed [8]. However, extending this technique to complex molecular systems can be difficult due to participation of multiple continua and breakdown of the adiabatic and plane-wave approximations [10,13]. It is therefore unknown whether HHG spectroscopy, with its high spatial and temporal precision, can be used as a sensitive tool to probe complex molecular structure and dynamics.

In this Rapid Communication, we demonstrate that HHG spectroscopy can be used to probe stereoisomers of randomly oriented 1,2-dichloroethylene (1,2-DCE, $C_2H_2Cl_2$) and 2-butene (C_4H_8). We show that differences in strong-field ionization of isomers cause the harmonic spectra to be distinguishable. Theoretically, we find the ionization yields of *cis*-DCE to be ∼8 times higher than that of *trans*-DCE for different wavelengths. Experimentally, the relative ionization probability between the two isomers is reflected in the ratio of their harmonic spectra. Finally, we show that HHG spectroscopy is insensitive to the chirality of an unaligned molecule.

The molecules that we investigated have low ionization potentials (9.62 and 9.58 eV for *cis*- and *trans*-DCE; 9.11 and 9.12 eV for *cis*- and *trans*-2-butene). Therefore, high-harmonic spectra are obtained using long-wavelength light in the range of 1300 to 1800 nm. At long wavelengths the following effects occur: (a) The energy of the recolliding electron scales quadratically with wavelength so the harmonic cutoff can be extended to high photon energies while the laser intensity is kept below or close to the saturation intensity of the molecule as compared to the use of 800 nm light [14]. Harmonics with photon energies greater than 40 to 50 eV are needed to capture molecular and multielectron dynamics [15,16]. (b) Ionization of polyatomic molecules is adiabatic with less fragmentation [17]. (c) High spatial resolution of the HHG spectroscopic method can be achieved, set by the de Broglie wavelength of the recolliding electron. (d) Phase matching for higher-order harmonics is extended and can be achieved at higher pressures since use of lower laser intensities offsets the detrimental effects of the ionized medium [18,19]. (e) The electron spends more time in the continuum, resulting in large transverse spreading of the recolliding electron wave packet. This reduces the recollision probability and, as a consequence, the harmonic signal scales with wavelength as $\lambda^{-5.5}$ [20,21]. To an extent, this limitation is overcome by use of higher pressures.

Wavelength-tunable infrared light pulses of 80 fs were generated at a repetition rate of 100 Hz with a superfluorescence-seeded optical parametric amplifier pumped by 3.5 mJ, 45 fs, 800 nm pulses. The light pulses, whose energies varied from 900 μJ at 1800 nm to 1.3 mJ at 1300 nm, were focused into a differentially pumped gas cell through a 2-mm-thick CaF_2 window by an achromatic lens of focal length 400 mm. The gas cell is 10 mm long with 600 μm apertures. The harmonics, produced in an ensemble of randomly oriented

---

[*] ravi.bhardwaj@uottawa.ca

molecules, were dispersed by a flat-field concave grating at grazing incidence onto a microchannel plate detector coupled to a phosphor screen and then imaged by a charge-coupled device camera. The harmonic spectra are obtained under optimal phase-matching conditions by adjusting the position of the laser focus with respect to the pinholes and the absolute pressure inside the gas cell. Typical densities used in the experiments were (1–3) $\times$ 10^{17} cm^{-3}. The vapor pressures of 1,2-DCE and propylene oxide at room temperature were high enough for them to be introduced into the cell without the use of any carrier gas. The chemicals, acquired from Sigma-Aldrich, have purities of 97% for 1,2-DCE, and 99% for 2-butene and propylene oxide. The intensity of the laser beam was altered between 5 $\times$ 10^{13} and 2 $\times$ 10^{14} W/cm^2 using neutral density filters. Intensity calibration was achieved by monitoring the cutoff harmonics from argon and validated by measuring its saturation intensity using a fast ionization gauge [22,23].

Figure 1(a) shows the harmonic spectra for *cis*- and *trans*-DCE obtained with 1800 nm driving laser pulses at an intensity of 1.1 $\times$ 10^{14} W/cm^2. Although the harmonic spectra of the two isomers are distinctly different, both exhibit an amplitude modulation around 40 eV. *cis*-DCE produces significantly more photons in the plateau region while *trans*-DCE produces more photons in the cutoff region. Figure 1(b) shows the ratio of the harmonic spectra for the two isomers. A value of unity corresponds to the harmonic signals being equal. Since the ionization potentials of the two isomers are nearly identical, similar spectra are expected from the semiclassical model of HHG extended to molecules. The harmonic spectra of the isomers are distinct even when different pressures are used, resulting in similar-looking ratios to those in Fig. 1(b) but with different magnitudes. The differences in harmonic spectra between the two isomers persist for several wavelengths and over a range of laser intensities.

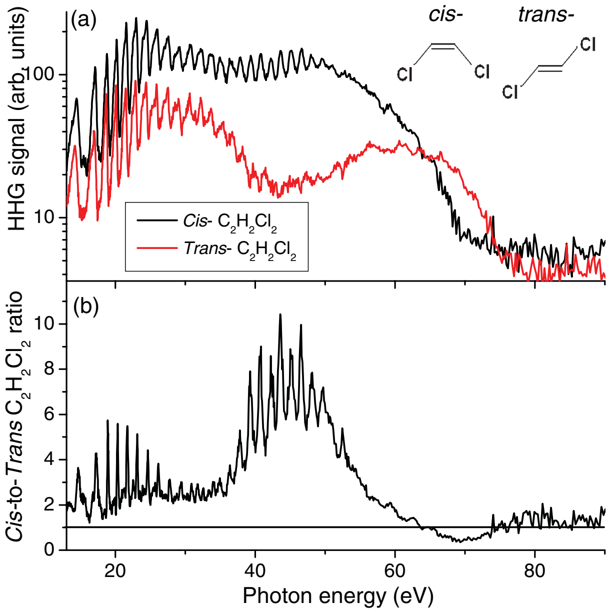

FIG. 1. (Color online) (a) High-harmonic spectra for *cis*- and *trans*-1,2-dichloroethylene obtained using 1800 nm light at an intensity of 1.1 $\times$ 10^{14} W/cm^2. (b) *cis*- to *trans*-1,2-dichloroethylene harmonic ratio of spectra from (a).

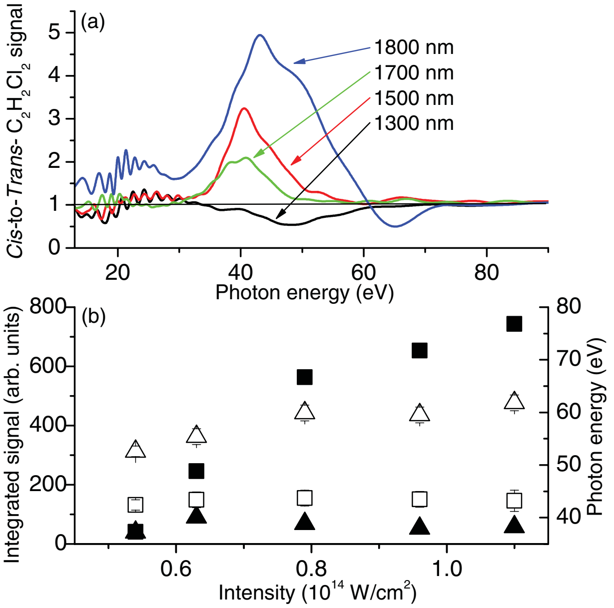

FIG. 2. (Color online) (a) *cis* to *trans* harmonic ratio of 1,2-dichloroethylene for different wavelengths at an intensity of 0.8 $\times$ 10^{14} W/cm^2. (b) Features of the harmonic ratio as a function of intensity using 1800 nm light; ■, the total integrated signal (left scale) of the peak above unity; □, the photon energy (right scale) of the position of the peak above unity; ▲, the total integrated signal of the peak below unity; △, the photon energy (right scale) of the position of the peak below unity.

Figure 2(a) shows the wavelength dependence of the *cis* to *trans* ratio between the harmonic spectra of 1,2-DCE obtained at an intensity of ~8 $\times$ 10^{13} W/cm^2. The curves have been smoothed for clarity. At 1300 nm, the two isomers produce similar spectra up to ~30 eV. Beyond this energy, the *trans*-DCE signal dominates, producing more high-energy photons up to 55 eV. As the driving wavelength is increased, two things occur. First, the harmonic spectra are extended to higher photon energies; at 1800 nm, photons up to 75 eV are produced. Second, the *cis*-DCE signal starts to dominate at lower photon energies. As the wavelength increases, the position of the peak above unity shifts marginally by ~2 eV. The position of the trough, corresponding to the *trans*-DCE signal being dominant, shifts from 50 eV at 1300 nm to 65 eV at 1800 nm.

Figure 2(b) shows the intensity dependence of the integrated signal for the ratio above unity (corresponding to the *cis*-DCE signal being dominant) for 1800 nm light. The signal from *cis*-DCE is greater than that for *trans*-DCE by almost an order of magnitude. The position of the peak above unity does not change with laser intensity. Also shown is the position of the trough below unity (corresponding to the *trans*-DCE signal being dominant) which shifts with laser intensity by ~10 eV and is associated with the cutoff harmonics. The integrated signal of the trough below unity does not vary much with intensity.

We now return to the amplitude modulations in the harmonic spectra in Fig. 1(a). The position of the amplitude minimum at ∼40 eV is independent of laser intensity and wavelength (see Fig. 2). Spectral minima of this nature have previously been shown to originate from electronic structure associated with the Cooper minima in the photoionization cross sections of molecules containing chlorine atoms [16,24]. Since recombination is the inverse of photoionization [25], contrast in the harmonic spectra near the Cooper minimum indicates significant difference in the photoionization cross sections of the two isomers.

We calculated the angle-dependent ionization yields using the time-dependent numerical *ab initio* method outlined in [26]. This method uses multielectron quantum chemistry wave functions to represent the multielectron bound states of the neutral atom and cation, and couples these states to Cartesian grids used to represent the continuum states. In the present calculations, we computed the ground state of the neutral and ionic systems using GAMESS [27] with the augmented correlation consistent polarized valence triple-zeta (aug-cc-pVTZ) basis set [28,29] at the Hartree-Fock level. The continuum grid extended to ±15 a.u. in all directions with a grid step size of 0.2 a.u. The time-dependent equations of [26] were integrated using the leapfrog method with a time step of 0.002 66 a.u.

The system is initiated with the whole population in the neutral ground state and then exposed to a half cycle of the carrier oscillations. We use only a half cycle in the calculation of the ionization yield since this is the yield relevant to the subcycle dynamics of the first step in HHG. Further, using only a half cycle allows us to capture the asymmetries in the subcycle ionization yields for the *cis* isomer. We used absorbing boundaries [30] with a width of 4.3 a.u. at the edges of the continuum grid to prevent reflection of the outgoing electron flux and to calculate the ionization yield by monitoring the population absorbed at the grid edges. The calculation was repeated with several different angles between the molecular axis and the laser polarization direction in order to capture the full angular dependence of the ionization yield.

Figure 3(a) shows the highest occupied molecular orbital (HOMO) of *cis*-DCE and the angular ionization distribution. The HOMO of *cis*-DCE ionizes preferentially when the laser polarization is parallel to the molecular dipole. Figure 3(b) shows the HOMO of *trans*-DCE and the angular ionization distribution. Here the molecule ionizes preferentially along the molecular axis. The half-cycle ionization yields of the two isomers at 800 nm are 10.1% for *cis* and 1.1% for *trans* at an intensity of 1.5×10^{14} W/cm^2. Although ionization yields vary with intensity, the relative differences between the two isomers remain the same. At an intensity of 10^{14} W/cm^2, the yields are 6.6% and 0.8% for 1300 nm and 7.3% and 0.96% for 1500 nm. The ionization yields of *cis*-DCE are ∼7–9 times higher than those of *trans*-DCE. Although we present angular plots for a half-cycle ionization using 800 nm light, calculations for 1300 and 1500 nm distributions show that they look qualitatively similar for all wavelengths considered.

Our experimental results can be interpreted in terms of ionization, the first step in the HHG process. Ionization yields of *cis*-DCE are ∼8 times higher than for *trans*-DCE when 1800 nm light is used. This difference is directly reflected in the ratio of the harmonic spectra of the isomers up to ∼60 eV. Suppression of ionization in *trans*-DCE leads to

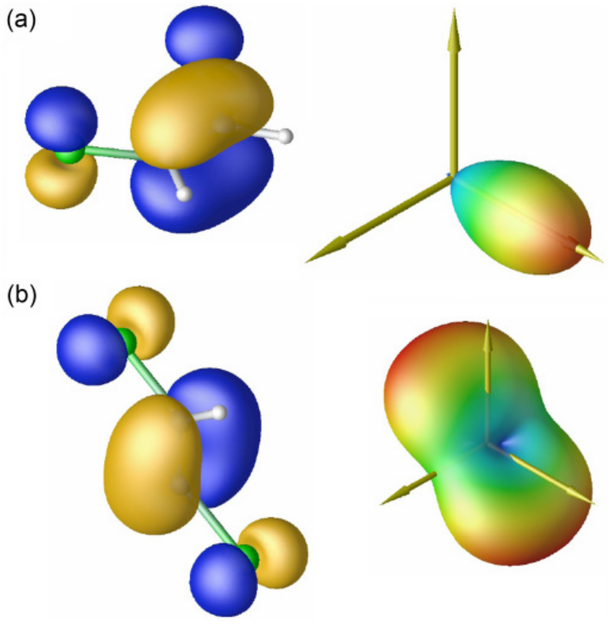

FIG. 3. (Color online) (a) HOMO (left) and angular ionization distribution (right) of (a) *cis* and (b) *trans*-1,2-dichloroethylene. Ionization distributions are calculated at an intensity of 10^{14} W/cm^2 using 800 nm light.

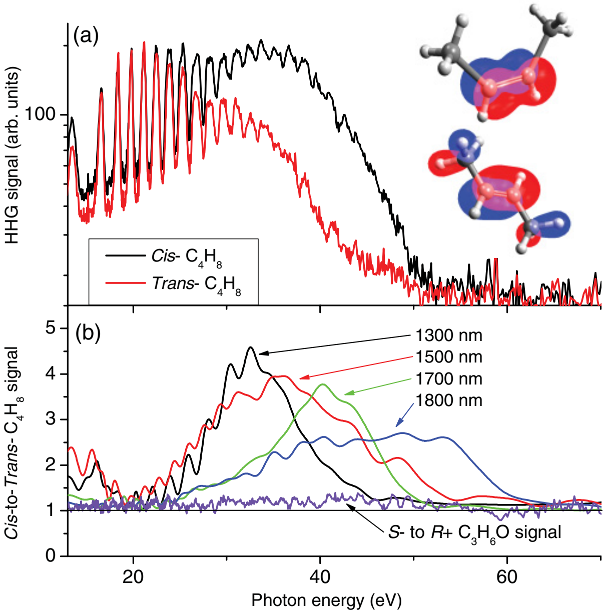

FIG. 4. (Color online) (a) High-harmonic spectra for *cis*- and *trans*-2-butene obtained using 1700 nm light at an intensity of 0.8×10^{14} W/cm^2. (b) *cis*- to *trans*- harmonic ratio of 2-butene at wavelengths 1300–1800 nm at an intensity of 0.9×10^{14} W/cm^2 and the $S-$ to $R+$ harmonic ratio of propylene oxide using 1800 nm light at an intensity of 10^{14} W/cm^2.

extension of the harmonic cutoff, especially when the laser intensity is above saturation [31], and this extension has been observed in simple molecular systems [32]. As a result, *trans*-DCE dominates in the 60 to 75 eV photon energy range (see Fig. 1). When the laser intensity or wavelength is increased, the harmonic cutoff is extended so the peak in the region where *trans*-DCE is dominant shifts to higher energies. Recombination, the final step in the HHG process, can also be influenced by both electronic and molecular structure [9,10,33]. The isomeric effects that we have so far demonstrated are not unique to 1,2-DCE. They should be present in all molecular isomers that differ in their orbital symmetries [34].

Figure 4(a) shows the harmonic spectra for *cis*- and *trans*-2-butene obtained using 1700 nm light at an intensity of 0.8×10^{14} W/cm^2. *Cis*-2-butene is valence isoelectronic to *cis*-DCE. Unlike 1,2-DCE, *cis*-2-butene produces more photons over a range of harmonic energies while *trans*-2-butene is never dominant. Figure 4(b) shows the wavelength dependence of the *cis* to *trans* ratio of the harmonic spectra of 2-butene obtained at an intensity of 0.9×10^{14} W/cm^2. The position of the peak above unity (corresponding to *cis*-2-butene being dominant) shifts to higher energies with increasing wavelength, and the harmonic cutoff extends to higher energies. These results indicate that the relative ionization probabilities of the two isomers differ by a factor of 5. Also shown is the ratio of the harmonic spectra of the left- and right-handed enantiomers of the chiral molecule propylene oxide (C_3H_6O) using 1800 nm light at an intensity of 10^{14} W/cm^2. Both enantiomers produced identical harmonic spectra, resulting in a ratio that is close to unity; an expected result since ionization of unaligned enantiomers should be identical. This outcome is consistent for all wavelengths used (1500–1800 nm) and confirms our interpretation of the isomeric effects.

The ability to distinguish molecular isomers by HHG spectroscopy combined with its high spatial and temporal resolution enables the study of isomerization dynamics. Such a study was recently conducted in the ethylene cation using an extreme-ultraviolet pump and near-infrared probe configuration [35]. The possibility of extracting electronic and molecular structure information from HHG in complex molecules would widen the prospects of using HHG spectroscopy as a sensitive tool to probe not only electron dynamics but also coupled electronic and nuclear dynamics.

The authors wish to acknowledge A. Laramée and F. Poitras from the ALLS in Montreal for expert technical assistance. This research is supported by the NSERC and CFI.

---

[1] E. T. J. Nibbering, H. Fidder, and E. Pines, Annu. Rev. Phys. Chem. **56**, 337 (2005).
[2] J. W. Hudgens, M. Seaver, and J. J. DeCorpo, J. Phys. Chem. **85**, 761 (1981).
[3] J.-Y. Zhang *et al.*, Int. J. Mass Spec. Ion Proc. **110**, 103 (1991).
[4] C. Sottani *et al.*, Org. Mass Spec. **27**, 169 (1992).
[5] V. A. Mikhailov *et al.*, J. Phys. Chem. A **110**, 5760 (2006).
[6] P. Sobocinski *et al.*, J. Phys.: Conf. Ser. **101**, 012006 (2008).
[7] C. Szmytkowski and S. Kwitnewski, J. Phys. B **36**, 4865 (2003).
[8] J. Itatani *et al.*, Nature (London) **432**, 867 (2004).
[9] T. Kanai, S. Minemoto, and H. Sakai, Nature (London) **435**, 470 (2005).
[10] O. Smirnova *et al.*, Nature (London) **460**, 972 (2009).
[11] M. Y. Ivanov and J. P. Marangos, J. Mod. Opt. **54**, 899 (2007).
[12] P. B. Corkum, Phys. Rev. Lett. **71**, 1994 (1993).
[13] W. Li *et al.*, Science **322**, 1207 (2008).
[14] B. Shan and Z. Chang, Phys. Rev. A **65**, 011804(R) (2001).
[15] R. Torres *et al.*, Opt. Express **18**, 3174 (2010).
[16] M. C. H. Wong, J.-P. Brichta, and V. R. Bhardwaj, Phys. Rev. A **81**, 061402(R) (2010).
[17] V. R. Bhardwaj *et al.*, Phys. Rev. Lett. **87**, 253003 (2001).
[18] E. J. Takahashi *et al.*, Phys. Rev. Lett. **101**, 253901 (2008).
[19] T. Popmintchev *et al.*, Opt. Lett. **33**, 2128 (2008).
[20] J. Tate *et al.*, Phys. Rev. Lett. **98**, 013901 (2007).
[21] A. D. Shiner *et al.*, Phys. Rev. Lett. **103**, 073902 (2009).
[22] S. M. Hankin *et al.*, Phys. Rev. A **64**, 013405 (2001).
[23] J.-P. Brichta *et al.*, Phys. Rev. A **79**, 033404 (2009).
[24] T. A. Carlson *et al.*, Z. Phys. D **2**, 309 (1986).
[25] A. D. Shiner *et al.*, Nat. Phys. **7**, 464 (2011).
[26] M. Spanner and S. Patchkovskii, Phys. Rev. A **80**, 063411 (2009).
[27] M. W. Schmidt *et al.*, J. Comput. Chem. **14**, 1347 (1993).
[28] T. H. Dunning Jr., J. Chem. Phys. **90**, 1007 (1989).
[29] D. E. Woon and T. H. Dunning Jr., J. Chem. Phys. **98**, 1358 (1993).
[30] D. E. Manolopoulos, J. Chem. Phys. **117**, 9552 (2002).
[31] Saturation intensity of xenon [ionization potential (IP) ~12 eV] is ~10^{14} W/cm^2. For molecules with IP ~ 9–10 eV the saturation intensity would be ~5×10^{13} W/cm^2 [22].
[32] B. Shan *et al.*, Phys. Rev. A **66**, 061401(R) (2002).
[33] M. Lein *et al.*, Phys. Rev. A **66**, 023805 (2002).
[34] Unpublished data on the structural isomers butane and isobutane, and 1-propanol and isopropanol.
[35] J. van Tilborg *et al.*, J. Phys.: Conf. Ser. **194**, 012015 (2009).

PHYSICAL REVIEW A **85**, 049901(E) (2012)

Erratum: High-harmonic spectroscopy of molecular isomers [Phys. Rev. A 84, 051403(R) (2011)]

M. C. H. Wong, J.-P. Brichta, M. Spanner, S. Patchkovskii, and V. R. Bhardwaj

(Received 12 March 2012; published 5 April 2012)

DOI: 10.1103/PhysRevA.85.049901 PACS number(s): 33.80.Rv, 42.65.Ky, 33.20.Lg, 99.10.Cd

In extending the single-channel ionization calculations of $C_2H_2Cl_2$ presented in our paper to the multichannel case, an error was found in the computational results presented in our paper. The permanent electronic dipole of the *cis*-isomer was included in the ionization calculation with a sign error. The results for the *trans*-isomer were unaffected by this error.

We have recalculated the Hartree-Fock (HF) highest occupied molecular orbital (HOMO) *cis*-isomer results, as was presented in our paper, with the correct permanent dipole. The corrected half-cycle ionization yields of the *cis*-isomer are no longer an order-of-magnitude larger than the corresponding *trans*-isomer ionization yields. The corrected half-cycle ionization yields for the *cis*-isomer are 1.8% at 800 nm and 1.5×10^{14} W/cm^2, 1.0% at 1300 nm and 10^{14} W/cm^2, and 1.3% at 1500 nm and 10^{14} W/cm^2. These corrected *cis*-isomer ionization yields are about a factor of 2 larger than the corresponding *trans*-isomer ionization yields. Though this does not change the physical interpretation of our results, the statement made in our paper that the differences in high-order harmonic generation (HHG) spectra directly reflect the differences in the ionization yields is no longer true.

The figure [Fig. 3(a) in the original paper] plots the corrected *cis*-isomer orientation dependence of strong-field ionization for the 800 nm case, at the HF level of electronic structure used in our paper. The angle in the orientation-dependent ionization yields is the angle between the fixed molecular axis and the force exerted by the laser field on the electron. The corrected HF *cis*-isomer orientation dependence of half-cycle strong-field ionization is qualitatively similar to the corresponding result presented in our paper, with the main difference being that it is now a little bit wider in the plane of the molecule. Please also note the corrected value for the intensity in the caption to Fig. 3.

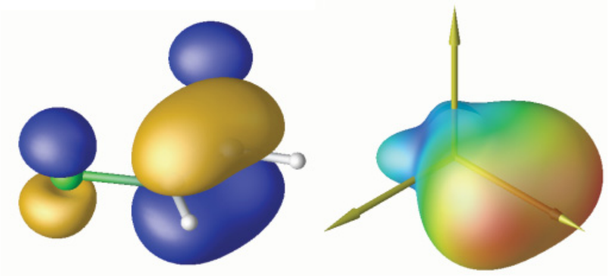

FIG. 3. (Color online) Left: Dyson orbitals of the *cis* HOMO ionization channel. Right: Orientation dependence of the ionization probability. Intensity distributions are calculated at an intensity of 1.5×10^{14} W/cm^2 using 800 nm light.

5.2 High-harmonic spectroscopy of structural isomers (Publication 6)

M. C. H. Wong, M. Spanner, J.-P. Brichta, S. Patchkovskii, and V. R. Bhardwaj
High-harmonic spectroscopy of structural isomers
In preparation (2014)

5.2.1 Author contribution

M. C. H. Wong performed the experiments at ALLS in Varennes, QC. M. Spanner performed the angle-dependent ionization calculations. M. C. H. Wong conducted the analysis of the experimental results and wrote the first draft of the manuscript. All authors contributed to the final manuscript.

High harmonic spectroscopy of structural isomers

M. C. H. Wong[1], M. Spanner[2], J.-P. Brichta[1], S. Patchkovskii[2], and V. R. Bhardwaj[1*]
[1]*Department of Physics, University of Ottawa,*
150 Louis-Pasteur, Ottawa, Ontario, K1N 6N5, Canada
[2]*National Research Council of Canada,*
100 Sussex Drive, Ottawa, Ontario, K1A 0R6, Canada

Abstract

High harmonic spectra of molecular isomers enable us to probe the dependence of molecular structure on ionization and recombination in a strong laser field. We compare detailed measurements of high harmonic generation (HHG) in various randomly oriented polyatomic molecules (C_4H_8, C_4H_{10}, and C_3H_8O) and show that harmonic spectra differ due to slight changes in molecular structure such as addition of a double bond or adding a hydroxyl group. We also observe differences in harmonic spectra between molecular isomers of these molecules and we attribute our results to changes in ionization yields which can be influenced by strong differences in electron localization. Our experimental results on the molecular isomers are confirmed by theoretical calculations of angle-dependent ionization yields. Our experimental results also show that isomeric effects in high harmonic spectroscopy are less apparent for structural isomers compared to *cis-trans* stereoisomers.

PACS numbers: 33.80.Rv, 42.65.Ky, 33.20.Lg

Molecular structure plays an important role to determine physical and chemical properties of a material. The physical characteristics set by the arrangement of a molecule's nuclei and electrons can influence ion energetics, reaction rates, chemical reactions, and light-matter interactions. Isomers play an important role in chemistry, biology and medicine. Isomers can be identified using techniques such as infrared, Raman, microwave, and nuclear magnetic resonance spectroscopy [1, 2]. Other methods including electronic absorption and collisional techniques such as ion and electron scattering have had various degrees of success as well [3–6].

Recent advancements in high-harmonic generation spectroscopy (HHS), where a laser-ionized electron is accelerated and driven back towards its parent ion with high kinetic energy and emitting extreme ultraviolet photons [7], has established it as a suitable tool to probe both molecular structure and dynamics with ångström spatial and attosecond temporal resolution [8]. We have previously shown high harmonic spectra of randomly oriented *cis-trans*-type stereoisomers to be distinguishable over a broad energy range due to variations in the strong field ionization process [9]. As the complexity of the molecular system increases, the participation of multiple orbitals to ionization becomes more important and it is still unknown whether HHS can be a suitable tool to study dynamics in large molecules.

In this paper, we extend the HHS technique to study three polyatomic molecules whose molecular structure differ by either a) a single or double bond: C_4H_{10} (n-butane) to *trans*-C_4H_8) (2-butene) or b) the replacement of a methyl group with a hydroxyl group: C_3H_8O (1-propanol). In addition, we study the molecular isomers of these three molecules in order to see the extent to which the harmonic spectra differ due to the type of isomerization present (structural vs. *cis-trans* stereoisomerization). The extensive differences in high harmonic spectra for these molecules are believed to be a direct result of differences in electron localization which affect the strong-field ionization yields and we perform theoretical calculations of angle-dependent ionization yields to confirm this. The calculations on 2-butene also suggest strong evidence of contribution from different orbitals to the HHG process which are reflected in the experimental results.

High harmonics were produced in a finite gas cell (FGC) of length 10 mm with 0.6 mm apertures. A 30 cm achromatic lens is used to focus $\lambda = 1300 - 1800$ nm near-infrared (NIR) light pulses into the gas cell through a 2 mm thick calcium fluoride window. An optical parametric amplifier pumped by a Ti:sapphire regenerative amplifier (3.5 mJ, 40 fs, 100 Hz, 0.8 μm) produced 80 fs NIR pulses whose energies varied from 0.9 mJ at 1.8 μm to 1.5 mJ at 1.3 μm. The harmonics were dispersed by a flat-field concave grating at grazing incidence onto a micro-channel plate detector coupled to a phosphor screen and then imaged by a charge-coupled device camera. The spectrometer was calibrated by measuring the transmitted spectrum after an aluminum filter. Intensity calibration of the laser beam was achieved by monitoring the cut-off harmonics from HHG in Ar and validated by measuring its saturation intensity using a fast ionization gauge [10, 11]. The position of the laser focus in the gas cell was adjusted such that the highest yield of cut-off harmonics were produced thereby favouring short-trajectories. The vapor pressures of all liquids at room temperature were high enough for them to be introduced into the gas cell without need for a carrier gas. Each liquid underwent a freeze and thaw cycle to minimize contamination in the gas cell.

Since most molecules have ionization potentials (IP) in the range of 9–11 eV, longer wavelengths ($\lambda = 1300 - 1800$ nm) (a) ensure adiabatic ionization, (b) extend the cut-off harmonics to beyond 50 eV which is needed to capture signatures of molecular and multi-electron dynamics [12], and (c) favor phase matching at higher gas pressures, thereby partially offsetting the wavelength scaling of high harmonic signal [13–15].

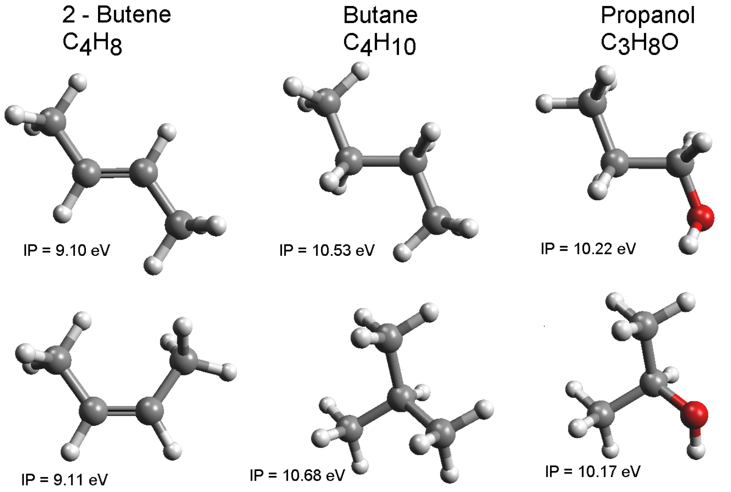

FIG. 1. Schematic of the three molecules butene, butane, propanol, and their molecular isomers along with ionization potentials.

Figure 1 shows a quick schematic of the three molecules: *trans*-2-butene, n-butane, and 1-propanol with their corresponding molecular isomers as well as their IPs. We see that each pair of molecules have almost identical IPs to each other. N-butane is a traditional four carbon chain while *trans*-2-butene contains a double bond between the second and third carbon atoms. 1-propanol is similar to n-butane except that a methyl group on the end is replaced by a hydroxyl group.

In Figure 2a, we show the integrated high harmonic signal for *trans*-2-butene, n-butane, 1-propanol using a wavelength of $\lambda = 1.7\ \mu$m at intensity of 1.1×10^{14} W/cm^2 and a pressure of 8 Torr in the FGC. It is immediately apparent that the magnitude of the harmonic yields in *trans*-2-butene are more than double the yields in the other two molecules. This is expected as *trans*-2-butene is the easiest to ionize as it has the lowest IP thus generating greater harmonic yield. *Trans*-2-butene has also been shown to demonstrate suppressed ionization [9] thus increasing both harmonic yield and cutoff.

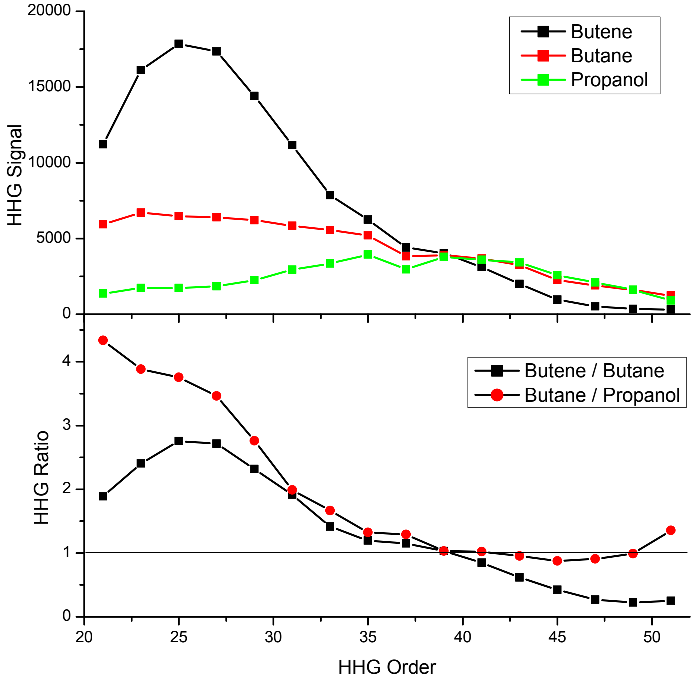

FIG. 2. (a) Integrated signal of *trans*-2-butene, n-butane, and 1-propanol and (b) the ratio of harmonic signal for two sets of molecules at a wavelength of $\lambda = 1700$ nm, an intensity of 1.1×10^{14} W/cm^2, and a pressure of 8 Torr in the FGC.

The spectra for n-butane and 1-propanol exhibit a broad plateau region with considerably lower signal than *trans*-2-butene. The cutoff for all three molecules are similar although *trans*-2-butene's is slightly lower, around harmonic order 45. In figure 2b, we plot two ratios of harmonic signal: *trans*-2-butene to n-butane and n-butane to 1-propanol. The first curve indicates that the double bond in *trans*-2-butene plays quite a significant role during HHG as harmonic yields for this molecule are up to four times that of n-butane. However, the n-butane signal dominates at higher orders due to the lower cutoff of *trans*-2-butene. Figure 3 shows the highest occupied molecular orbitals for the three molecules in question. While the molecular structure of *trans*-2-butene and n-butane are similar, their HOMOs have significant differences in the central carbon chain which can lead to differences in ionization rates.

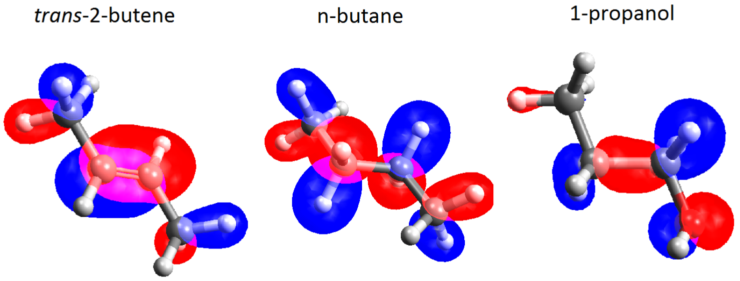

FIG. 3. Highest occupied molecular orbitals for *trans*-2-butene, n-butane, and 1-propanol

Similarly, n-butane's harmonic signal, with respect to that of 1-propanol, is up to three times higher for lower order harmonics but the ratio evens out rapidly. Therefore, we have the impression that the hydroxyl group in 1-propanol can have a detrimental effect on harmonic efficiency. The HOMO of 1-propanol indicates that the majority of electron localization and thus ionization, is situated in the C-O chain which is composed of two *p*-type orbitals, similar to what we see on any C-C chain of n-butane. This could be a factor to support the similarities in ionization for n-butane and 1-propanol.

We now take a closer look at the experimental results for the two isomers of 2-butene. Our previous results [9] demonstrated higher yields of *cis*-2-butene compared to the *trans* isomer. We improve on our previous study in the following discussion. Fig. 4a shows the high harmonic spectra of *cis*- and *trans*-2-butene as a function of photon energy using a wavelength of $\lambda = 1700$ nm, an intensity of 1.1×10^{14} W/cm^2 and pressure of 8 Torr in the FGC. The two isomers have similar harmonic yields at low energies but eventually, the *cis*- yields begin to dominate. Figs. 1b and 1c show energy and wavelength dependent measurements, respectively. In both figures, we show the ratio of the *cis*- to *trans*-2-butene high harmonic spectra as a function of photon energy. A signal of unity demonstrates equal

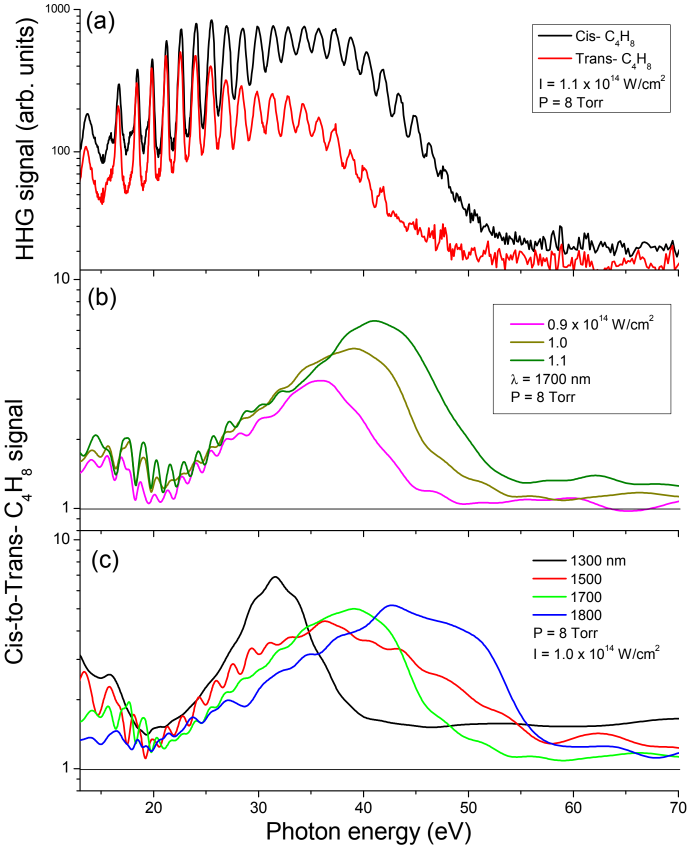

FIG. 4. (a) High harmonic spectra for *cis*- and *trans*-2-butene obtained using $\lambda = 1.7\ \mu$m light at an intensity of 0.9×10^{14} W/cm^2. (b-c) Ratio of HHG signal for *cis*- to *trans*-2-butene for (b) intensities $I = 0.9$–1.1×10^{14} W/cm^2 using $\lambda = 1.7\ \mu$m light and (c) wavelengths $\lambda = 1.3$–$1.8\ \mu$m at an intensity of 1×10^{14} W/cm^2.

harmonic yield for the two isomers. Fig. 1b is measured using a wavelength of $\lambda = 1700$ nm while the harmonic spectra in Fig. 1c have a fixed intensity of 1.0×10^{14} W/cm^2. The pressures used for the samples in the gas cell are indicated in the figure. As evident from the two panels, *cis*-2-butene consistently has higher yields. What's interesting to note is that the yield increases with laser intensity but decreases with wavelength. The peaks of the intensity and wavelength ratio curves increases substantially with intensity and wavelength. This is not surprising as higher intensities will generate both higher yields as well as greater cutoffs. Also, the high harmonic cutoff scales quadratically with wavelength.

Fig. 5 reveals further trends for the high harmonic spectra of 2-butene. Fig. 5a shows the

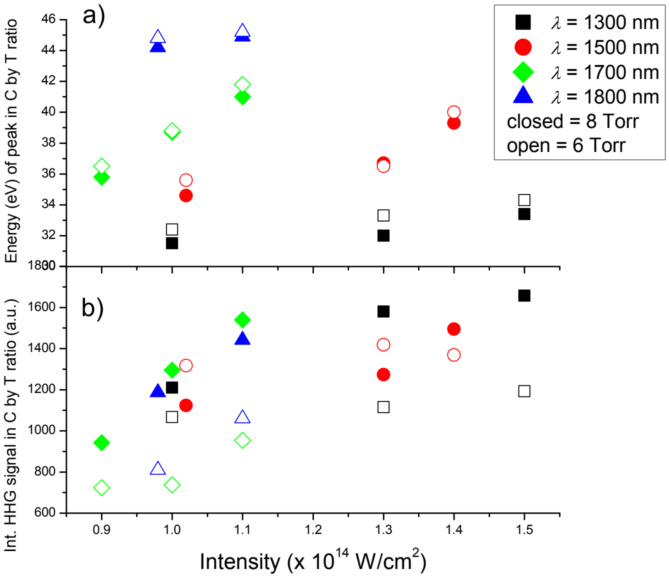

FIG. 5. (a) The position of the peak above unity (in eV) and (b) the integrated signal of the peak above unity of the ratio of HHG signal for *cis* and *trans*-2-butene using wavelengths $\lambda = 1300 - 1800$ nm as a function of intensity for two different pressures, 8 (closed shapes) and 6 Torr (open shapes).

energy of the peak of the *cis* to *trans* harmonic ratio of 2-butene as a function of intensity for wavelengths $\lambda = 1300 - 1800$ nm at two different pressures in the gas cell. The position of the peak shifts to higher energy as wavelength increases due to the extension of cutoff harmonics which scale quadratically with wavelength. Fig. 5b shows the integrated signal of the peak above unity in the harmonic ratio as a function of intensity. For all wavelengths used, the integrated signal increases with intensity. We also see that for a given intensity, the integrated signal of the peak is generally higher for longer wavelengths ($\lambda = 1700$ and 1800 nm) compared to shorter ones ($\lambda = 1300$ and 1500 nm).

Higher pressures in the interaction medium during HHG generally lead to higher ionization yields [16]. This can be seen in Fig. 2b where the integrated signal of the peak above unity in the *cis* to *trans* harmonic ratio is higher at higher pressure. However, an increase in pressure in the sample can also lead to poor phase matching, especially for low energy harmonics. This is why we see that the energy of the peak of the *cis* to *trans* harmonic ratio is slightly higher for lower pressures (see Fig. 5a) at all wavelengths.

The interpretation for our previous results on *cis*- and *trans*-2-dichloroethylene ($C_2H_2Cl_2$)

was best described by the ionization process which is the first step in HHG [9]. Therefore, calculations of angle-dependent ionization yields of *cis*- and *trans*-2-butene should provide us with further understanding of our experimental results.

We calculated the angle-dependent ionization yields using the time-dependent numerical *ab initio* method outlined in [17]. This method uses multi-electron quantum chemistry wave functions to represent the multi-electron bound states of the neutral and cation, and couples these states to Cartesian grids used to represent the continuum states. In the present calculations, we computed the ground state of the neutral and ionic systems using GAMESS [18] with the aug-cc-pVTZ basis set [19, 20] at the Hartree Fock level. The continuum grid extended to ± 15 a.u. in all directions with a grid step size of 0.2 a.u. The time-dependent equations of [17] were integrated using the leap-frog method with a time step of 0.00266 a.u.

The system is initiated with all population in the neutral ground state and then exposed to a half-cycle of the carrier oscillations. We use only a half-cycle in the calculation of the ionization yield since this is the yield relevant to the sub-cycle dynamics of the first step in HHG. Further, using only a half-cycle allows us to capture the asymmetries in the sub-cycle ionization yields for the *cis*- isomer. We used absorbing boundaries [21] with a width of 4.3 a.u. at the edges of the continuum grid to prevent reflection of the outgoing electron flux and to calculate the ionization yield by monitoring the population absorbed at the grid edges. The calculation was repeated with several different angles between the molecular axis and the laser polarization direction in order to capture the full angular dependence of the ionization yield.

Fig. 6 shows the probability of ionization of the calculated HOMO (D0) and HOMO-1 (D1) for both *cis*- and *trans*-2-butene using $\lambda = 1300 - 1700$ nm light at an intensity of 10^{14} W/cm^2. There are significant differences in the ionization trends for the two isomers. For the HOMO, *cis*-2-butene ionizes with greater probability about 2 to 2.5 times higher than the *trans* isomer. At all wavelengths, the ionization probability of the HOMO is roughly 4 times higher than for the HOMO-1 in *cis*-2-butene. This is however not the case for the *trans* isomer as the ionization for the HOMO-1 is about 75% that of the HOMO. This demonstrates that the contribution of different orbitals to the HHG process may be different for the two isomers of 2-butene. The direct measurement of contributions from multiple orbitals for these molecules can be deciphered using the high harmonic interferometry technique of Smirnova *et al.* [22] but requires precise alignment of the molecules with respect to the laser

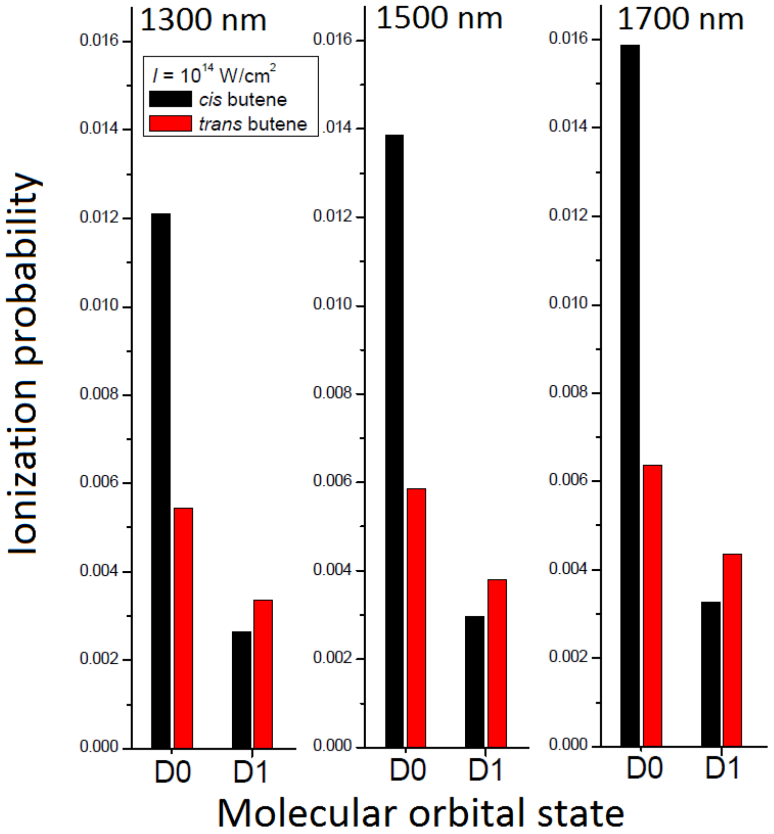

FIG. 6. Ionization probabilities for the calculated HOMO (D0) and HOMO-1 (D1) of *cis*- and *trans*-2-butene using wavelengths $\lambda = 1300 - 1700$ nm light at an intensity of 10^{14} W/cm^2 over a period of a half laser cycle.

polarization. From the ionization calculations, we can safely assume that the majority of harmonic yield for *cis*-2-butene comes from the HOMO whereas the HOMO-1 contribution may be impossible to ignore for *trans*-2-butene. This is not to discount the fact the multiple orbital contribution to HHG can be present for *cis*-2-butene as well.

It must be noted that the ionization probabilities presented in our calculations seem slightly counterintuitive since the experimental ionization energies from photoelectron spectroscopy for molecular orbitals in *cis*- and *trans*-2-butene are almost identical for the first three molecular orbitals: 9.36, 11.65, and 12.76 eV for *cis*- and 9.37, 11.96, and 12.79 eV for *trans*-2-butene [23]. Therefore we would expect similar ionization probabilities for both isomers. Since our calculations show that this is not the case, we again look to the role of the molecular orbitals. Fig. 7 shows the first two calculated molecular orbitals and the orientation dependence of ionization for *cis*- and *trans*-2-butene. The HOMO of *cis*-

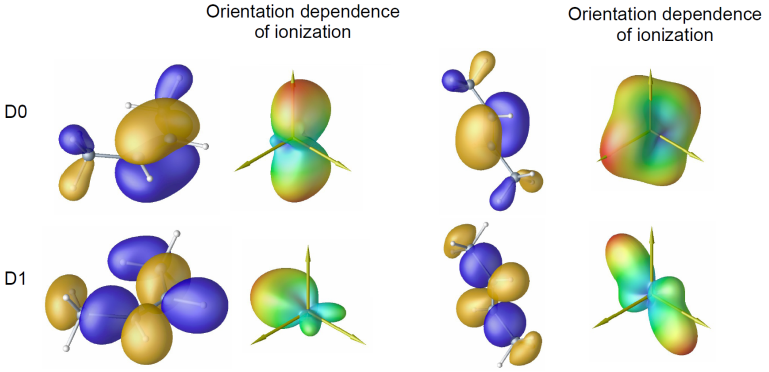

FIG. 7. Calculated molecular orbitals and orientation dependence of ionization for *cis*- and *trans*-2-butene.

2-butene preferentially ionizes perpendicular to the plane of the molecule whereas for the *trans*-isomer, the ionization is high both along the molecular axis as well as perpendicular to its plane. As shown by the accompanying molecular orbital schematics, the molecular axis of *trans*-2-butene is a perfect nodal plane and thus it is possible to have suppression of ionization due to quantum interferences [24, 25] for the orbital of *trans*-2-butene. This could contribute to the low ionization probability for the HOMO of *trans*-2-butene that we see in all three panels of Figure 4. A similar argument could be made for the HOMO-1 of *cis*-2-butene where the orbital preferentially ionizes along a nodal plane made by the single bonded carbon atoms in the molecule.

Our theoretical calculations also provide two valuable insights to our experimental results. First, the fact that the ionization probability of *cis*-2-butene is consistently higher than the *trans* isomer confirms that the ratios shown in Figure 4 should never drop below unity. Second, we also note that our calculations show a slight increase in *cis*- to *trans* ionization probabilities as wavelength increases. This is reflected in Fig. 5b where the integrated signal of the peak above unity is generally higher for longer wavelengths at a given intensity.

We now move to a new system of isomers where, instead of *cis*-*trans* isomerization, the geometric structure is different. Fig. 8a shows the high harmonic spectra of n-butane and isobutane using a wavelength of $\lambda = 1500$ nm at an intensity of 1.5×10^{14} W/cm^2. We choose to work at a higher intensity for n-butane and isobutane in order to increase harmonic yields and cutoff. At all photon energies, isobutane has a higher harmonic yield than n-butane. Figures 8b and 8c show intensity and wavelength dependent measurements, respectively.

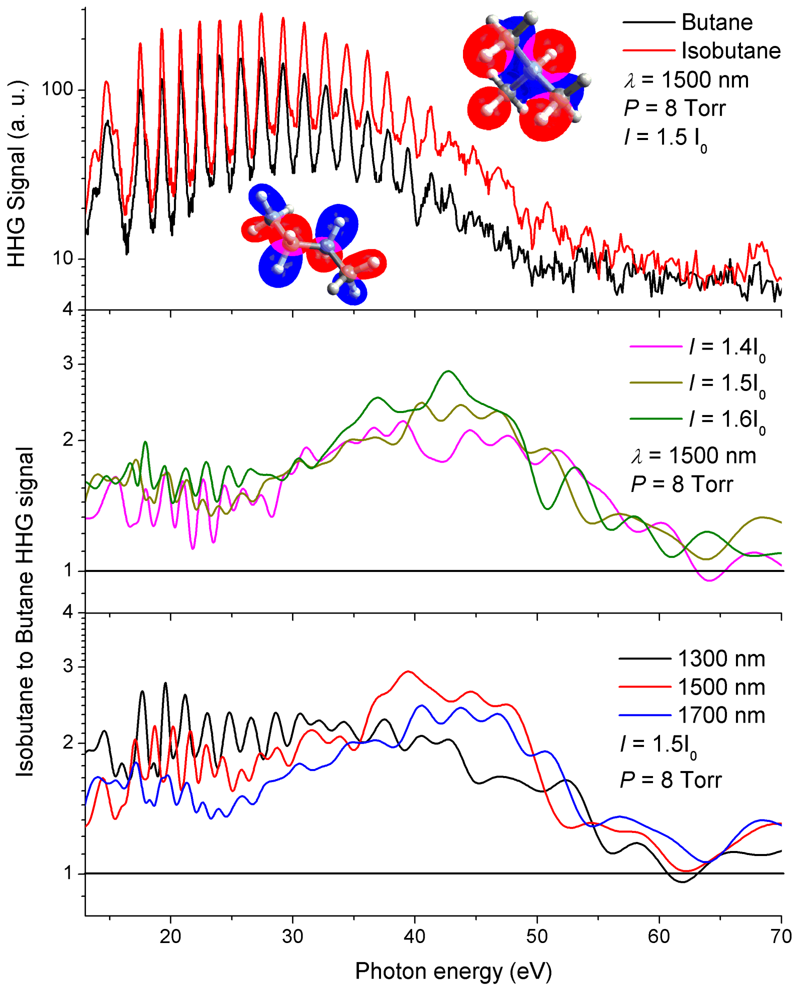

FIG. 8. (a) High harmonic spectra for butane and isobutane obtained using $\lambda = 1.5$ μm light at an intensity of 1.5×10^{14} W/cm^2. (b-c) Ratio of HHG signal for isobutane to butane for (b) intensities $I = 1.4$–1.6×10^{14} W/cm^2 using $\lambda = 1.5$ μm light and (c) wavelengths $\lambda = 1.3$–1.7 μm at an intensity of 1.5×10^{14} W/cm^2. Panel (a) also contains the highest occupied molecular orbitals of butane (top) and isobutane (bottom). N.B. We use the term I_0 to represent 10^{14} W/cm^2 in the figure to save space.

Both figures show the ratio of the isobutane to n-butane high harmonic spectra as a function of photon energy. A slight increase in intensity (Fig. 5b) shows a slightly higher ratio for isobutane to n-butane.

Both the intensity and wavelength dependence of the harmonic ratio show that the harmonic signal of isobutane is, on average, twice the signal of n-butane. However, we do not see the same type of shifting peaks that are evident in the *cis*- and *trans*-2-butene harmonic ratio data. The peak of the ratio stays fairly constant at a photon energy between 40 and 45 eV. The magnitude of the ratio is fairly static and has a range from ∼1.5 to 3 for all intensities and wavelengths used. This is in contrast with 2-butene where the *cis*- to *trans* ratio ranges from 1.5 to ∼7 at $\lambda = 1700$ nm.

Also contained in Fig. 8a are the HOMOs of both n-butane (bottom) and isobutane (top). We see that the HOMO of n-butane is comprised of a chain of *p*-type orbitals surrounding each carbon atom that contains multiple nodal planes while no clear sign of nodal planes are seen in the HOMO of isobutane.

To compare these results on structural isomers, we study high harmonic spectra from the molecules 1-propanol and isopropanol. These molecules have similar molecular structure to butane but with a methyl group replaced by a hydroxyl group. Their ionization potentials are also similar; 10.53 and 10.68 eV for butane and isobutane, and 10.22 and 10.17 eV for propanol and isopropanol (see Fig. 1). In Fig. 2, we saw that n-butane and 1-propanol to have similar harmonic yields for higher photon energies.

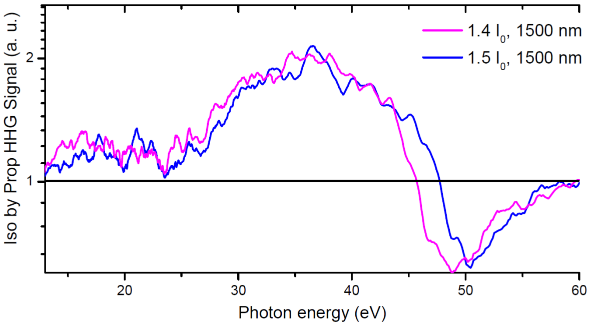

FIG. 9. Ratio of high harmonic signal for isopropanol to 1-propanol for intensities $I = 1.4–1.5\times10^{14}$ W/cm^2 and at a wavelength of $\lambda = 1500$nm.

In Fig. 9, we show the harmonic signal ratio of isopropanol to 1-propanol for intensities $I = 1.4–1.5\times10^{14}$ W/cm^2 at a wavelength of $\lambda = 1500$ nm. Similar to Fig. 8, the harmonic yield of isopropanol is noticeably larger than that of propanol for most photon energies until we reach the cutoff. Again, the range in the ratio of the harmonic yields is small, about 1–2, when compared with the ratios for 2-butene.

As intensity changes, there is no difference in the position of the peak above unity in the ratios but we do see a dip in the ratio near the cutoff energies which was not seen in the butane ratios. The peak is about 5 eV lower than that of the isobutane to n-butane ratio at the same intensity and wavelength but qualitively, these results are suitably consistent with those for the butanes.

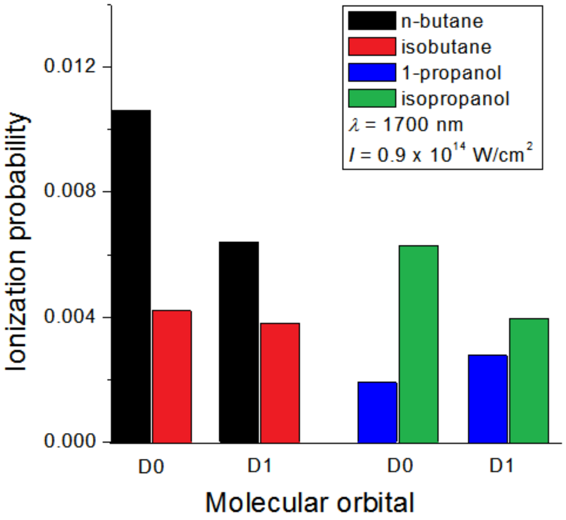

FIG. 10. Ionization probabilities for the calculated HOMO (D0) and HOMO-1 (D1) of n-butane, isobutane, 1-propanol, and isopropanol using $\lambda = 1700$ nm light at an intensity of 0.9×10^{14} W/cm^2 over a period of a half laser cycle.

To confirm our experimental measurements, we calculated ionization probabilities of the HOMO (D0) and HOMO-1 (D1) for the butane and propanol isomers, as shown in Fig. 10. Surprisingly, for the butanes, n-butane has the dominant ionization signal compared to isobutane while for the propanols, isopropanol has higher ionization probability as expected from experiment. The disagreement in butane could be due to the role of contribution from multiple molecular orbitals to ionization. We see that the ionization probability of the HOMO-1 in n-butane is almost as high as the signal for the HOMO. In [22], simultaneous contributions to ionization from up to three molecular orbitals were shown in CO_2 and a similar effect in n-butane may be the cause of the lower signal which we see here. However, the calculations confirm that the n-butane ionization probability is high compared to that of 1-propanol which confirms what we see for harmonics emitted at low photon energy in Fig. 2b.

In conclusion, we have demonstrated the ability for high harmonic spectroscopy to probe a variety of large isomeric systems and show that differences in high harmonic emission can result directly from contribution of multiple molecular orbitals to strong field ionization. The next step would be to measure high harmonic generation in aligned isomers and use high harmonic interferometry to resolve contribution from lower lying orbitals [22]. The experimental results also show that isomeric effects in HHS are lower for structural isomers compared to *cis-trans* stereoisomers. New theoretical and experimental tools for HHG would enable the ability to probe coupled electronic and nuclear dynamics in large molecules and show how they affect isomerization rates and dynamics.

The authors wish to thank T. Brabec and P. Corkum for enlightening discussions and acknowledge A. Laramée and F. Poitras for expert technical assistance. This research is supported by the Natural Science and Engineering Research Council of Canada and the Canadian Foundation for Innovation.

---

* ravi.bhardwaj@uottawa.ca

[1] E. T. J. Nibbering, H. Fidder, and E. Pines, Annu. Rev. Phys. Chem. **56**, 337 (2005).

[2] J. W. Hudgens, M. Seaver, and J. J. DeCorpo, J. Phys. Chem. **85**, 761 (1981).

[3] J.-Y. Zhang *et al.*, Int. J. Mass Spec. Ion Proc. **110**, 103 (1991).

[4] C. Sottani *et al.*, Org. Mass Spec. **27**, 169 (1992).

[5] V. A. Mikhailov *et al.*, J. Phys. Chem. A **110**, 5760 (2006).

[6] P. Sobocinski *et al.*, J. Phys.: Conf. Ser. **101**, 012006 (2008).

[7] P. B. Corkum, Phys. Rev. Lett. **71**, 1994 (1993).

[8] M. Y. Ivanov and J. P. Marangos, J. Mod. Opt. **54**, 899 (2007).

[9] M. C. H. Wong *et al.*, Phys. Rev. A **84**, 051403(R) (2011).

[10] S. M. Hankin *et al.*, Phys. Rev. A **64**, 013405 (2001).

[11] J.-P. Brichta *et al.*, Phys. Rev. A **79**, 033404 (2009).

[12] R. Torres *et al.*, Opt. Express **18**, 3174 (2010).

[13] E. J. Takahashi *et al.*, Phys. Rev. Lett. **101**, 253901 (2008).

[14] T. Popmintchev *et al.*, Opt. Lett. **33**, 2128 (2008).

[15] A. D. Shiner *et al.*, Phys. Rev. Lett. **103**, 073902 (2009).

[16] E. Constant *et al.*, Phys. Rev. Lett. **82**, 1668 (1999).

[17] M. Spanner and S. Patchkovskii, Phys. Rev. A **80**, 063411 (2009).

[18] M. W. Schmidt *et al.*, J. Comput. Chem. **14**, 1347 (1993).

[19] T. H. Dunning Jr., J. Chem. Phys. **90**, 1007 (1989).

[20] D. E. Woon and T. H. Dunning Jr., J. Chem. Phys. **98**, 1358 (1993).

[21] D. E. Manolopoulos, J. Chem. Phys. **117**, 9552 (2002).

[22] O. Smirnova *et al.*, Nature (London) **460**, 972 (2009).

[23] K. Kimura, S. Katsumata, Y. Achiba, T. Yamazaki, and S. Iwata, *Handbook of He I photoelectron spectra of fundamental organic molecules* (Japan Scientific Societies Press, Tokyo, 1981).

[24] V. R. Bhardwaj *et al.*, Phys. Rev. Lett. **87**, 253003 (2001).

[25] M. C. H. Wong, J.-P. Brichta, and V. R. Bhardwaj, Phys. Rev. A **81**, 061402(R) (2010).

Chapter 6

Multi-electron dynamics with XUV and IR pulses

Valence electrons in polyatomic molecules play a key role during chemical reactions that occur on the fs timescale. Using fs lasers and high harmonic generation (HHG), it is possible to time-resolve processes such as photodissociation [79] and vibrational dynamics [80] in simple di- and triatomic molecules. However, the study of time-resolved attosecond electronic processes requires the use of attosecond extreme ultraviolet (XUV) pulses, especially in complex polyatomic systems where electron rearrangement or collective electronic motion can readily occur. Presently, high energy attosecond sources are not yet available but signatures of multi-electron dynamics can still be studied in a multitude of ways.

In this chapter, we present two paths towards the study of multi-electron dynamics in complex molecules. In section 6.1, we look at the ionization of noble gas atoms using attosecond XUV pulses from HHG. The experiments we carry out on Ar and Ne serve as a basis for XUV spectroscopy in polyatomic molecules towards the goal of studying electron dynamics during chemical processes. In section 6.2, we present a study of ionization and fragmentation of C_{60} using few-cycle laser pulses in order to efficiently remove electrons from the molecule to obtain a glimpse of how electron dynamics affect this process. These two studies are integral to understanding how collective electron dynamics are at play in systems from atoms to large molecules.

6.1 Attosecond XUV multiphoton ionization of atoms and molecules

Since the attosecond is the natural timescale of electrons, attosecond pulses will enable spectroscopists to measure electron dynamics involving valence electrons in atoms and molecules. A suitable approach would be to perform a pump-probe experiment using two or more attosecond XUV pulses but at the moment, current attosecond technology is not capable of generating the necessary intensities needed to carry out this type of experiment. For this reason, we pursued the development of a bright XUV source (see Chapter 2) in order to extend nonlinear spectroscopy from the optical to the XUV regime. In this section, we present studies of multiphoton ionization of noble gas atoms using XUV pulses generated in a semi-infinite gas cell (SIGC) through the high-harmonic generation (HHG) process. We demonstrate nonlinear double ionization of Ar and Ne using ∼40 eV photons and provide insight on how these studies can be extended to studying multi-electron dynamics in molecules.

High harmonics were produced in the SIGC using the setup described in Chapter 2 at the Advanced Laser Light Source in Varennes, QC. The reason we choose the SIGC as our HHG source is twofold: a) it provides our brightest source of XUV photons and, b) we can tune the efficiency of generated harmonics by adjusting the pressure in the cell as well as the position of the laser focus of the fundamental beam. Emitted high harmonics were then focused onto a gas target in a time-of-flight (TOF) mass spectrometer (MS) (see Fig. 6.2) by a custom made multilayer dielectric spherical mirror with focal length $f = 250$ mm. The dielectric material and thicknesses of the layers were chosen such that the mirror has a maximum reflection efficiency for a photon energy of ∼40 eV. The mirror was calibrated by our collaborators at the Lawrence Berkeley National Laboratory using a synchrotron source. It has a maximum reflection value of ∼0.42 and a bandwidth with full width at half maximum approaching 3 eV. Fig. 6.1 shows the normalized harmonic spectra generated in the SIGC along with the reflection coefficient of the dielectric mirror.

The harmonic signal was tuned such that the 25^{th} ($E = 38.75$ eV) and 27^{th} ($E = 41.85$ eV) harmonics of the 800 nm fundamental laser have the highest conversion efficiency. The reflection reaches a maximum of ∼3 % for all other photon energies present in the XUV beam. At the beginning of each ionization experiment, the harmonic spectra was measured and recorded so that no significant changes to the spectra were present. Because of the high stability of both the pressure in the gas cell and the fundamental 800 nm beam, we were able to keep the XUV beam consistent throughout the data collection process.

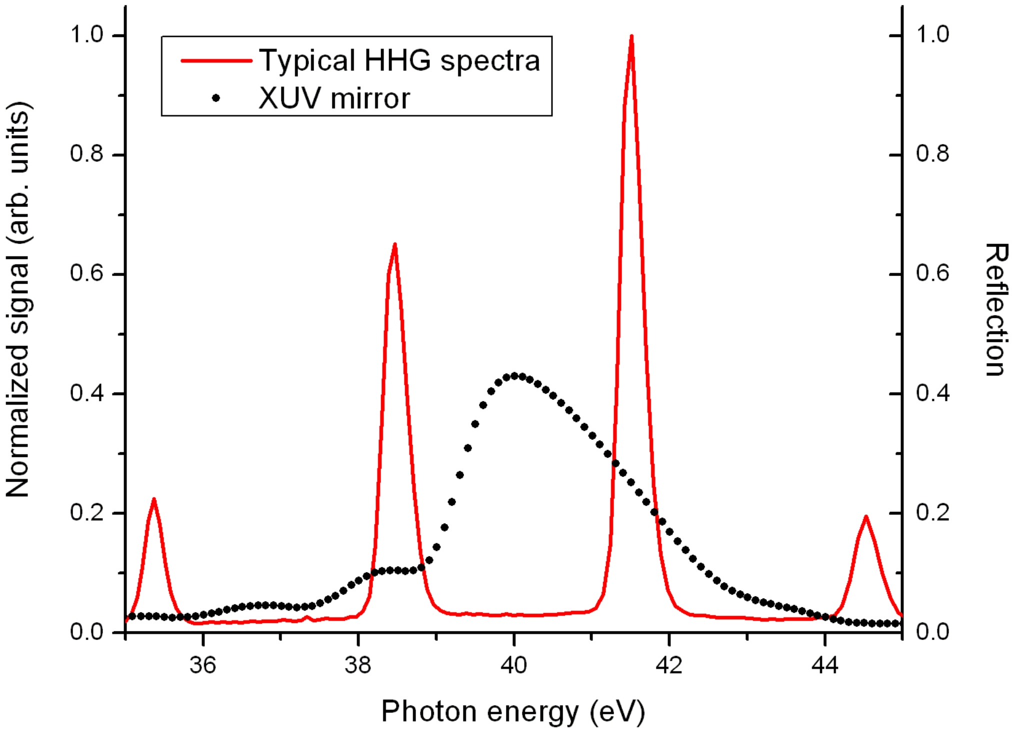

Figure 6.1: The normalized high harmonic spectra produced in the SIGC superimposed onto the reflection efficiency of the multilayer dielectric spherical mirror.

The fundamental beam and lower harmonic signal ($\hbar\omega < \sim 15$ eV) were blocked by using an aluminum filter of thickness 150 μm (purchased from Lebow). The aluminum filter's transmission only approaches a maximum of ∼ 75% for photons in the range of 17-70 eV which further diminishes the useable photons for ionization. However, it does a tremendous job of rejecting the fundamental beam. The filter was first tested for effectiveness by cutting off the gas pressure in the gas cell so that no harmonics would be produced. The absense of ionization signal in the TOF system indicated that there was no fundamental beam leaking through the filter. The effectiveness of the aluminum filter was also carefully monitored throughout the experiments by measuring the ionization rates of a low-abundance isotope of Argon at different times during the data collection. The signal from this isotope was steady but never saturated. Any deficiency in the filter that would allow the fundamental to leak through would increase the ionization signal.

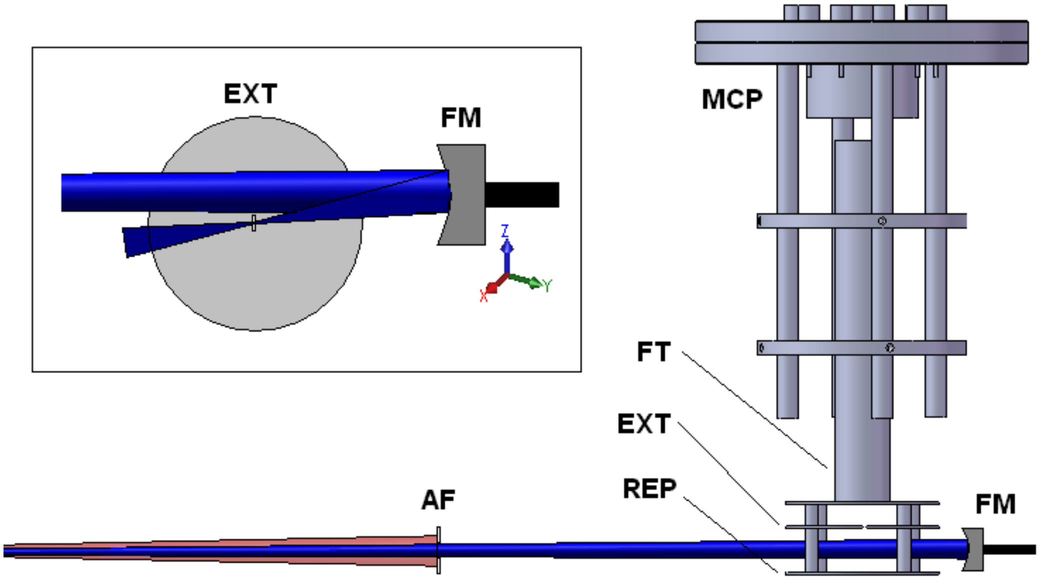

Figure 6.2: Schematic of the time-of-flight mass spectrometer. AF: aluminum filter; REP: repeller plate; EXT: extractor plate; FT: flight tube; FM: focusing mirror; MCP: microchannel plate detector. The inset shows the off-axis geometry when using the XUV beam for ionization.

We use a home-built TOFMS to observe the ions created in the experiment. A schematic of our experimental system is shown in Fig. 6.2. We use a Wiley-McClaren setup to extract ions from the interaction region which are sent down a field-free flight tube towards a microchannel plate detector (MCP). The detector is biased to post-accelerate the incident ions and sends out a voltage to a time digitizer for every ion occurence. The digitizer is coupled to a computer which records each incident ion in the software and creates the mass spectrum based on the MCP signal and a trigger from the laser source. The time that the ions hit the detector is converted into a mass to charge (m/z) with a quadratic dependence. A calibration of the mass spectrum is done using known ions such as H_2O^+, O_2^+, and N_2^+ along with their typical calculated flight times.

Ionization in the TOFMS occurs between the repeller and extractor electrodes. The electric field used in the first acceleration stage was 2000 V/cm and a field of 1100 V/cm was used in the second stage. A 1 mm × 9 mm slit in the center of the extractor plate allows the passage of ions towards the detector. The geometry of the TOF is off-axis (as shown in the inset of Fig. 6.2) so that ions created by single photon ionization from the unfocused harmonic beam will not be delivered to the detector as the beam passes the slit in the extractor plate. The multilayer mirror is mounted on an XYZ translation manipulator in order to adjust the focus of the beam so it is at an optimal position for maximum ion collection efficiency.

Fig. 6.3 shows a typical TOF ion spectrum of Argon under illumination by the focused XUV beam in units of m/z. The appearance of the first charge state results from the absorption of a single XUV photon. The formation of Ar^{2+} requires an appearance energy of ∼43 eV, a value which has been known since the early days of electron impact ionization [81]. The 2+ charge state can result from two different mechanisms. First, the Ar atom can directly absorb two XUV photons of ∼40 eV to end up in the doubly charged state. The second pathway would be a sequential ionization where the atom first absorbs one photon thereby releasing an electron and creating an ion. The ion subsequently absorbs a second photon which has enough energy (∼29 eV) to remove a second electron from the system, sending it to the 2+ state. The appearance of Ar^{2+} should have contributions from both nonlinear mechanisms. A method to determine which mechanism dominates would be to study the emitted photoelectron spectrum which we plan to carry out at a later date. Instead, we observed the intensity dependence of the Ar^{2+} signal. The slope of this logarithmic plot gives the order of the process. We vary the intensity of the XUV beam by changing the fundamental beam energy while keeping the pressure in the gas cell constant.

Fig. 6.4 shows the results of the double ionization experiment of Argon using the XUV photons. Since it is difficult to measure the XUV photon energy to estimate beam intensity, we plot the Ar^{2+} signal as a function of Ar^+ as the singly charged ion signal is a

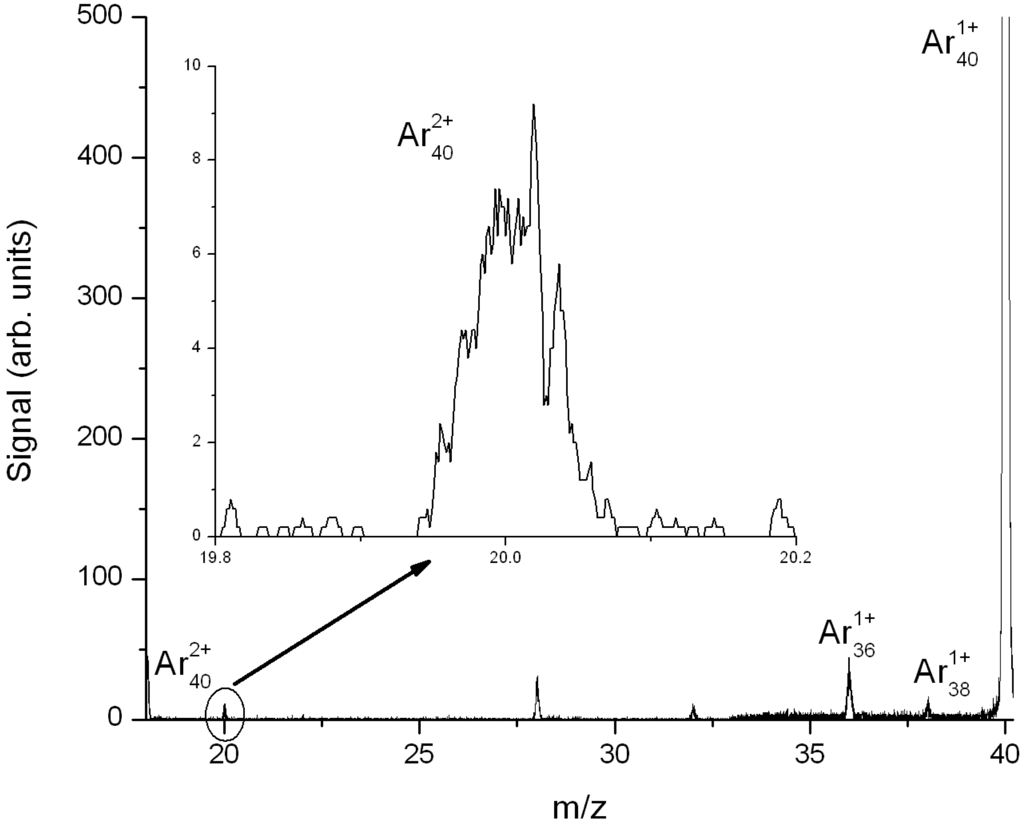

Figure 6.3: A sample time-of-flight ion spectrum of Argon under illumination by a focused XUV beam in units of m/z.

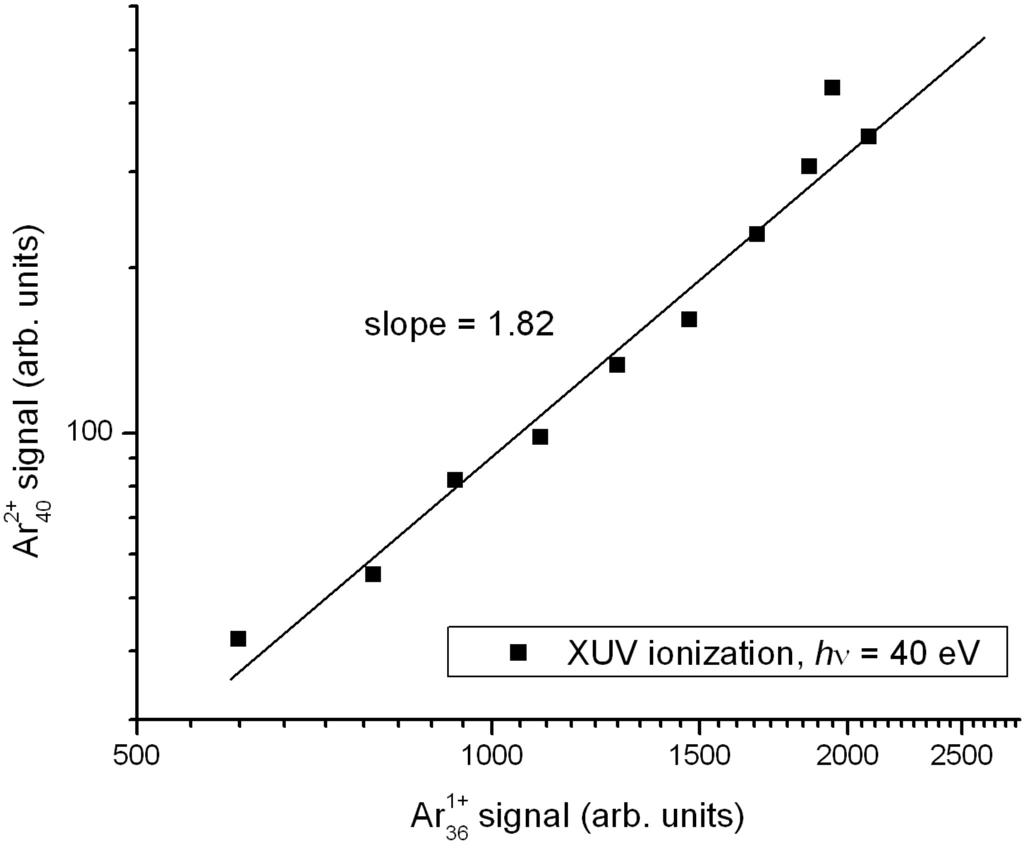

Figure 6.4: Log plot of the doubly charged Ar yield as a function of the singly charged Ar yield. The singly charged yield is directly proportional to the XUV beam intensity.

1-photon process and would be proportional to the XUV intensity. The figure shows the log-log plot of the Ar^{2+} signal of the mass-40 isotope vs. the Ar^{+} signal of the mass-36 isotope. The mass-36 isotope has an overall abundance of only 0.33% and its signal was unsaturated at the highest harmonic intensity. The slope of the log-plot is 1.8 ± 0.2 which shows the process to have a 2-photon nature.

Using the same harmonic beam, the double ionization of Ne was also obtained. The appearance energy of Ne^{2+} is slightly above 62 eV. A log plot of the Ne^{2+} signal against an unsaturated isotope of Ne^{+} also yields a slope with value close to 2.

We give a rough estimation of $\sim 10^{12}$ W/cm^2 as the intensity of the XUV beam. This value is based on an estimated spot size. We continue our efforts to determine the experimental focused spot size through a series of knife-edge measurements in conjunction with an XUV photodiode.

The results on nonlinear ionization of Ar and Ne puts us in a position to try similar experiments of this nature in molecules in order to study multi-electron dynamics. Transient absorption spectroscopy using fs XUV pulses has recently proven capable of probing dissociation dynamics in polyatomic molecules such as vinyl bromide [82]. The use of attosecond XUV pulses for this type of experiment will enhance both spatial and temporal resolution and also provide insight on the multi-electron dynamics at work. We also continue to improve the experimental technique by increasing the XUV flux using various methods such as quasi-phase matching in a modified gas cell as well as different ionization schemes involving multiple fundamental fields.

6.2 Ionization and fragmentation of C_{60} with few-cycle laser pulses

Collective electronic dynamics influence a variety of processes in nature including superconductivity and ferromagnetism in physics, electron transfer rates in chemistry, energy conversion and signal transport in biology, and it also enables new technologies such as nanophotonics [83] and nanoplasmonics [84]. Electronic motion occurs on the attosecond timescale and direct study of such ultrafast processes, while possible with the use of attosecond technology, is still in its infancy. However, it is possible to extract signatures of collective and correlated multi-electron dynamics in molecules by studying laser-induced processes where electrons play a key role such as ionization and fragmentation or high harmonic generation. C_{60} is of particular interest for these types of studies due to its high degree of symmetry which simplifies the ability to model its geometry [85], as well as its large number of delocalized valence electrons. Significant experimental [86] and theoretical [87, 88] work has been conducted on ionization and fragmentation dynamics in C_{60} and recent calculations on multi-electron effects in ultrafast ionization of C_{60} [89] confirms a continued interest in this molecule. It has also been shown that C_{60} is an effective source for high harmonic generation and multi-electron dynamics play an important role in harmonic enhancement [90].

The present study investigates the effects of various laser parameters such as pulse duration and ellipticity in the ionization and fragmentation dynamics of C_{60} towards efficiently generating high molecular charge states and extracting indications of multi-electron dynamics at play. Our results build on the work of Bhardwaj *et al.* [91, 92] which looked at how a laser-induced dipole force influenced the excitation of the C_{60} molecule as well as the role of recollision during ionization in the strong laser field. Those experiments were conducted with multi-cycle near- to mid-infrared pulses ($\lambda = 0.8$–2.2 μm). The use of longer wavelengths was important as ionization became adiabatic and high charge states were produced (up to C_{60}^{12+}) with fragmentation being almost nonexistant. Alternatively, one can use few-cycle pulses at optical wavelengths to minimize the coupling of energy into the nuclear degrees of freedom which also minimizes fragmentation [93, 91].

A Wiley-Mclaren time-of-flight mass spectrometer (TOFMS) [1] was used to collect ion signal during the ionization and fragmentation of C_{60}. Ion collection from the TOFMS is described in section 6.1. Experiments were carried out at the Advanced Laser Light Source in Varennes, QC using the 1 kHz beamline to generate 780 nm pulses with durations between 6 and 100 fs. To create the few-cycle beam, the 25 fs pulses from the compressor are first shaped by an acousto-optic programmable dispersive filter (Dazzler,

---

[1] The complete design, fabrication, and testing of the time-of-flight mass spectrometer was carried out by the author as part of the current Ph. D. project.

Fastlite [94]) then spectrally broadened by self phase modulation in a Argon-filled hollow core fiber. A typical broadband spectrum used to generate few-cycle pulses centered at 780 nm is shown in Fig. 6.5. The beam is then compressed by reflection off five sets of chirped mirrors and propagation through a few mm of fused silica [95]. We were able to compress the pulse down to 6 fs using this method. The temporal characterization of the pulse was performed using an interferometric autocorrelator (Femtolasers). To change the polarization of the few-cycle pulse, we used a broadband quarter-wave-plate (λ = 400 - 1200 nm). The intensity calibration at all pulse durations was done using the method of Hankin *et al.* [96] with the saturation intensity measured using the TOFMS. The TOFMS was also used to optimize the pulse duration of the few-cycle laser pulse.

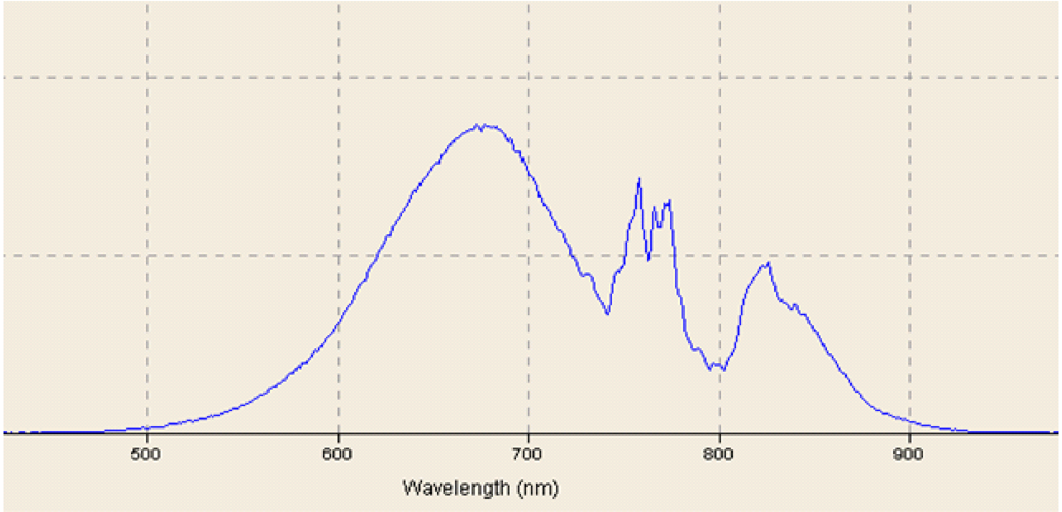

Figure 6.5: An example of a typical spectrum, centered at 780 nm, spectrally broadened in an Argon-filled hollow core fiber by self phase modulation. This spectrum is used to generate few-cycle 6 fs pulses.

Fig. 6.6 shows a typical mass spectrum of C_{60} ionized by a linearly polarized, 6 fs, 780 nm beam at an intensity of 0.8×10^{14} W/cm^2. Fragmentation using the few-cycle pulse is very low compared to a 40 fs multi-cycle pulse [92] and we can clearly see the C_{60}^{7+} ion charge state at a value of m/z = 102.86. The peak at m/z = 90 could correspond to either the C_{60}^{8+} ion charge state or the C_{15}^{2+} fragment charge state. Since we cannot see clear isotopes in the mass spectra at m/z = 90, it is not possible to confirm that the ion charge state is present. To the best of our knowledge, the C_{60}^{7+} ion charge state is presently the highest recorded charge state for C_{60} at optical wavelengths and is not present in mass spectra generated using multicycle laser pulses. It is thus worth investigating the effect of pulse duration on ionization and fragmentation of C_{60} at optical wavelengths.

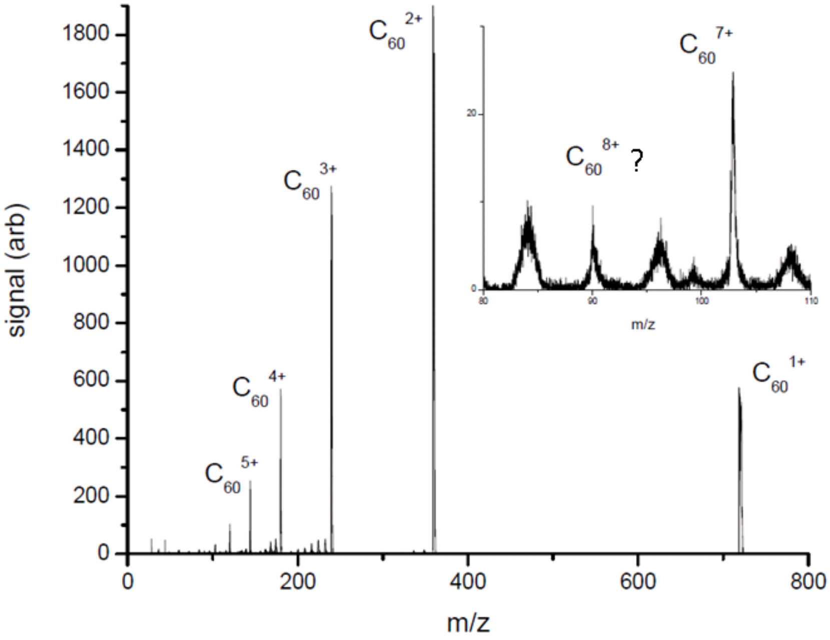

Figure 6.6: This is a sample mass spectrum of C_{60} ionized by a 6 fs, 780 nm beam at an intensity of 0.8×10^{14} W/cm^2.

Keeping the laser intensity constant, we vary the pulse duration, τ, of the linearly polarized 780 nm beam from 6 to 100 fs. For τ = 6-9 fs, we used the compression scheme described above to generate transform-limited pulses. The Dazzler was used to shape and temporally broaden the pulses for τ = 20-100 fs. The same beam path was used for these multi-cycle pulses and the hollow core fiber was filled with Helium to suppress any self phase modulation. The maximum charge state attainable in C_{60} as a function of τ is shown in Fig. 6.7a while the 3D contour plot (Fig. 6.7b) shows the variation on number of charge states. Pulse durations of 6 and 9 fs were capable of generating C_{60}^{7+} ions while we see a steady decrease of high ion charge states as τ increases. We attribute this result to lower molecular stability during ionization for multicycle pulses which leads to higher rates of fragmentation. This is because longer pulse durations enable the coupling of laser energy into both nuclear as well as electronic degrees of freedom.

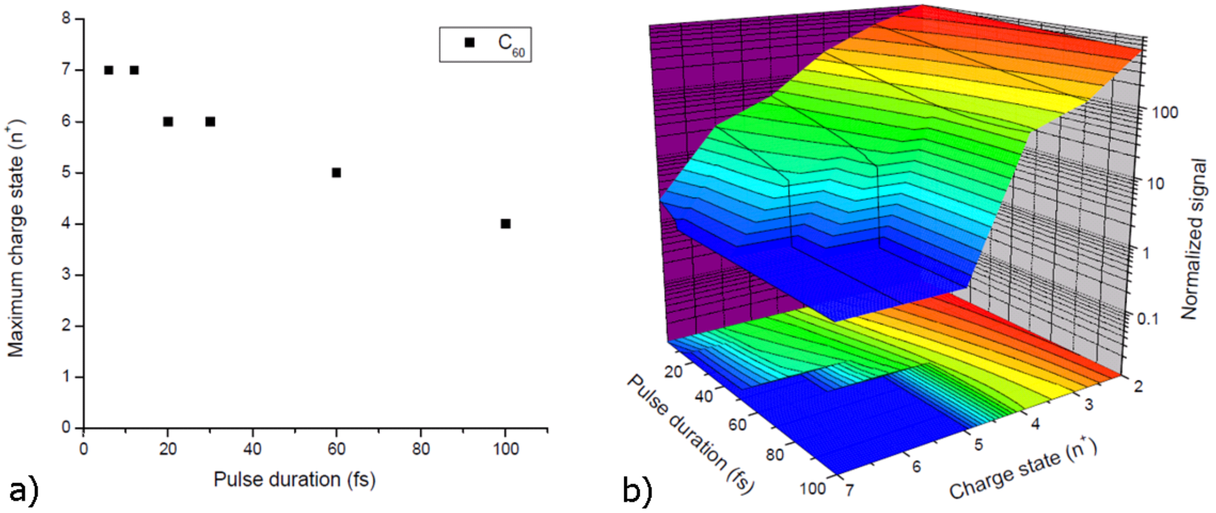

Figure 6.7: a) 2D and b) 3D contour plot of the maximum number of charge states in C_{60} as a function of laser pulse duration, τ, using linearly polarized, 780 nm light at an intensity of $\sim 2\times10^{14}$ W/cm^2.

Fig. 6.8 shows the dependence of the total number of intact fragments (black squares) as well as the total number of fragments with ejected carbon clusters (red circles) as a function of τ using linearly polarized, 780 nm light at an intensity of $\sim 2\times10^{14}$ W/cm^2. We see an almost linear increase for both plots as pulse duration increases which demonstrates the effectiveness of the few-cycle pulse at minimizing fragmentation.

However, an inherent limit arises as we consider the use of single cycle pulses for experiments. For linear polarization, two electrons would simultaneously need to occupy the molecule's potential barrier region thus causing a decline in ionization efficiency similar to a Coulomb blockade in solid-state physics [97, 98]. We therefore must consider the use of circular or elliptically polarized light when using few-cycle pulses. As mentioned in [92], recollision is the dominant ionization method for C_{60} in strong laser fields and it is well known that recollision decreases rapidly with increasing ellipticity in the laser polarization.

In Fig. 6.9 we examine how the molecular ion yield (6.9a) for both low (black squares)

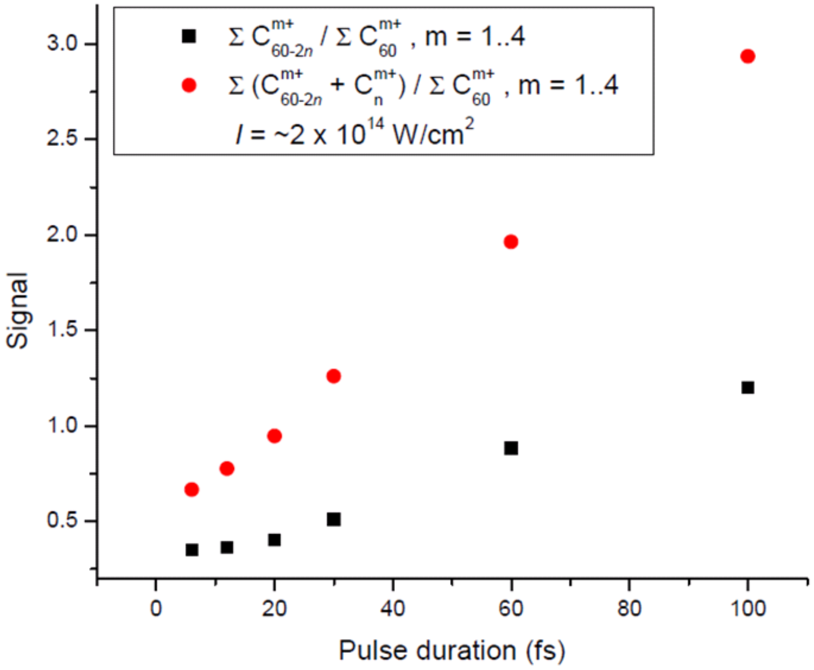

Figure 6.8: The total number of fragments of C_{60} (normalized to the total number of ions) as a function of laser pulse duration, τ, using linearly polarized, 780 nm light at an intensity of $\sim 2\times10^{14}$ W/cm^2.

and high (red circles) charge states as well as normalized fragment yield (6.9b) vary with laser ellipticity. We use a 780 nm, 6 fs pulse with an intensity of 0.8×10^{14} W/cm^2 and we vary the ellipticity from linear ($\epsilon = 0$) to circular ($\epsilon = 1$).

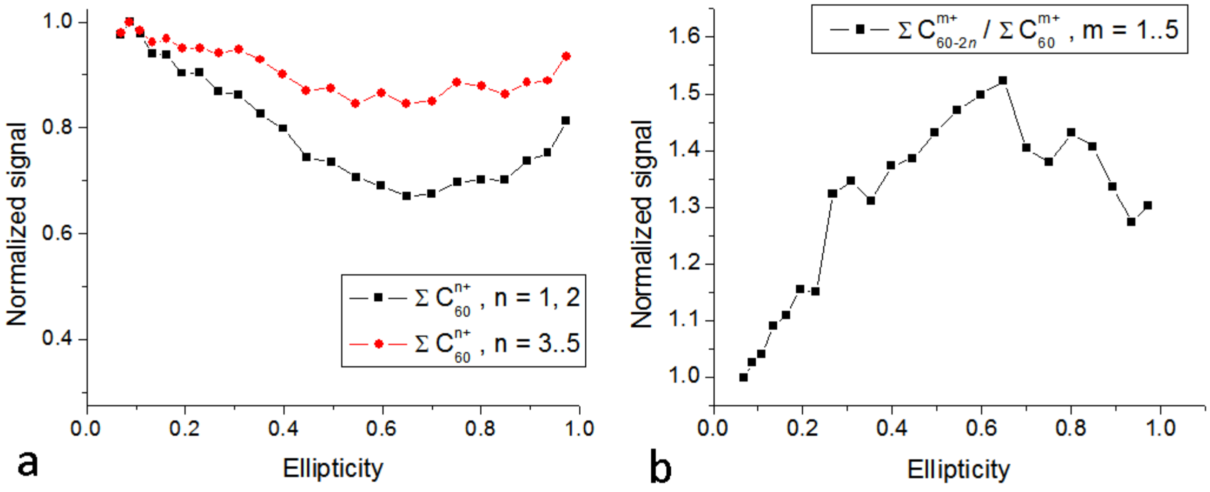

Figure 6.9: The a) molecular ion yields for low (black squares) and high (red circles) charge states and b) normalized fragment yield as a function of laser ellipticity, ϵ, using a 6 fs, 780 nm pulse at an intensity of 0.8×10^{14} W/cm^2.

The total number of low charge state ions decreases significantly as ellipticity is increased up to a value of $\epsilon = \sim 0.7$ at which point, the number of ions begins to rise. This signifies that another mechanism of ionization besides recollision starts to dominate at high ellipticity. However, although counterintuitive, recollision could still play a role as theoretical evidence of recollision using circularly polarized light has been reported [99]. For higher charge states of C_{60}(from 3+ to 5+), the ellipticity dependence is much weaker thus the production of high charge states is still quite feasible using the few-cycle pulse. Panel b) of Fig. 6.9 shows that the total fragmentation, normalized to the total number of ions, increases with laser ellipticity. At $\epsilon = \sim 0.7$ where we have a minimum in low charge state production, there is a maximum in fragmentation. This relationship between ionization and fragmentation should be much less evident through use of longer wavelengths as shown in [92].

While the total number of ions decreases with increasing ellipticity, an interesting result for the high charges states (normalized to the C_{60}^{1+} signal) occurs (Fig. 6.10). Each subsequent charge state, C_{60}^{q+}, increases faster than the previous one for $q = 2$–6, all with maximum value at $\epsilon = \sim 0.7$, the ellipticity at which point the total ion signal is lowest. We emphasize the key point that we can most efficiently generate high charge states in C_{60} using nearly circularly polarized light.

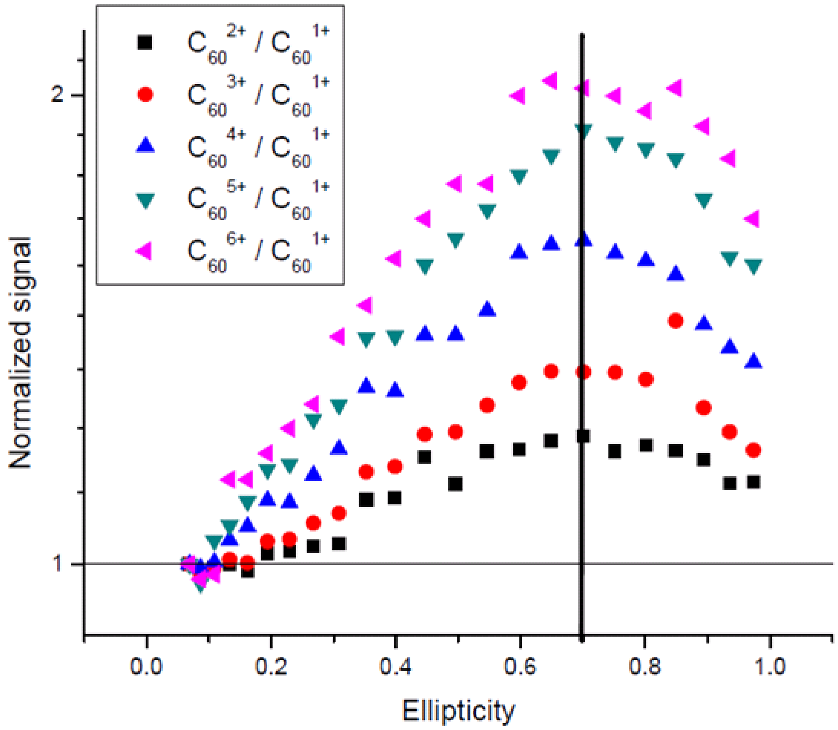

Figure 6.10: The number of high charge states of C_{60} as a function of laser ellipticity, ϵ, using a 6 fs, 780 nm pulse at an intensity of 0.8×10^{14} W/cm^2.

To complement these results, we examine how laser intensity affects the production of high charge states and fragments for the few-cycle pulse using both linear and circularly polarized light. We compare the normalized molecular ion charge states of C_{60} for a ratio of linear to circularly polarized light as a function of laser intensity using a 6 fs, 780 nm pulse (Fig. 6.11). It is important to note that the signal for circular polarization has been shifted down by $\sim 0.6\times10^{14}$ W/cm^2 in order to equalize the ionization rates for both polarizations since the electric field strength of circular polarization is $\sqrt{2}$ higher than linear for the same beam energy. We see a clear domination for circularly polarized light at low intensities and this is most significant for the higher charge states (4+ and 5+). As intensity is increased, the amount of charge states for both polarizations begin to even out but at this point, the molecule has reached ionization saturation.

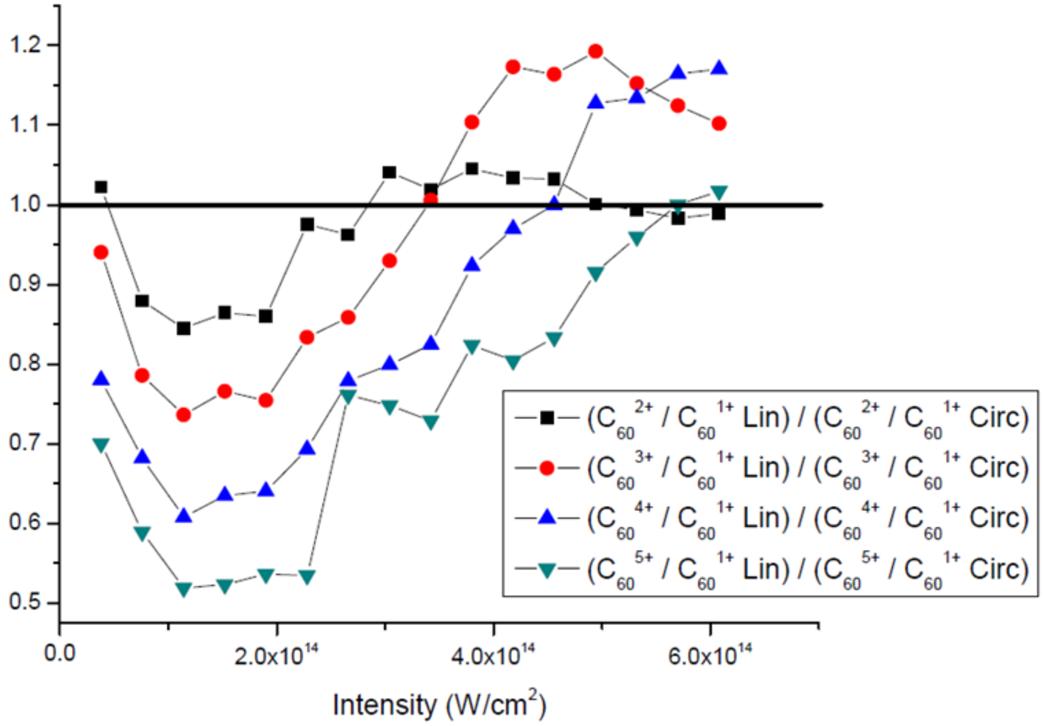

Figure 6.11: Normalized C_{60} charge state ratios for linear and cirularly polarized light as a function of intensity using a 6 fs, 780 nm pulse.

To get an idea of how energy is deposited into the molecule to induce higher charge states before fragmentation occurs, we examine the sum of all fragments produced as a function of intensity (normalized to the C_{60}^{1+} signal) for both linear and circularly polarized light (see Fig. 6.12). We see a slight decrease in fragmentation as intensity rises for both polarizations but the fragmentation signal remains relatively constant for a broad range with a slight pickup past $I = \sim 5\times10^{14}$ W/cm^2. It is evident that the few-cycle pulse can minimize fragmentation of the molecule even at high intensities which further confirms its efficiency in producing high molecular ion charge states in C_{60}.

We have demonstrated a clear advantage to generating a high number of ion charge

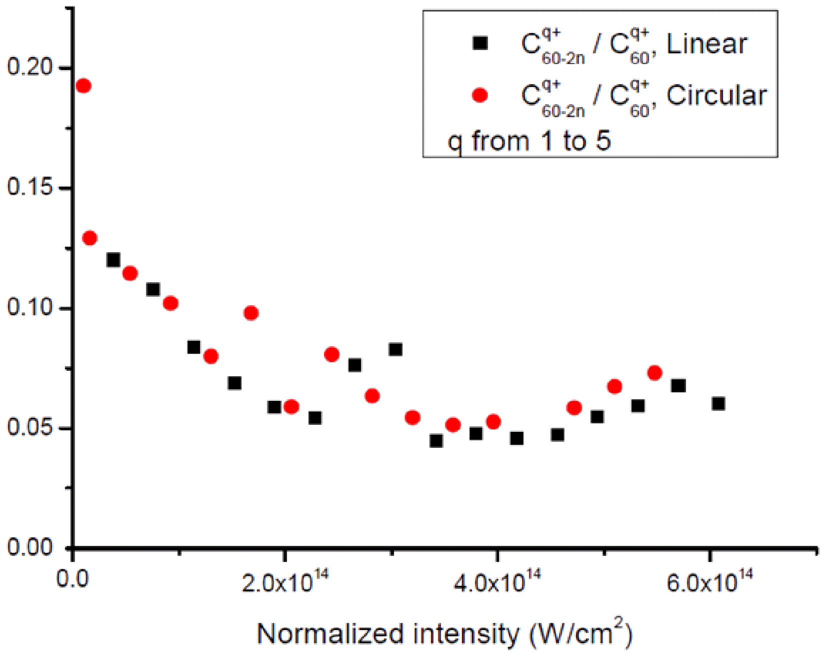

Figure 6.12: The sum of C_{60} fragments, C^{q+}_{60-2n}, as a function of intensity using a 6 fs, 780 nm pulse for both linear and circular polarization. Each number of fragments is normalized to the C^{1+}_{60} signal.

states in C_{60} using few-cycle pulses at a near-infrared wavelength. High charge states are more apparent when using elliptical and circularly polarized light compared to linear polarization. This could be due to the ellipticity of the laser field effectively bringing back electrons with large transverse spread upon ionization to recombine with parent ions. The influence of the ionic core could also play a role for higher charge states in bringing back electrons due to an increase in Coulomb focusing [100]. The next step is to use a few-cycle mid-infrared pulse (such as $\lambda = 1800$ nm) to study ionization and fragmentation. We expect to see higher charge states ($> C_{60}^{12+}$) [91] as well as even less fragmentation compared to 780 nm light and hope to approach the theoretical Coulomb limit of C_{60}^{16+}. In concurrence, we plan to study the interaction of XUV photons with energies of both 20 and 40 eV with C_{60} to excite the well known surface and volume plasmons [20]. To extract the measurement of multi-electron dynamics, we can directly measure the signal from ejected electrons using a velocity map imaging spectrometer which we are currently building.

Chapter 7

Conclusion and future outlook

The work conducted in this thesis is original research that has contributed to the new field of high harmonic spectroscopy (HHS), particularly in complex molecular systems. We have explored various topics in molecular physics and chemistry, such as electronic and isomeric effects, and shown how HHS can lead to new discoveries and conclusions surrounding these topics. The publications in this thesis serve to establish HHS as an easily accessible spectroscopic tool to study the dynamics of atoms, molecules, and electrons on the femtosecond and attosecond timescales with incredible ångström spatial resolution.

The contributions to the field are summarized in sections 7.1 and 7.2. Section 7.3 briefly describes some other experiments we are working towards.

7.1 Contributions to high harmonic generation efficiency

High harmonic generation (HHG) is a highly nonlinear process with typical conversion efficiencies on the order of the 10^{-5} to 10^{-7} range [57, 58] when using 800 nm light. A necessity for HHG to be considered a general spectroscopic tool is that it can be utilized to study a wide variety of samples. The conversion efficiency of HHG relies heavily on the density of the sample in the interaction region and for a traditional pulsed valve setup, achieving such densities can be a challenge. In Chapter 2, we explored the direct comparison between the use of both a finite (FGC) and semi-infinite gas cell (SIGC) to a pulsed valve as a generating medium for high-order harmonics and demonstrated over two orders of magnitude increase in conversion efficiency ($\sim 10^{-4}$) in our setup under optimal pressure and phase-matching conditions.

The publication also described an in-line monitoring system for measuring harmonic generation efficiency in the form of a simple copper parallel plate detector (PPD). The detector collected electrons from photoionization of the background gas in the chamber by the propagating extreme-ultraviolet photons (XUV) produced from HHG. While the PPD is not able to measure the absolute efficiency of the generated high-order harmonics, it can be used to complement various methods of measuring HHG flux such as the knife-edge technique [101] along with an XUV photodiode.

While the measurement of the absolute harmonic conversion efficiency is not a novel experiment, it requires a complicated setup and disruption of the vacuum system in the HHG chamber at ALLS. This experiment was attempted during the course of this Ph.D but too many problems arose which did not allow for any tangible results. However, some significant progress has been made towards building an HHG system to be used in-house at uOttawa (see Appendix A) that would be capable of interchanging between several high harmonic applications at the flip of a switch. Examples are HHS experiments, the measurement of high harmonic flux, and the interaction of the high harmonic beam and the fundamental beam onto a separate target.

We have also used the bright HHG source described in Chapter 2 to conduct some preliminary experiments on the interaction of high energy XUV photons and various gas targets. The results of these experiments are described in Chapter 6.

7.2 Contributions to molecular high harmonic spectroscopy

The focus of the thesis was to develop HHS as a general spectroscopic tool to study static and dynamic processes in atoms and molecules. HHS had previously been successful in probing atomic and simple molecular systems but the challenge was to extend HHS to study complex, polyatomic molecules. While there are a few notable causes for modulations of high harmonic spectra from atoms (eg. the Cooper minimum in Argon [52] or the giant resonance in Xe [102]), there are several other factors that can cause the modulation of high harmonic spectra from molecules such as the contribution of multiple molecular orbitals to ionization as well as multi-orbital effects during recombination. A suitable practice is to take what is known about HHG in atoms and extend that knowledge to molecules in order to find similar effects. In Chapters 3, 4, and 5, we developed a basis for investigating the influence of electronic and molecular structure from high harmonic spectra in complex, polyatomic molecules.

7.2.1 The Cooper minimum in molecules

A well-known example of a modulation in high harmonic spectra is the Cooper minimum (CM) in Argon causing a noticeable local minimum [52]. The CM in the photoionization cross-sections is familiar in atoms but photoelectron spectroscopy has shown it to persist in some molecules containing atoms that display a radial node in their orbital [55]. In Chapter 3, we sought to use HHS to demonstrate this effect in a series of molecules containing either a chlorine (Cl) or sulfur (S) atom as the minimum should appear as a strong modulation in the high harmonic spectra. It was unknown whether HHS was capable of studying such a phenomenon in molecules arising purely from electronic structure as other sources are known to also modulate high harmonic spectra.

Publication 5 provides the first experimental and theoretical high harmonic spectra which demonstrate a CM to appear in the molecules CS_2 and CCl_4, as well as other polyatomic molecules containing Cl. These results provide strong evidence to suggest that there exists a direct correlation between transition dipole matrix elements associated with HHG and photoionization. Furthermore, the results demonstrate that HHS can be used as a sensitive probe of the atomic character of molecular orbitals. We have shown that lone-pair-like molecular orbitals (MO) may exhibit CM in their high harmonic spectra and the position of the CM shifts as the character of the MO changes.

These results also show that to an extent, the HHG process is capable of extracting recombination cross-sections from molecules, similar to the atomic case [103]. Although this procedure is indeed complex, it would open up a new possibility to study ultrafast nuclear dynamics in complex molecules. In principle, the retrieved cross-sections should be independent of wavelength therefore the recollision time of the electron can be carefully controlled during the HHG process, resolved to a few tens of attoseconds.

A subsequent planned experiment is to produce and characterize HHG in aligned CS_2 which can easily be aligned since it is highly polarizable. Doing so would enable 1) to investigate amplitude minima in the HHG spectra caused by the CM as well as structural interference due to multi-centre recombination and 2) progress towards extracting recombination dipoles matrix elements from HHG spectra in a polyatomic molecule and test the validity of new theoretical tools being developed.

7.2.2 Symmetry in molecular and electronic structure

The influence of symmetry in both electronic and molecular structure on high harmonic spectra can be studied in several ways. In Chapter 4, we investigated how the presence of nodal planes in MO's would influence harmonic spectra in first a simple test molecule, H_2O, and then a series of complex polyatomic chloromethane molecules: CH_2Cl_2, $CHCl_3$, and CCl_4. At the time of publication, most experimental and theoretical studies on HHG in molecules had been typically conducted in simple linear molecules such as N_2, O_2, and CO_2 that were aligned in a laser field. However, the wealth of information from signatures of electronic structure from HHG experiments on polyatomic molecules was high, but these molecules were difficult to align and this made the extraction of meaningful information difficult.

The results we show in Chapter 4 demonstrate, for the first time, that it was feasible to extract electronic structure information from a randomly oriented, complex polyatomic molecule. In H_2O as well as all three chloromethanes, we see significant extension of the high-harmonic cut-off compared to an atom with similar ionization potential, Xe. The extension of the cut-off is mainly due to suppression of ionization which occurs when the MO in which ionization takes place contains one or more nodal planes [46]. Quantum destructive interference occurs as an electron wavepacket is emitted from either side of the nodal plane. The first three orbitals of H_2O are perfect *p*-type orbitals while the highest occupied molecular orbital (HOMO) of each chloromethane contains one or more nodal planes.

A second manifestation of suppressed ionization was seen in CCl_4 as a local minimum at linear polarization in the ellipticity dependence of the driving field on the HHG process. As both the HOMO, as well as the molecular structure of CCl_4, is highly symmetric, there is a slight suppression of ionization for linear polarization due to quantum interference during ionization which was shown to be offset by the small transverse field component at a slight ellipticity. This effect was previously shown in the recollision signal of the C_6H_6 molecule [45].

Another significant result from Publication 3 was the evidence of interference during recombination due to multiple nuclear centers. In simple aligned molecules, molecular structure has been shown to cause interferences in the HHG spectra during the recombination process [50]. We used a similar model to describe destructive interference from three atomic centers in $CHCl_3$ which suggested that the angle-dependent ionization process preferentially selects a specific orientation even in randomly oriented molecules. A similar interference for three centers was also modeled by Lein *et al.* [104].

The experiments described in Chapter 4 on molecules that display signatures of molecular and electronic structure open up a wide avenue of possibilities for selective probing of complex systems using HHS, such as investigating the contribution to strong-field processes from specific MO's. In fact, there has been recent interest in the study of strong-field ionization of H_2O and theoretical results seem to indicate the distinct separation of ionization from the first two molecular orbitals [105].

7.2.3 HHS of molecular isomers

In order to further explore the role of molecular structure on the HHG process, we also carried out experiments on a set of molecular stereo- and structural isomers and these results are described in Chapter 5. There already exist several techniques to identify molecular isomers by their ro-vibrational spectra or using electron scattering techniques [106]. However, HHS would be an ideal tool to study isomeric effects in molecules due to the high spatial and temporal resolutions available. In publication 4, we showed that high harmonic spectra from randomly oriented *cis-trans* stereoisomers of 1,2-dichloroethylene and 2-butene generated at similar wavelength, intensity, and gas pressures, showed immense differences in both harmonic amplitude and cut-off. The differences were mainly attributed to the first step of the HHG process, ionization by the strong laser field, and were confirmed by calculations of angle-dependent ionization yields. Publication 6 uses further experimental and numerical results to extend this study to structural isomers, such as butane and propanol, in order to use HHS to probe the contribution to ionization from multiple molecular orbitals in unaligned, polyatomic molecules.

The results from Chapter 5 show for the first time that HHS is capable of probing molecular isomers of randomly oriented complex molecules and that the harmonic spectra from those isomers are distinguishable. The differences in HHG spectra are extremely apparent for *cis-trans* type stereoisomers while much less so for structural isomers. The fact that HHS can distinguish between molecular isomers opens up the path towards ultrafast time-resolved measurements of isomerization dynamics with femtosecond to attosecond temporal resolution. These types of dynamics are especially important in biology where most forms of biological molecules (macromolecules) such as proteins and nucleic acids have isomers or demonstrate chirality [107]. This opens up a variety of experiments towards the investigation of ultrafast processes such as charge transfers in large, complex systems [108].

7.3 Further studies in HHS of complex molecules

We have always had a significant interest in generating high harmonics in the C_{60} molecule and have had some success in the past (see publications 7 and 8) using the plasma harmonic method (see, for example, [109]). However, generating high harmonics from a C_{60} plasma plume can lead to inconsistencies such as whether HHG from C_{60} ions contributes to the total signal. HHG experiments in C_{60} are of particular interest due to the high number of delocalized electrons in the molecule and there have also been several theoretical studies on this topic [110, 111]. We have made steps towards the generation of high harmonics from single C_{60} molecules in gas phase and we continue these experiments to-date. Since the HHG process begins with ionization, we've also taken significant effort to study ionization of C_{60} using ultrafast laser pulses at different wavelengths ($\lambda = 800 - 1800$ nm). Further details of these ionization experiments can be seen in Chapter 6.

We have recently conducted some HHG experiments in 1,3 and 1,4-cyclohexadiene (CHD) molecules using few-cycle pulses at wavelengths of $\lambda = 1400 - 1800$ nm. Our results suggest evidence of distinct local minima in the HHG spectra from 1,4-CHD that is weakly intensity and wavelength dependent. This suggests that the source of the minimum arises from destructive interference between HHG contributions from different molecular orbitals. A manuscript on this topic is in preparation for publication in the near future (see Publication 9).

As shown in publication 4, the high harmonic spectra of the two enantiomers of the chiral molecule, propylene oxide, are indistinguishable when using linearly polarized light. Chiral molecules are normally identified by means of circular dichroism (CD) in linear absorption, which arises from differential absorption of left and right handed circularly polarized light. Absorption cross-sections for left and right handed circularly polarized light differ by less than one part per thousand due to the small size of most molecules relative to the wavelength of light. As a result, CD effects are relatively weak and therefore difficult to measure. It is a well known fact that HHG signal decreases significantly as ellipticity in the electric field of the driving pulse is increased. However, HHG signal is still relevant at small ellipticities ($\epsilon < 0.1$). We have measured the ellipticity dependence of HHG for the two enantiomers of propylene oxide using $\lambda = 1800$ nm light and we demonstrate elliptical dichroism with sensitivities on the same order as CD. These results, in collaboration with results from the CELIA group in France, have been submitted to the journal Nature for publication in September, 2014 (see Publication 10).

While the fields of attosecond science and high harmonic spectroscopy are only about a decade old, significant resources are being committed to the development of these topics today. Eventually, time-resolved HHS will enable us the ability to study specific electronic processes on the attosecond timescale. It is the hope of the author that the research conducted during this Ph.D project is of interest to those researchers currently expanding the field today, and will help develop some ideas for the new scientists who will progress the field tomorrow.

Appendix A

HHG system for Ultrafast Photonics Group

We have begun the assembly of our High Harmonic Generation (HHG) system to be used in the Ultrafast Photonics Group at the University of Ottawa. The full system is composed of three parts: 1) Source chamber, 2) Detection chamber, and 3) Interaction chamber. High harmonics will be generated in a semi-infinite gas cell (SIGC) in the source chamber. The detection chamber will contain an extreme-ultraviolet (XUV) spectrometer for diagnostics of the harmonics. Finally, an interaction chamber having either a time-of-flight mass spectrometer (TOFMS) or a velocity map imaging (VMI) spectrometer will be attached to the system to study interactions between the XUV pulses and atoms and molecules. The following sections will describe the three parts of this new system.

A.1 Source chamber

The source chamber is a custom spherical chamber made of stainless steel designed by the author and V. R. Bhardwaj and built by the Kurt. J. Lesker Company. A full schematic of the chamber is shown in Fig. A.1. The chamber has a spherical top with multiple conflat (CF) flanges around its shell and a large half nipple on the bottom to attach the turbomolecular pump. There are three 8" CF flanges on three sides and one

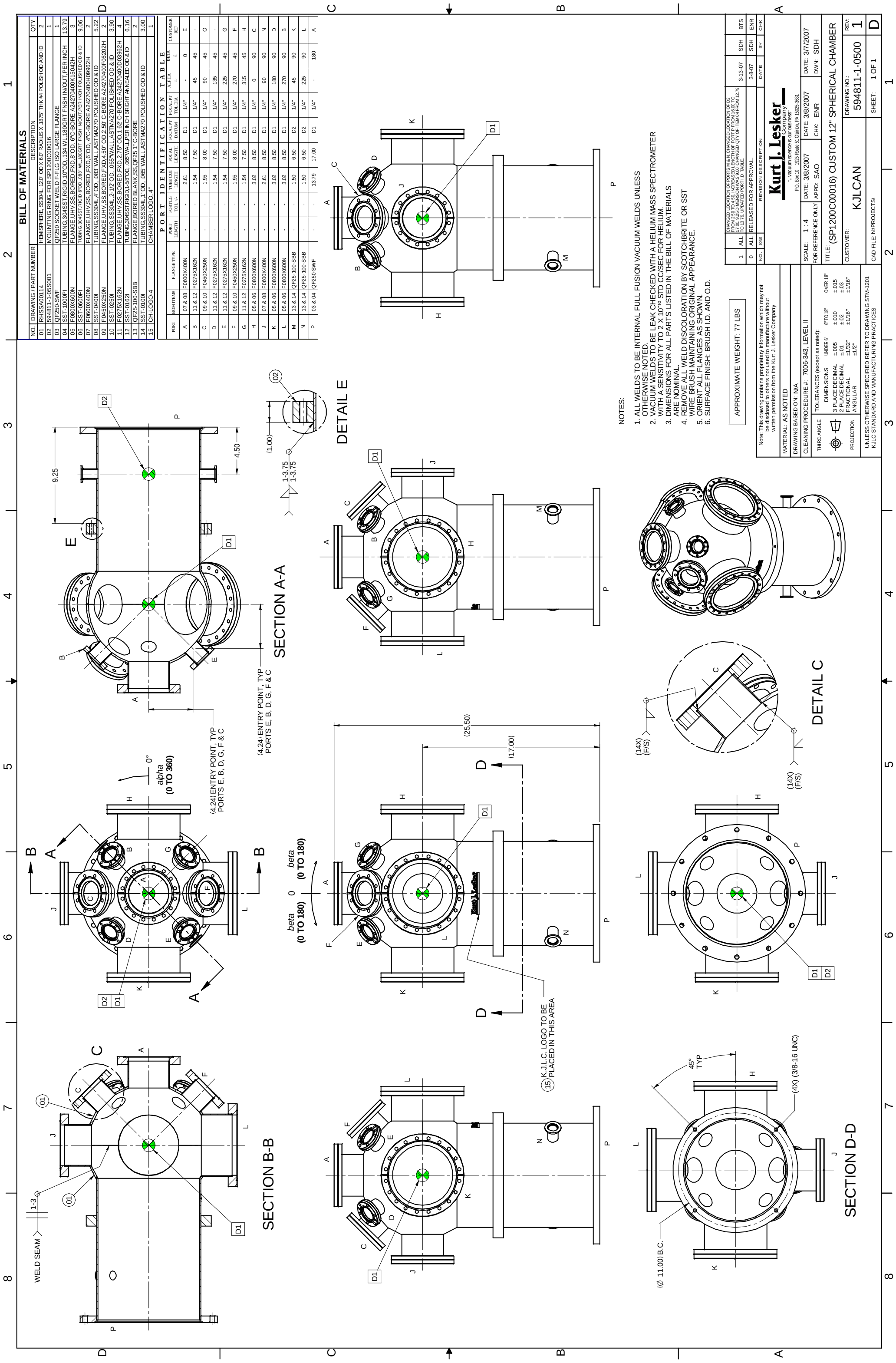

BILL OF MATERIALS

NO.	DRAWING / PART NUMBER	DESCRIPTION	QTY
01	RHSSA00114	HEMISPHERE, SS304L, 12.0" OD X 6.0" RADIUS X .1875" THK #4 POLISH OD AND ID	2
02	594811-1-05S001	MOUNTING RING FOR SP1200C00016	1
03	QF250-SWF	QF250 SOCKET WELD F-FLG ISO LARGE FLANGE	1
04	SST-1000PI	TUBING,304SST,RIGID,10"OD,.134 WL,180GRT FNSH IN/OUT,PER INCH	13.79
05	F0800X600N	FLANGE,UHV,SS,BORED,FXD,8"OD, 6"C-BORE A24270400K15042H	3
06	SST-0600PI	TUBING,304SST,RIGID,6"OD,.083" WL,180GRT FNSH IN/OUT,PER INCH POLISHED OD & ID	9.06
07	F0600X400N	FLANGE,UHV,SS,BORED,FXD,6"OD, 4"C-BORE A24270400H09962H	2
08	SST-0400I	TUBING,SS304L,4"OD, .083"WALL,ASTMA270 POLISHED OD & ID	5.22
09	F0450X250N	FLANGE,UHV,SS,BORED,FXD,4.50" OD,2.50"C-BORE A24270400F06202H	2
10	SST-0250I	TUBING,SS304L,2-1/2"OD, .065"WALL,ASTMA270 POLISHED OD & ID	3.90
11	F0275X162N	FLANGE,UHV,SS,BORED,FXD,2.75" OD,1.62"C-BORE A24270400D03962H	4
12	SST-0162I	TUBING,304SST,RIGID,1-5/8"OD, .065"WALL,PER INCH BRIGHT ANNEALED OD & ID	6.16
13	QF25-100-SBB	FLANGE,BORED BLANK,SS,QF25 1" C-BORE	2
14	SST-0100I	TUBING,SS304L,1"OD, .065"WALL,ASTMA270 POLISHED OD & ID	3.00
15	CH-LOGO-4	CHAMBER LOGO, 4"	1

PORT IDENTIFICATION TABLE

PORT	BOM ITEM#	FLANGE TYPE	PORT LENGTH	PORT LG TOL +/-	TUBE CUT LENGTH	FOCAL LENGTH	FOCAL PT DATUM	FOCAL PT TOL DIA	ALPHA α	BETA β	CUSTOMER REF
A	07 & 08	F0600X400N	-	-	2.61	8.50	D1	1/4"	-	0	E
B	11 & 12	F0275X162N	-	-	1.54	7.50	D1	1/4"	45	45	-
C	09 & 10	F0450X250N	-	-	1.95	8.00	D1	1/4"	90	45	O
D	11 & 12	F0275X162N	-	-	1.54	7.50	D1	1/4"	135	45	-
E	11 & 12	F0275X162N	-	-	1.54	7.50	D1	1/4"	225	45	G
F	09 & 10	F0450X250N	-	-	1.95	8.00	D1	1/4"	270	45	F
G	11 & 12	F0275X162N	-	-	1.54	7.50	D1	1/4"	315	45	H
H	05 & 06	F0800X600N	-	-	3.02	8.50	D1	1/4"	0	90	C
J	07 & 08	F0600X400N	-	-	2.61	8.50	D1	1/4"	90	90	N
K	05 & 06	F0800X600N	-	-	3.02	8.50	D1	1/4"	180	90	D
L	05 & 06	F0800X600N	-	-	3.02	8.50	D1	1/4"	270	90	B
M	13 & 14	QF25-100-SBB	-	-	1.50	6.50	D2	1/4"	45	90	K
N	13 & 14	QF25-100-SBB	-	-	1.50	6.50	D2	1/4"	225	90	L
P	03 & 04	QF250-SWF	-	-	13.79	17.00	D1	1/4"	-	180	A

NOTES:

1. ALL WELDS TO BE INTERNAL FULL FUSION VACUUM WELDS UNLESS OTHERWISE NOTED.
2. VACUUM WELDS TO BE LEAK CHECKED WITH A HELIUM MASS SPECTROMETER WITH A SENSITIVITY TO 2×10^{-10} STD CC/SEC FOR HELIUM.
3. DIMENSIONS FOR ALL PARTS LISTED IN THE BILL OF MATERIALS ARE NOMINAL.
4. REMOVE ALL WELD DISCOLORATION BY SCOTCHBRITE OR SST WIRE BRUSH MAINTAINING ORIGINAL APPEARANCE.
5. ORIENT ALL FLANGES AS SHOWN.
6. SURFACE FINISH: BRUSH I.D. AND O.D.

APPROXIMATE WEIGHT: 77 LBS

NO.	ZONE	REVISION DESCRIPTION	DATE	BY	CHK
1	ALL	CHANGED LOCATION OF PORTS M & N. CHANGED LOCATION OF D2 FROM 2.50 TO 4.50. INCREASED LENGTH OF PORT P FROM 16.00 TO 17.00. 9.25 DIMENSION WAS 9.00. CHANGED QTY OF ITEM 04 FROM 12.79 TO 13.79. UPDATED PORT I.D. TABLE.	3-13-07	SDH	BTS
0	ALL	RELEASED FOR APPROVAL.	3-8-07	SDH	ENR

Note: This drawing contains proprietary information which may not be disclosed to others nor used to manufacture without written permission from the Kurt J. Lesker Company

MATERIAL: AS NOTED

DRAWING BASED ON: N/A

CLEANING PROCEDURE #: 7006-343, LEVEL II

THIRD ANGLE PROJECTION

TOLERANCES (except as noted):

DIMENSIONS	UNDER 6"	6" TO 18"	OVER 18"
3 PLACE DECIMAL	±.005	±.010	±.015
2 PLACE DECIMAL	±.01	±.02	±.03
FRACTIONAL	±1/32"	±1/16"	±1/16"
ANGULAR	±1/2°		

UNLESS OTHERWISE SPECIFIED REFER TO DRAWING STM-1201 KJLC STANDARD AND MANUFACTURING PRACTICES

Kurt J. Lesker Company
"...vacuum science is our business"
P.O. Box 10 1925 Route 51 Clairton, PA 15025-3681

SCALE: 1 : 4
FOR REFERENCE ONLY
DATE: 3/8/2007 APPD: SAO
DATE: 3/8/2007 CHK: ENR
DATE: 3/7/2007 DWN: SDH

TITLE: (SP1200C00016) CUSTOM 12" SPHERICAL CHAMBER

CUSTOMER: KJLCAN

DRAWING NO.: 594811-1-0500

REV: 1

CAD FILE: N:\PROJECTS\

SHEET: 1 OF 1

D

Figure A.1: The schematic of the HHG source chamber.

6” CF flange on the fourth side as well as the top of the chamber. There are four 2.75” and two 4.5” CF flanges placed at a 45° angle from the horizontal. There are two QF25 ports on the nipple and the bottom flange is a QF250 type. The advantage of using such a multipurpose chamber with a variety of ports is to be able to implement multiple types of HHG sources such as gas cells, pulsed valves, capillaries, or solid surfaces. The turbomolecular pump to be used with this chamber is a Varian Turbo-V 3K-G, capable of evacuating a volume of ∼2000 litres per second and backed by a Varian Triscroll 600 (500 L/min) roughing pump. The 3K-G pump was chosen to ensure we could work with HHG sources that require high pressure throughput such as a semi-infinite or finite gas cell since HHG efficiency is dependent on pressure in the laser interaction region.

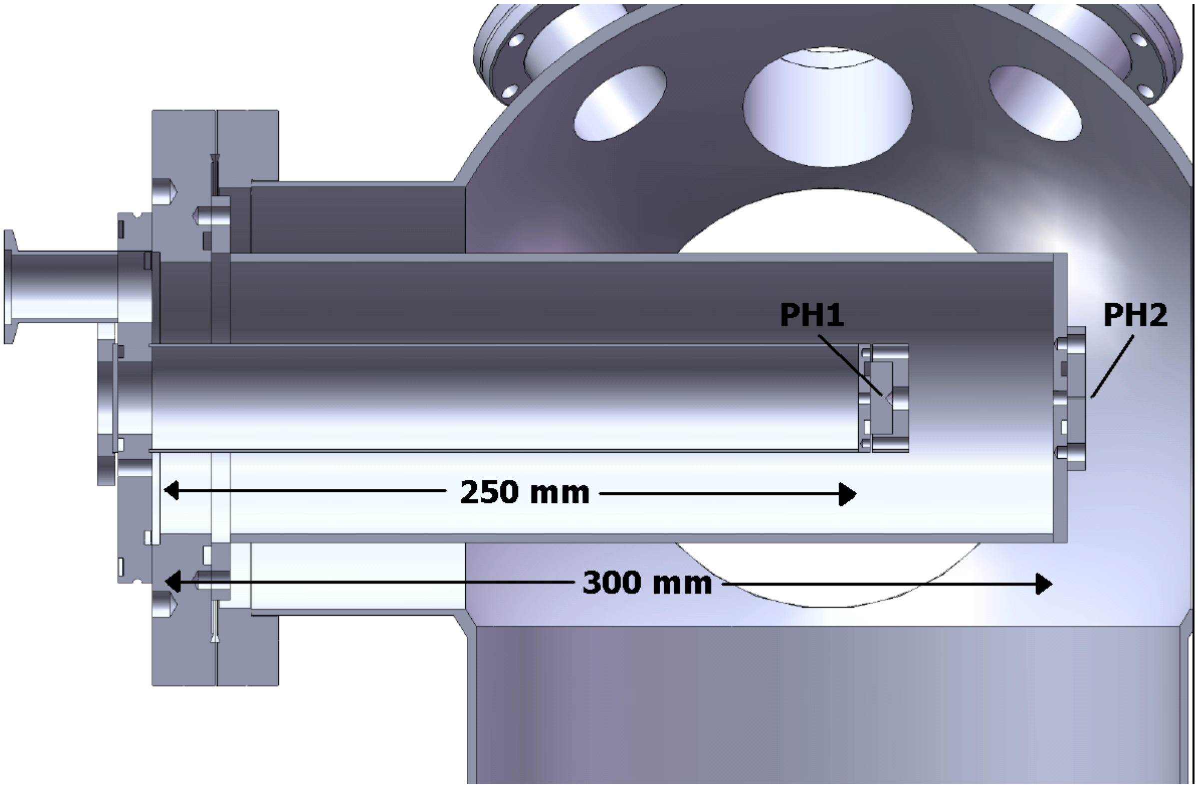

Figure A.2: The schematic of the semi-infinite gas cell. The inner and outer tubes measure 250 and 300 mm, respectively. The inner tube pinhole (PH1) measures 150 μm in diameter while the outer tube pinhole (PH2) has a 1 mm diameter.

A SIGC designed by the author to be used to generate high harmonics (similar to the one used in experiments at ALLS, see Publication 1) was built and installed into the HHG system. A schematic of the SIGC is shown in Fig A.2. The SIGC employs a differential pumping geometry to reduce the rate of gas flow into the source and detection chambers. It consists of a cylindrical inner tube (250 mm long with 40 mm diameter) surrounded by a cylindrical outer tube (300 mm long with a 100 mm diamater). The gas sample is delivered into the inner tube by a 1/4" stainless steel tube. A QF25 elbow is connected to the outer tube so that a roughing pump (500 L/min) can be used for differential pumping. The pinholes of the inner and outer tubes have diameters of 150 μm and 1 mm, respectively. The inner pinholes were made by pulling diamond thread through an aluminum base (Fort Wayne Wire Die, Inc.). Preliminary tests with this SIGC were carried out using the HHG detection system at ALLS and similar harmonic yields to what we produce in the SIGC of Publication 1 using λ = 800 nm light were observed.

A.2 Detection chamber

The detection chamber is a rectangular box made of aluminum with a length, width, and height of of 650, 400, and 200 mm, respectively. The chamber and all of its components were designed by the author. A 3D schematic of the chamber (without the lid) is shown in Fig. A.3. Each face of the chamber contains multiple custom-designed flanges for various feedthroughs and ports to access the chamber interior. The left face of the detection chamber connects to the source chamber via 6" CF flange. A cylindrical tube (130 mm long with 38 mm diameter) along with a differential pumping straw (20 mm long with 3 mm diameter) is attached to the left face and meets the SIGC in the source chamber to ensure differential pumping between the source and detector chambers. A 6" CF flange on the bottom of the detection chamber connects to a turbomolecular pump (Varian Turbo-V 301 Navigator, 300 L/s). The bottom flange also has a series of 1/4"-20 tapped holes with 1" separation to be used as a breadboard to fasten optics within the detection chamber. The right face of the detection chamber contains a 140 × 60 mm rectangular window where a CCD camera can view the microchannel plate detector inside the system. Two 2.75" CF ports on the right side are used to connect

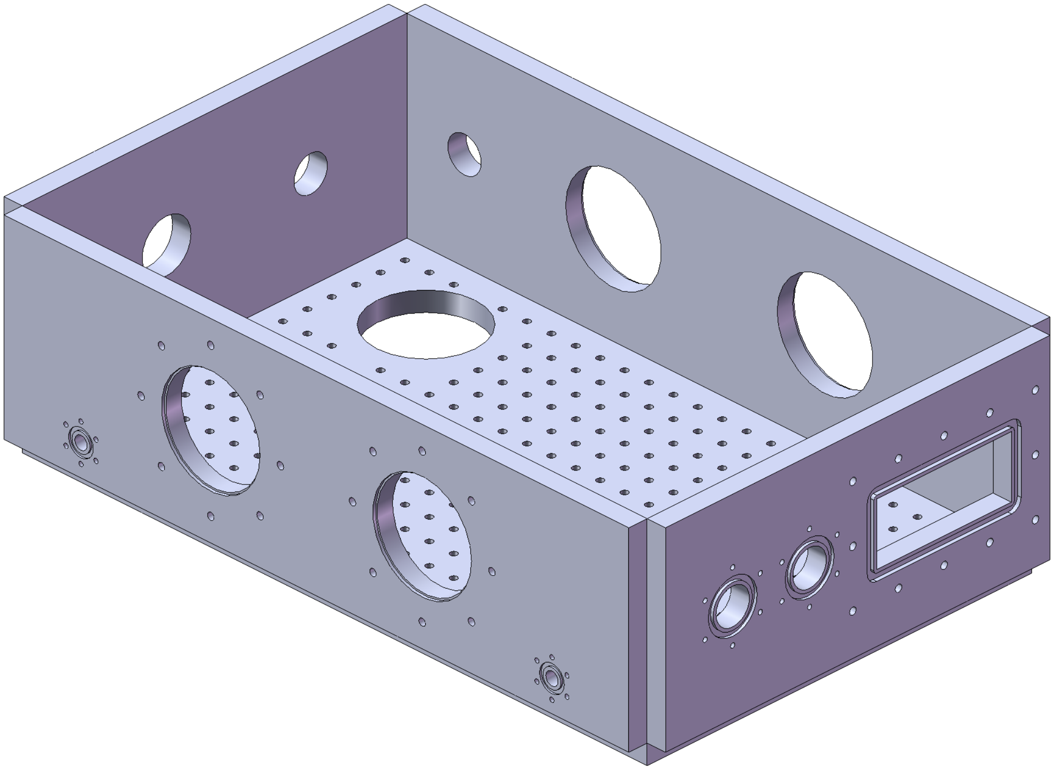

Figure A.3: The 3D schematic of the HHG detection chamber (without lid).

the detection chamber to an interaction chamber. One of these ports is in-line with the SIGC to allow both the HHG emission as well as the fundamental beam to propagate out of the chamber together. The second port is shifted by 80 mm and optics inside the detection chamber will remove the fundamental beam so that the HHG emission can exit this port by itself. The front and back flanges of the detection chamber contain various ports to allow feedthroughs and linear manipulators to access the chamber. The top flange contains two handles to be used when removing the lid of the chamber as well as a port for a 4.5” diameter window for viewing access.

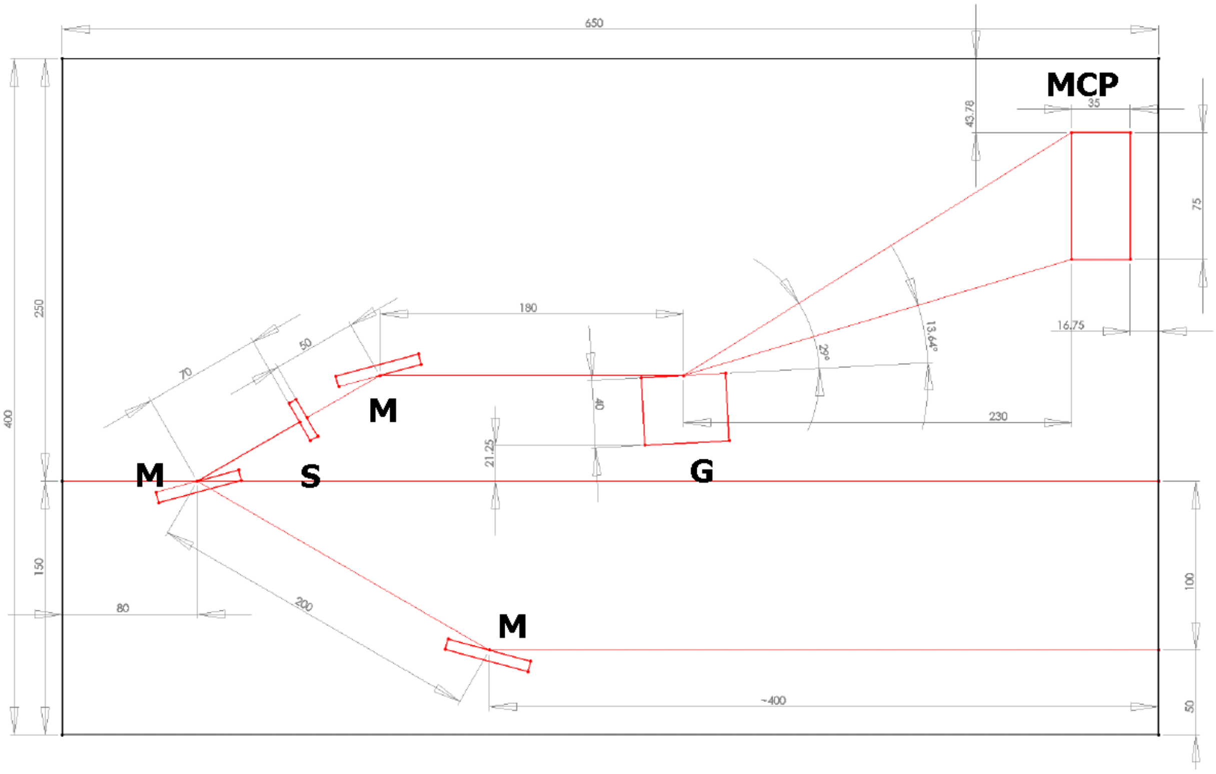

Figure A.4: The schematic of the beam direction as it propagates through the HHG detection chamber. The beam enters from the left side. The components are labeled as follows: **M** are silicon mirrors set at ∼17° to eliminate the fundamental beam, **S** is an adjustable slit to attenuate the spreading of the harmonics in the horizontal direction, **G** is the grating to disperse the harmonics, and **MCP** represents the microchannel plate detector and coupled phosphor screen to image the dispersed XUV spectrum.

A schematic of the inner components of the detection chamber is shown in Fig. A.4. The main component of the chamber is the XUV spectrometer to allow the observation of emitted high harmonics in real time. The beam enters from the left side. It is reflected off of two silicon mirrors set at the Brewster angle for 800 nm (∼17°) to eliminate the fundamental beam then dispersed by a grating (Hitachi) onto a microchannel plate (MCP) detector (Photonis) coupled to a phosphor screen to image the dispersed XUV spectrum. An adjustable slit set between the two silicon mirrors is used to attenuate the horizontal spreading of the XUV beam so that good spatial resolution is achieved when imaging the harmonics. The focal plane of the grating is at a distance of 235.5 mm. The distance of the MCP with respect to the grating can be adjusted using a linear stage. A CCD camera is used externally to record the spectrum shown on the phosphor screen and connected to a computer with software used to convert the CCD picture to a high harmonic spectrum.

The first mirror is mounted on a double mirror mount connected to a linear stage and controlled by a manual linear actuator. The technical drawing of the double mirror mount is shown in Fig. A.5. The three positions of the mirror mount correspond to the HHG beam either being directed to the XUV spectrometer, passing straight through to a port on the exit side of the chamber, or being directed to another silicon mirror then passing through to a second port on the exit side. When the beam passes straight through the double mirror mount, the fundamental beam propagates along with the HHG beam to the interaction chamber. Two reflections off of the silicon mirror effectively remove the fundamental beam from the HHG beam. Depending on the application needed for the XUV beam, the position of the double mirror mount can easily by changed.

A.3 Interaction chamber

The 2.75" CF flange on the right side of the HHG detection chamber is used to connect to an interaction chamber using flexible bellows. We have previously built a time-of-flight mass spectrometer (TOFMS) for multiple experiments that we plan to attach to our HHG system. More details about this TOFMS can be found in Chapter 6 where we describe experiments on XUV interaction with noble gases carried out at ALLS.

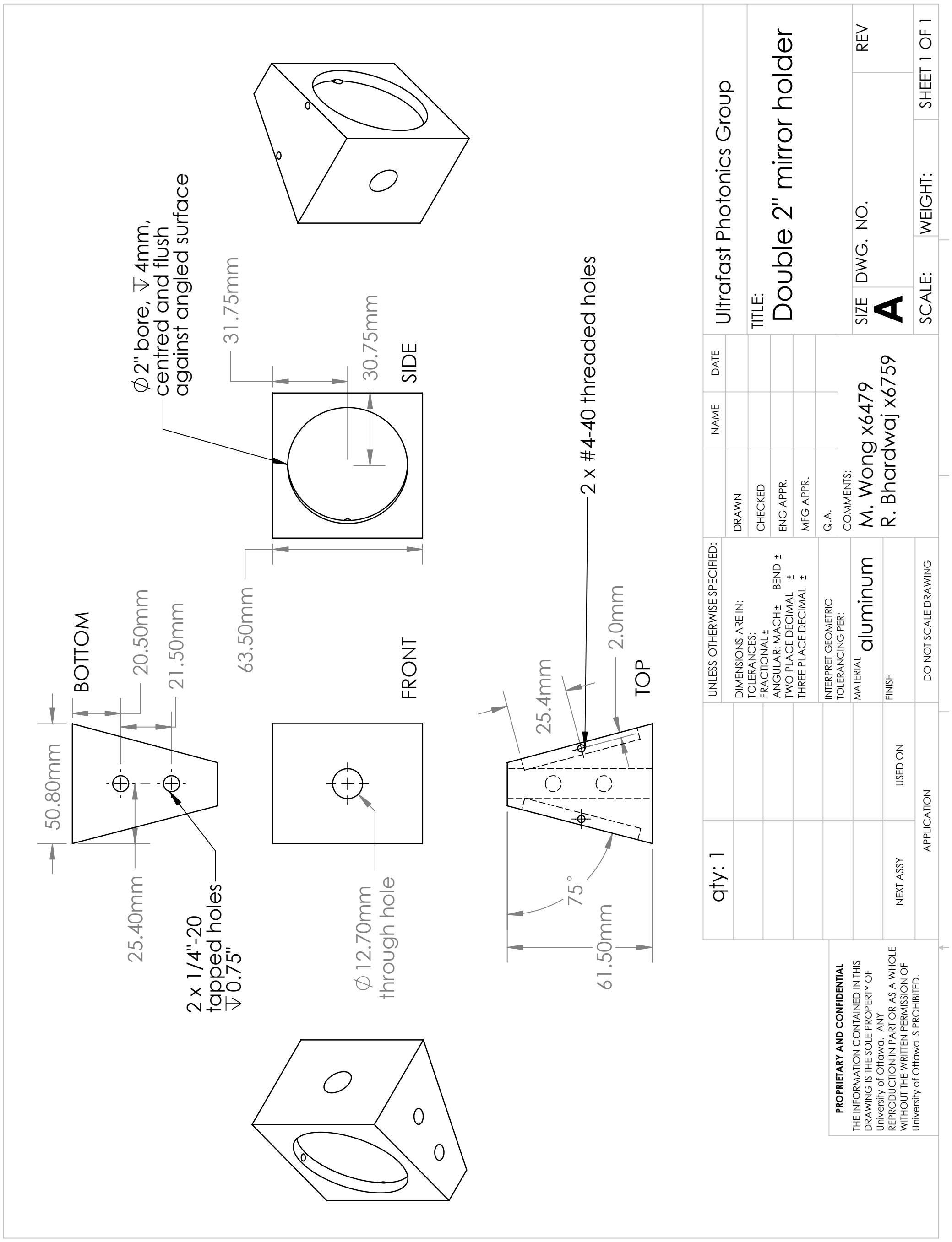

Figure A.5: The technical drawing of the double mirror mount which is used to direct the HHG beam between the XUV spectrometer or access to the interaction chamber.

We have also designed a velocity map imagine (VMI) spectrometer to study electron momentum spectra from XUV interactions with atoms and molecules. VMI makes use of a series of electrodes to create an electrostatic lens which focuses ions (or electrons) with the same velocity onto a single spot on a detector, regardless of where the particle was created in the interaction region. The author helped in the initial design of this spectrometer including simulations of electron focusing and scientific drawings of all spectrometer components. The VMI system has been constructed but awaits preliminary testing.

Fig. A.6 shows a schematic of the full assembly of the source, detection, and interaction (TOFMS) chambers.

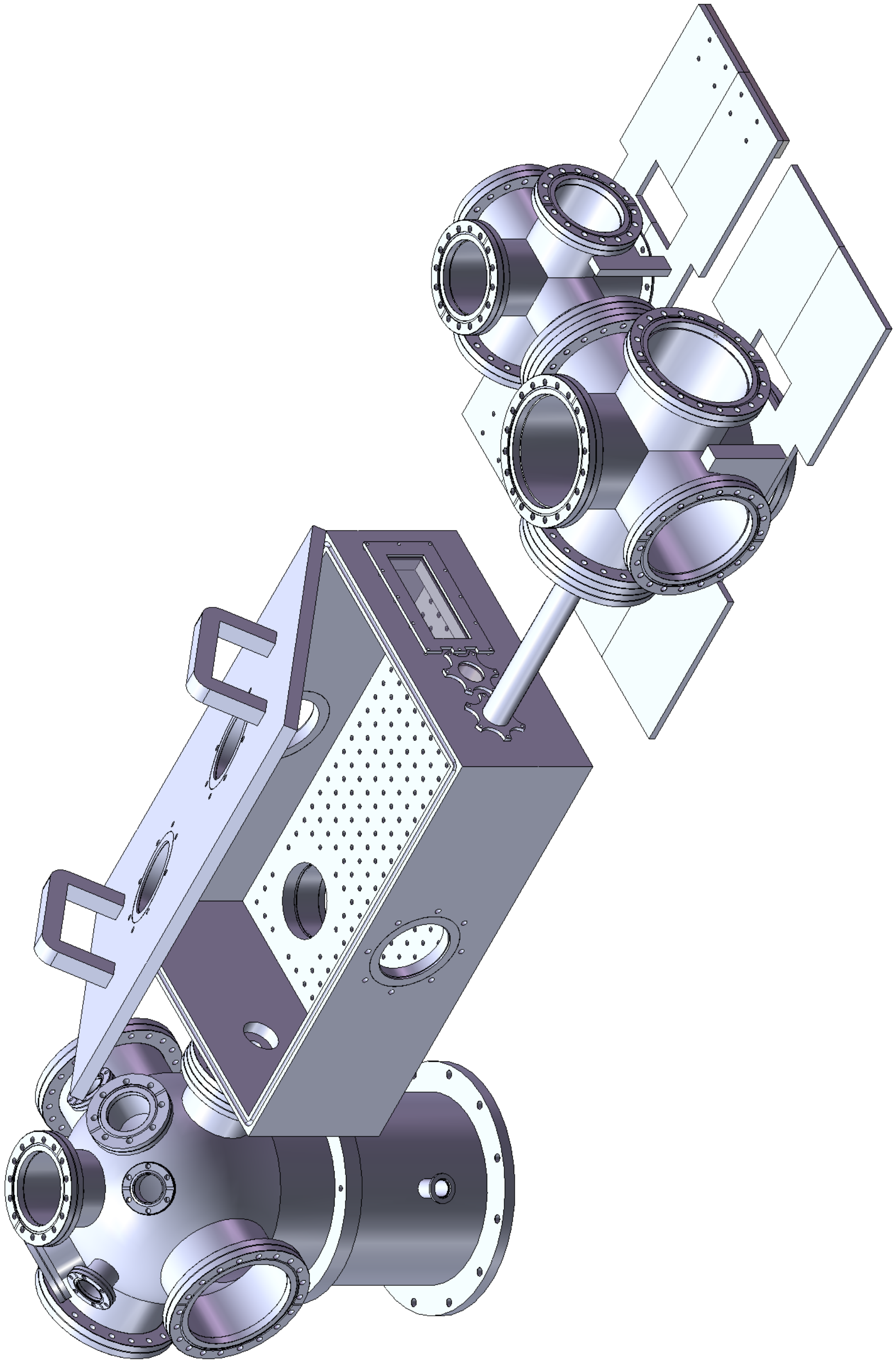

Figure A.6: The schematic of the source, detector, and interaction chamber (TOFMS) all connected together.

Appendix B

Calibrations for HHG experiments

B.1 Energy calibration of MCPs

The energy calibration of the microchannel plate (MCP) detector in the high harmonic generation (HHG) system at the Advanced Laser Light Source was performed using a variety of techniques. A well-known method for calibration is to measure the high harmonic spectrum with an aluminum filter inserted in the beam path and comparing it with the transmission spectrum for the known thickness of aluminum. The transmission curve [112] for a 0.2 μm thick aluminum filter is plotted in Fig. B.1 and demonstrates the strict energy window (17 - 79 eV) that is relevant for MCP calibration. This method allows the easy identification of the first and last harmonic orders.

A second method for calibration is to use high intensity circularly polarized light to ionize gas samples such as O_2 and comparing the plasma emission spectrum on the MCPs with known line values [113]. Finally, we can also use the position of the Cooper minimum in the HHG spectrum of Argon as a reference energy (see Chapter 3).

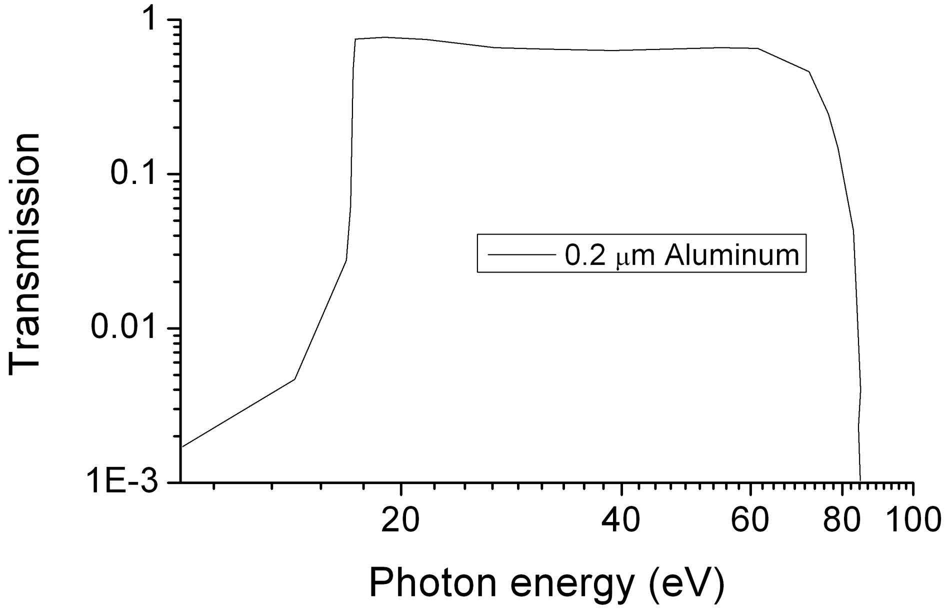

Figure B.1: The transmission through a 0.2 μm thick aluminum filter as a function of photon energy.

B.2 Intensity calibration of fundamental beam

The intensity calibration of the fundamental beam was typically achieved by monitoring the cutoff harmonics from Argon and validated by measuring its saturation intensity using a fast ionization gauge. The ion yield measured by the fast ionization gauge as a function of laser pulse energy is plotted in a semi-log plot as seen in Fig. B.2. We extrapolate the linear portion of the ion signal curve to zero which defines the saturation energy and we then compare with the calculated ion yield using the ADK model to give the saturation intensity [96].

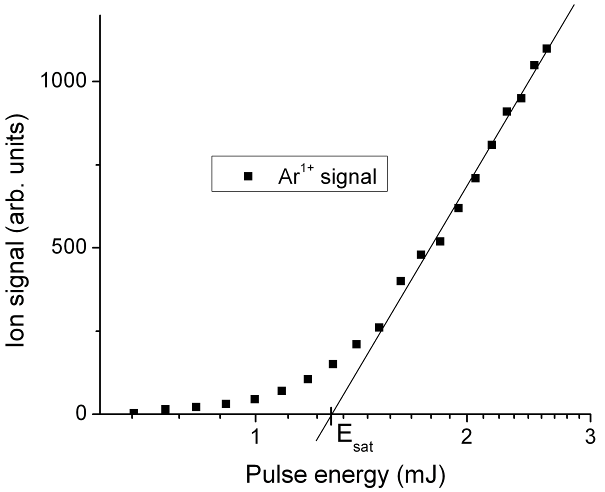

Figure B.2: The extrapolation of the saturation intensity from a semi-log plot of Argon ion signal as a function of fundamental pulse energy.

Bibliography

[1] I. Newton, *Opticks or, a Treatise of the Reflections, Refractions, Inflections, and Colours of Light.* London, England: Printers to the Royal Society, 1704.

[2] A. L. Schawlow and C. H. Townes, "Infrared and optical masers," *Phys. Rev.*, vol. 112, p. 1940, 1958.

[3] R. G. Gould, "The laser, light amplification by stimulated emission of radiation," *The Ann Arbor conference on optical pumping : the University of Michigan*, 1959.

[4] D. J. Gardiner, *Practical Raman spectroscopy.* Berlin, Heidelberg: Springer-Verlag, 1989.

[5] A. Sharma and S. G. Schulman, *Introduction to Fluorescence Spectroscopy.* New York, NY: John Wiley & Sons, 1999.

[6] L. J. Radziemski and D. A. Cremers, *Handbook of laser-induced breakdown spectroscopy.* New York, NY: John Wiley & Sons, 2006.

[7] I. Schechter, A. W. Miziolek, and V. Palleschi, *Laser-induced breakdown spectroscopy (LIBS): fundamentals and applications.* Cambridge, UK: Cambridge University Press, 2006.

[8] A. H. Zewail, *Femtochemistry: Ultrafast Dynamics of the Chemical Bond.* Singapore: World Scientific Publishing Co., 1994.

[9] A. H. Zewail, "Femtochemistry. past, present, and future," *Pure Appl. Chem.*, vol. 72, p. 2219, 2000.

[10] E. Goulielmakis, M. Schultze, M. Hofstetter, V. S. Yakovlev, J. Gagnon, M. Uiberacker, A. L. Aquila, E. M. Gullikson, D. T. Atwood, R. Kienberger, F. Krausz, and U. Kleinberg, "Single-cycle nonlinear optics," *Science*, vol. 320, p. 1614, 2008.

[11] A. McPherson, G. Gibson, H. Jara, U. Johann, T. S. Luk, I. A. McIntyre, K. Boyer, and C. K. Rhodes, "Studies of multiphoton production of vacuum-ultraviolet radiation in the rare gases," *J. Opt. Soc. Am B*, vol. 4, p. 595, 1987.

[12] P. B. Corkum, "Plasma perspective on strong-field multiphoton ionization," *Phys. Rev. Lett.*, vol. 71, p. 1994, 1993.

[13] D. Strickland and G. Mourou, "Compression of amplified chirped optical pulses," *Opt. Commun.*, vol. 56, p. 219, 1985.

[14] G. Steinmeyer, D. H. Sutter, L. Gallmann, N. Matuschek, and U. Keller, "Frontiers in ultrashort pulse generation: Pushing the limits in linear and nonlinear optics," *Science*, vol. 286, p. 1507, 1999.

[15] F. S. Tsung, C. Ren, L. O. Silva, W. B. Mori, and T. Katsouleas, "Generation of ultra-intense single-cycle laser pulses by using photon deceleration," *Proc. Natl. Acad. Sci. U S A*, vol. 99, p. 29, 2002.

[16] A. Baltuska, M. Uiberacker, E. Goulielmakis, R. Kienberger, V. S. Yakovlev, T. Udern, T. W. Hansch, and F. Krausz, "Phase-controlled amplification of few-cycle laser pulses," *Selected Topics in Quantum Electronics, IEEE Journal of*, vol. 9, p. 972, 2003.

[17] R. Kienberger, E. Goulielmakis, M. Uiberacker, A. Baltuska, V. Yakovlev, F. Bammer, A. Scrinzi, T. Westerwalbesloh, U. Kleineberg, U. Heinzmann, M. Drescher, and F. Krausz, "Atomic transient recorder," *Nature*, vol. 427, p. 817, 2004.

[18] R. A. Baumgartner and R. C. Miller, "Optical parametric amplification," *IEEE J. Quantum Electron.*, vol. QE-15, p. 432, 1979.

[19] T. Popmintchev, M.-C. Chen, D. Popmintchev, P. Arpin, S. Brown, S. Alisauskas, G. Andriukaitis, T. Balciunas, O. D. Mucke, A. Pugzlys, A. Baltuska, B. Shim, S. E. Schrauth, A. Gaeta, C. Hernandez-Garcia, L. Plaja, A. Becker, A. Jaron-Becker,

M. M. Murnane, and H. C. Kapteyn, “Bright coherent ultrahigh harmonics in the kev x-ray regime from mid-infrared femtosecond lasers,” *Science*, vol. 336, p. 1287, 2012.

[20] S. W. J. Scully, E. D. Emmons, M. F. Gharaibeh, R. A. Phaneuf, A. L. D. Kilcoyne, A. S. Schlachter, S. Schippers, A. Muller, H. S. Chakraborty, M. E. Madjet, and J. M. Rost, “Photoexcitation of a volume plasmon in c_{60} ions,” *Phys. Rev. Lett.*, vol. 94, p. 065503, 2005.

[21] F. Lepine, G. Sansone, and M. J. J. Vrakking, “Molecular applications of attosecond laser pulses,” *Chem. Phys. Lett.*, vol. 578, p. 1, 2013.

[22] A.-T. Le, R. R. Lucchese, S. Tonzani, T. Morishita, and C. D. Lin, “Quantitative rescattering theory for high-order harmonic generation from molecules,” *Phys. Rev. A*, vol. 80, p. 013401, 2009.

[23] O. Smirnova, S. Patchkovskii, Y. Mairesse, N. Dudovich, D. Villeneuve, P. Corkum, and M. Y. Ivanov, “Attosecond circular dichroism spectroscopy of polyatomic molecules,” *Phys. Rev. Lett.*, vol. 102, p. 063601, 2009.

[24] M. Spanner and S. Patchkovskii, “Molecular strong field ionization and high harmonic generation: A selection of computational illustrations,” *Chem. Phys.*, vol. 414, p. 10, 2013.

[25] H. Niikura, F. Legare, R. Hasbani, M. Y. Ivanov, D. M. Villeneuve, and P. B. Corkum, “Probing molecular dynamics with attosecond resolution using correlated wave packet pairs,” *Nature*, vol. 421, p. 826, 2003.

[26] J. Itatani, J. Levesque, D. Zeidler, H. Niikura, H. Pepin, J. C. Kieffer, P. B. Corkum, and D. M. Villeneuve, “Tomographic imaging of molecular orbitals,” *Nature*, vol. 432, p. 867, 2004.

[27] T. Kanai, S. Minemoto, and H. Sakai, “Quantum interference during high-order harmonic generation from aligned molecules,” *Nature*, vol. 435, p. 470, 2005.

[28] S. Baker, J. S. Robinson, C. A. Haworth, H. Teng, R. A. Smith, C. C. Chirila, M. Lein, J. W. G. Tisch, and J. P. Marangos, “Probing proton dynamics in molecules on an attosecond time scale,” *Science*, vol. 312, p. 424, 2006.

[29] B. K. McFarland, J. P. Farrell, P. H. Bucksbaum, and M. Guhr, “High harmonic generation from multiple orbitals in n_2,” *Science*, vol. 322, p. 1232, 2008.

[30] W. Li, X. Zhou, R. Lock, S. Patchkovskii, A. Stolow, H. C. Kapteyn, and M. M. Murnane, “Time-resolved dynamics in n_2o_4 probed using high harmonic generation,” *Science*, vol. 322, p. 1207, 2008.

[31] O. Smirnova, Y. Mairesse, S. Patchkovskii, N. Dudovich, D. Villeneuve, P. Corkum, and M. Y. Ivanov, “High harmonic interferometry of multi-electron dynamics in molecules,” *Nature*, vol. 460, p. 972, 2009.

[32] C. Vozzi, R. Torres, M. Negro, L. Brugnera, T. Siegel, C. Altucci, R. Velotta, F. Frassetto, L. Poletto, P. Villoresi, S. D. Silvestri, S. Stagira, and J. P. Marangos, “High harmonic generation spectroscopy of hydrocarbons,” *Appl. Phys. Lett.*, vol. 97, p. 241103, 2010.

[33] S. Haessler, J. Caillat, W. Boutu, C. Giovanetti-Texeira, T. Ruchon, T. Auguste, Z. Diveki, P. Breger, A. Maquet, B. Carre, R. Taieb, and P. Salieres, “Attosecond imaging of molecular electronic wavepackets,” *Nat. Phys.*, vol. 6, p. 200, 2010.

[34] H. J. Worner, J. B. Bertrand, D. V. Kartashov, P. B. Corkum, and D. M. Villeneuve, “Following a chemical reaction using high-harmonic interferometry,” *Nature*, vol. 466, p. 604, 2010.

[35] S. Augst, D. Strickland, D. D. Meyerhofer, S. L. Chin, and J. H. Eberly, “Tunneling ionization of noble gases in a high-intensity laser field,” *Phys. Rev. Lett.*, vol. 63, p. 2212, 1989.

[36] L. V. Keldysh, “Ionization in the field of a strong electromagnetic wave,” *Sov. Phys. JETP*, vol. 20, p. 1307, 1965.

[37] C. Winterfeldt, *Generation and control of high-harmonic radiation.* Universitat Wurzburg: Ph.D thesis, 2006.

[38] M. Lewenstein, P. Balcou, M. Y. Ivanov, A. L'huillier, and P. B. Corkum, "Theory of high-harmonic generation by low-frequency laser fields," *Phys. Rev. A*, vol. 49, p. 2117, 1994.

[39] M. V. Ammosov, N. B. Delone, and V. P. Krainov, "Tunnel ionization of complex atoms and of atomic ions in an alternating electromagnetic field," *Sov. Phys. JETP*, vol. 64, p. 1191, 1986.

[40] G. L. Yudin and M. Y. Ivanov, "Nonadiabatic tunnel ionization: Looking inside a laser cycle," *Phys. Rev. A*, vol. 64, p. 013409, 2001.

[41] X. M. Tong, Z. X. Zhao, and C. D. Lin, "Theory of molecular tunneling ionization," *Phys. Rev. A*, vol. 66, p. 033402, 2002.

[42] G. L. Kamta and A. D. Bandrauk, "High-order harmonic generation from two-center molecules: Time-profile analysis of nuclear contributions," *Phys. Rev. A*, vol. 70, p. 011404(R), 2004.

[43] M. W. Schmidt, K. K. Baldridge, J. A. Boatz, S. T. Elbert, M. S. Gordon, J. H. Jensen, S. Koseki, N. Matsunaga, K. A. Nguyen, S. Su, T. L. Windus, M. Dupuis, and J. A. Montgomery, "General atomic and molecular electronic structure system," *J. Comput. Chem.*, vol. 14, p. 1347, 1993.

[44] M. S. Gordon and M. W. Schmidt, *Advances in electronic structure theory: GAMESS a decade later.* Amsterdam, Netherlands: Elsevier, 2005.

[45] V. R. Bhardwaj, D. M. Rayner, D. M. Villeneuve, and P. B. Corkum, "Quantum interference in double ionization and fragmentation of c_6h_6 in intense laser fields," *Phys. Rev. Lett.*, vol. 87, p. 253003, 2001.

[46] B. Shan, X.-M. Tong, Z. Zhao, Z. Chang, and C. D. Lin, "High-order harmonic cutoff extension of the o_2 molecule due to ionization suppression," *Phys. Rev. A*, vol. 66, p. 061401(R), 2002.

[47] O. Smirnova, M. Spanner, and M. Ivanov, "Analytical solutions for strong field-driven atomic and molecular one- and two-electron continua and applications to strong-field problems," *Phys. Rev. A*, vol. 77, p. 033407, 2008.

[48] M. Lein, “Attosecond probing of vibrational dynamics with high-harmonic generation,” *Phys. Rev. Lett.*, vol. 94, p. 053004, 2005.

[49] A. D. Bandrauk, S. Chelkowski, S. Kawai, and H. Lu, “Effect of nuclear motion on molecular high-order harmonics and on generation of attosecond pulses in intense laser pulses,” *Phys. Rev. Lett.*, vol. 101, p. 153901, 2008.

[50] M. Lein, N. Hay, R. Velotta, J. P. Marangos, and P. L. Knight, “Role of the intramolecular phase in high-harmonic generation,” *Phys. Rev. Lett.*, vol. 88, p. 183903, 2002.

[51] A. L’Huillier and P. Balcou, “High-order harmonic generation in rare gases with a 1-ps 1053-nm laser,” *Phys. Rev. Lett.*, vol. 70, p. 774, 1993.

[52] H. J. Worner, H. Niikura, J. B. Bertrand, P. B. Corkum, and D. M. Villeneuve, “Observation of electronic structure minima in high-harmonic generation,” *Phys. Rev. Lett.*, vol. 102, p. 103901, 2009.

[53] J. Higuet, H. Ruf, N. Thiré, R. Cireasa, E. Constant, E. Cormier, D. Descamps, E. Mével, S. Petit, B. Pons, Y. Mairesse, and B. Fabre, “High-order harmonic spectroscopy of the cooper minimum in argon: Experimental and theoretical study,” *Phys. Rev. A*, vol. 83, p. 053401, 2011.

[54] J. W. Cooper, “Photoionization from outer atomic subshells. a model study,” *Phys. Rev.*, vol. 128, p. 681, 1962.

[55] T. A. Carlson, M. O. Krause, F. A. Grimm, P. Keller, and J. W. Taylor, “Angle-resolved photoelectron spectroscopy of ccl$_4$: The cooper minimum in molecules,” *J. Chem. Phys.*, vol. 77, p. 5340, 1982.

[56] C. Altucci, R. Velotta, J. P. Marangos, E. Heesel, E. Springate, M. Pascolini, L. Poletto, P. Villoresi, C. Vozzi, G. Sansone, M. Anscombe, J.-P. Caumes, S. Stagira, and M. Nisoli, “Dependence upon the molecular and atomic ground state of higher-order harmonic generation in the few-optical-cycle regime,” *Phys. Rev. A*, vol. 71, p. 013409, 2005.

[57] E. Takahashi, Y. Nabekawa, T. Otsuka, M. Obara, and K. Midorikawa, "Generation of highly coherent submicrojoule soft x rays by high-order harmonics," *Phys. Rev. A*, vol. 66, p. 021802(R), 2002.

[58] J.-F. Hergott, M. Kovacev, H. Merdji, C. Hubert, Y. Mairesse, E. Jean, P. Breger, P. Agostini, B. Carre, and P. Salieres, "Extreme-ultraviolet high-order harmonic pulses in the microjoule range," *Phys. Rev. A*, vol. 66, p. 021801(R), 2002.

[59] A. Rundquist, C. G. D. III, Z. Chang, C. Herne, S. Backus, M. M. Murnane, and H. C. Kapteyn, "Phase-matched generation of coherent soft x-rays," *Science*, vol. 280, p. 1412, 1998.

[60] C. G. Durfee III, A. Rundquist, S. Backus, C. Herne, Z. Chang, H. C. Kapteyn, and M. M. Murnane, "Phase-matching of high-harmonics in capillary waveguides," *Phys. Rev. Lett*, vol. 83, p. 2187, 1999.

[61] L. G. Gouy, "Sur une propriete nouvelle des ondes lumineuses," *C. R. Acad. Sci. Paris*, vol. 110, p. 1251, 1890.

[62] R. W. Boyd, "Intuitive explanation of the phase anomaly of focused light beams," *J. Opt. Soc. Am.*, vol. 70, p. 877, 1980.

[63] P. Salieres, A. L'Huillier, and M. Lewenstein, "Coherence control of high-order harmonics," *Phys. Rev. Lett.*, vol. 74, p. 3776, 1995.

[64] J. A. Armstrong, N. Bloembergen, J. Ducuing, and P. S. Pershan, "Interactions between light waves in a nonlinear dielectric," *Phys. Rev.*, vol. 127, p. 1918, 1962.

[65] A. Paul, R. A. Bartels, R. Tobey, H. Green, S. Weiman, I. P. Christov, M. M. Murnane, H. C. Kapteyn, and S. Backus, "Quasi-phase-matched generation of coherent extreme-ultraviolet light," *Nature*, vol. 421, p. 51, 2003.

[66] E. A. Gibson, A. Paul, N. Wagner, R. Tobey, D. Gaudiosi, S. Backus, I. P. Christov, A. Aquila, E. M. Gullikson, D. T. Attwood, M. M. Murnane, and H. C. Kapteyn, "Coherent soft x-ray generation in the water window with quasi-phase matching," *Science*, vol. 302, p. 95, 2003.

[67] B. Dromey, M. Zepf, M. Landreman, and S. M. Hooker, "Quasi-phasematching of harmonic generation via multimode beating in waveguides," *Opt. Express*, vol. 15, p. 7894, 2007.

[68] J. Seres, V. S. Yakovlev, E. Seres, C. Streli, P. Wobrauschek, C. Spielmann, and F. Krausz, "Coherent superposition of laser-driven soft-x-ray harmonics from successive sources," *Nat. Phys.*, vol. 3, p. 878, 2007.

[69] S. L. Voronov, I. Kohl, J. B. Madsen, J. Simmons, N. Terry, J. Titensor, Q. Wang, and J. Peatross, "Control of laser high-harmonic generation with counterpropagating light," *Phys. Rev. Lett.*, vol. 87, p. 133902, 2001.

[70] A. L. Lytle, X. Zhang, P. Arpin, O. Cohen, M. M. Murnane, and H. C. Kapteyn, "Quasi-phase matching of high-order harmonic generation at high photon energies using counterpropagating pulses," *Opt. Lett.*, vol. 33, p. 174, 2008.

[71] E. Constant, D. Garzella, P. Breger, E. Mevel, C. Dorrer, C. L. Blanc, F. Salin, and P. Agostini, "Optimizing high harmonic generation in absorbing gases: Model and experiment," *Phys. Rev. Lett.*, vol. 82, p. 1668, 1999.

[72] R. Torres, T. Siegel, L. Brugnera, I. Procino, J. G. Underwood, C. Altucci, R. Velotta, E. Springate, C. Froud, I. C. E. Turcu, M. Y. Ivanov, O. Smirnova, and J. P. Marangos, "Extension of high harmonic spectroscopy in molecules by a 1300 nm laser field," *Opt. Express*, vol. 18, p. 3174, 2010.

[73] E. J. Takahashi, T. Kanai, K. L. Ishikawa, Y. Nabekawa, and K. Midorikawa, "Coherent water window x ray by phase-matched high-order harmonic generation in neutral media," *Phys. Rev. Lett.*, vol. 101, p. 253901, 2008.

[74] T. Popmintchev, M.-C. Chen, A. Bahabad, M. Gerrity, P. Sidorenko, O. Cohen, I. P. Christov, M. M. Murnane, and H. C. Kapteyn, "Phase matching of high harmonic generation in the soft and hard x-ray regions of the spectrum," *Proc. Natl. Acad. Sci. U S A*, vol. 106, p. 10516, 2009.

[75] V. S. Yakovlev, M. Ivanov, and F. Krausz, "Enhanced phase-matching for generation of soft x-ray harmonics and attosecond pulses in atomic gases," *Opt. Express*, vol. 15, p. 15351, 2007.

[76] J. Tate, T. Auguste, H. G. Muller, P. Salieres, P. Agostini, and L. F. DiMauro, "Scaling of wave-packet dynamics in an intense midinfrared field," *Phys. Rev. Lett.*, vol. 98, p. 013901, 2007.

[77] M. V. Frolov, N. L. Manakov, and A. F. Starace, "Wavelength scaling of high-harmonic yield: Threshold phenomena and bound state symmetry dependence," *Phys. Rev. Lett.*, vol. 100, p. 173001, 2008.

[78] A. D. Shiner, C. Trallero-Herrero, N. Kajumba, H.-C. Bandulet, D. Comtois, F. Legare, M. Giguere, J.-C. Kieffer, P. B. Corkum, and D. M. Villeneuve, "Wavelength scaling of high harmonic generation efficiency," *Phys. Rev. Lett.*, vol. 103, p. 073902, 2009.

[79] H. J. Worner, J. B. Bertrand, P. B. Corkum, and D. M. Villeneuve, "High-harmonic homodyne detection of the ultrafast dissociation of br_2 molecules," *Phys. Rev. Lett.*, vol. 105, p. 103002, 2010.

[80] H. Ruf, C. Handschin, A. Ferre, N. Thire, J. B. Bertrand, L. Bonnet, R. Cireasa, E. Constant, P. B. Corkum, D. Descamps, B. Fabre, P. Larregaray, E. Mevel, S. Petit, B. Pons, D. Staedter, H. J. Worner, D. M. Villeneuve, Y. Mairesse, P. Halvick, and V. Blanchet, "High-harmonic transient grating spectroscopy of no2 electronic relaxation," *J. Chem. Phys.*, vol. 137, p. 224303, 2012.

[81] H. A. Barton, "Single and double ionization of argon by electron impacts," *Phys. Rev.*, vol. 25, p. 469, 1925.

[82] M. F. Lin, D. M. Neumark, O. Gessner, and S. R. Leone, "Ionization and dissociation dynamics of vinyl bromide probed by femtosecond extreme ultraviolet transient absorption spectroscopy," *J. Chem. Phys.*, vol. 140, p. 064311, 2014.

[83] G. Herink, D. R. Solli, M. Guide, and C. Ropers, "Field-driven photoemission from nanostructures quenches the quiver motion," *Nature*, vol. 483, p. 190, 2012.

[84] M. I. Stockman, "Nanoplasmonics: past, present, and glimpse into future," *Opt. Express*, vol. 19, p. 22029, 2011.

[85] M. Y. Amusia and A. S. Baltenkov, "On the possibility of considering the fullerene shell c_{60} as a conducting sphere," *Phys. Lett. A*, vol. 360, p. 294, 2006.

[86] I. V. Hertel, T. Laarmann, and C. P. Schulz, "Ultrafast excitation, ionization, and fragmentation of c_{60}," *Adv. At. Mol. Opt. Phys.*, vol. 50, p. 219, 2005.

[87] A. Jaron-Becker, A. Becker, and F. H. M. Faisal, "Single-active-electron ionization of c_{60} in intense laser pulses to high charge states," *J. Chem. Phys.*, vol. 126, p. 124310, 2007.

[88] M. E. Madjet, H. S. Chakraborty, J. M. Rost, and S. T. Manson, "Photoionization of c_{60}: a model study," *J. Phys. B: At. Mol. Opt. Phys.*, vol. 41, p. 105101, 2008.

[89] Y. Huismans, E. Cormier, C. Cauchy, P.-A. Hervieux, G. Gademann, A. Gijsbertsen, O. Ghafur, P. Johnsson, P. Logman, T. Barillot, C. Bordas, F. Lepine, and M. J. Vrakking, "Macro-atom versus many-electron effects in ultrafast ionization of c_{60}," *Phys. Rev. A*, vol. 88, p. 013201, 2013.

[90] R. A. Ganeev, L. B. E. Bom, J. Abdul-Hadi, M. C. H. Wong, J. P. Brichta, V. R. Bhardwaj, and T. Ozaki, "Higher-order harmonic generation from fullerene by means of the plasma harmonic method," *Phys. Rev. Lett.*, vol. 102, p. 013903, 2009.

[91] V. R. Bhardwaj, P. B. Corkum, and D. M. Rayner, "Internal laser-induced dipole force at work in c_{60} molecule," *Phys. Rev. Lett.*, vol. 91, p. 203004, 2003.

[92] V. R. Bhardwaj, P. B. Corkum, and D. M. Rayner, "Recollision during the high laser intensity ionization of c_{60}," *Phys. Rev. Lett.*, vol. 93, p. 043001, 2004.

[93] V. R. Bhardwaj, S. A. Aseyev, M. Mehendale, G. L. Yudin, D. M. Villeneuve, D. M. Rayner, M. Y. Ivanov, and P. B. Corkum, "Few cycle dynamics of multiphoton double ionization," *Phys. Rev. Lett.*, vol. 86, p. 3522, 2001.

[94] D. Kaplan and P. Tournois, "Acousto-optic spectral filtering of femtosecond laser pulses," *Ultrafast Optics IV in Springer Series in OPTICAL SCIENCES*, vol. 95, p. 105, 2004.

[95] M. Nisoli, S. D. Silvestri, O. Svelto, R. Szipocs, K. Ferencz, C. Spielmann, S. Sartania, and F. Krausz, “Compression of high-energy laser pulses below 5 fs,” *Opt. Lett.*, vol. 22, p. 522, 1997.

[96] S. M. Hankin, D. M. Villeneuve, P. B. Corkum, and D. M. Rayner, “Nonlinear ionization of organic molecules in high intensity laser fields,” *Phys. Rev. Lett.*, vol. 84, p. 5082, 2000.

[97] F. Légaré, I. V. Litvinyuk, P. W. Dooley, F. Queré, A. D. Bandrauk, D. M. Villeneuve, and P. B. Corkum, “Time-resolved double ionization with few cycle laser pulses,” *Phys. Rev. Lett.*, vol. 91, p. 093002, 2003.

[98] I. A. and Y. Yamamoto, “Turnstile device for heralded single photons: Coulomb blockade of electron and hole tunneling in quantum confined p-i-n heterojunctions,” *Phys. Rev. Lett.*, vol. 72, p. 210, 1994.

[99] F. Mauger, C. Chandre, and T. Uzer, “Recollisions and correlated double ionization with circularly polarized light,” *Phys. Rev. Lett.*, vol. 105, p. 083002, 2010.

[100] T. Brabec, M. Y. Ivanov, and P. B. Corkum, “Coulomb focusing in intense field atomic processes,” *Phys. Rev. A*, vol. 54, p. R2551(R), 1996.

[101] S. Kimura, “Method for measuring the spot size of a laser beam using a boundary-diffraction wave,” *Opt. Lett.*, vol. 12, p. 552, 1987.

[102] A. D. Shiner, B. E. Schmidt, C. Trallero-Herrero, H. J. Worner, S. Patchkovskii, P. B. Corkum, J.-C. Kieffer, F. Legare, and D. M. Villeneuve, “Probing collective multi-electron dynamics in xenon with high-harmonic spectroscopy,” *Nat. Phys.*, vol. 7, p. 464, 2011.

[103] S. Minemoto, T. Umegaki, Y. Oguchi, T. Morishita, A.-T. Le, S. Watanabe, and H. Sakai, “Retrieving photorecombination cross sections of atoms from high-order harmonic spectra,” *Phys. Rev. A*, vol. 78, p. 061402(R), 2008.

[104] M. Lein, P. P. Corso, J. P. Marangos, and P. L. Knight, “Orientation dependence of high-order harmonic generation in molecules,” *Phys. Rev. A*, vol. 67, p. 029819, 2003.

[105] S. Petretti, A. Saenz, A. Castro, and P. Decleva, "Orientation dependence of high-order harmonic generation in molecules," *Chem. Phys.*, vol. 414, p. 45, 2013.

[106] E. T. J. Nibbering, H. Fidder, and E. Pines, "Ultrafast chemistry: Using time-resolved vibrational spectroscopy for interrogation of structural dynamics," *Annu. Rev. Phys. Chem.*, vol. 56, p. 337, 2005.

[107] S. R. Mishra, *Biomolecules.* New Delhi, India: Discovery Publishing House, 2003.

[108] F. Remacle and R. D. Levine, "An electronic time scale in chemistry," *Proc. Natl. Acad. Sci. U S A*, vol. 103, p. 6793, 2006.

[109] R. A. Ganeev, "Generation of higher harmonics of laser radiation in plasma formed by pulses with a 1khz repetition rate," *Opt. and Spect.*, vol. 114, p. 614, 2013.

[110] G. P. Zhang, "Optical high harmonic generation in c_{60}," *Phys. Rev. Lett.*, vol. 95, p. 047401, 2005.

[111] M. F. Ciappina, A. Becker, and A. Jaron-Becker, "Multislit interference patterns in high-order harmonic generation in c_{60}," *Phys. Rev. A*, vol. 76, p. 063406, 2007.

[112] B. L. Henke, E. M. Gullikson, and J. C. Davis, "X-ray interactions: photoabsorption, scattering, transmission, and reflection at e=50-30000 ev, z=1-92," *Atomic Data and Nuclear Data Tables*, vol. 54, p. 181, 1993.

[113] J. J. Camacho, M. Santos, L. Diaz, and J. M. L. Poyato, "Optical emission spectroscopy of oxygen plasma induced by ir co_2 pulsed laser," *J. Phys. D: Appl. Phys.*, vol. 41, p. 215206, 2008.